



63667044

This is to certify that the  
dissertation entitled

**ROLES OF SERVICE PARAMETERS  
ON THE MECHANICAL BEHAVIOR OF  
LEAD-FREE SOLDER JOINTS**

presented by

Hongjoo Rhee

has been accepted towards fulfillment  
of the requirements for the

Ph.D.

degree in

Department of  
Chemical Engineering and  
Materials Science

*S. N. Subramanian*

Major Professor's Signature

*February, 26, 2005*

Date

*MSU is an Affirmative Action/Equal Opportunity Institution*



**ROLES OF SERVICE PARAMETERS ON THE MECHANICAL BEHAVIOR OF  
LEAD-FREE SOLDER JOINTS**

By

Hongjoo Rhee

**A DISSERTATION**

Submitted to  
Michigan State University  
in partial fulfillment of the requirements  
for the degree of

**DOCTOR OF PHILOSOPHY**

Department of Chemical Engineering and Materials Science

2005

## **ABSTRACT**

### **ROLES OF SERVICE PARAMETERS ON THE MECHANICAL BEHAVIOR OF LEAD-FREE SOLDER JOINTS**

By

Hongjoo Rhee

Lead-based solders have been extensively used as interconnects in various electronic applications due to their low cost and suitable material properties. However, in view of environmental and health concerns, the electronics industry is forced to develop lead-free alternative solders. Eutectic Sn-3.5Ag based solders are being considered as suitable substitutes due to their non-toxicity, tolerable melting temperatures, and comparable mechanical as well as electrical properties. Smaller electronic packaging and emerging new technologies impose several constraints on the solder interconnect that require better inherent properties in the solder to resist failure during operation. Hence, it is important to develop a clear understanding of the deformation behavior of eutectic Sn-Ag solder joints.

Mechanical characterization was performed to investigate the behavior of eutectic Sn-Ag solder joints. Peak shear stress and flow stress decreased with increasing testing temperature and with decreasing simple shear-strain rate. The effect of simple shear-strain rate on the peak shear stress was found to be more significant at temperature regimes less than 125°C. The deformation structure of specimens deformed at higher temperatures was dominated by grain boundary deformation, while at lower temperatures it was dominated by shear

banding.

Stress relaxation studies on eutectic Sn-Ag solder joints were carried out to provide a better understanding of various parameters contributing to thermomechanical damage accumulation. Monotonic stress relaxation tests at various pre-strain conditions and testing temperatures can provide information relevant to the effects of ramp rates during heating and cooling excursions experienced during thermomechanical fatigue. Peak shear stress and residual shear stress, resulting from stress relaxation period, decreased with increasing testing temperature for a given pre-strain condition. A faster ramp rate was found to cause higher resultant residual stress as compared to slower ramp rates.

In order to understand the roles of service related parameters, such as pre-strain and pre-strain rate imposed prior to the repeated strain cycling, cyclic strain amplitude and cyclic strain rate, and testing temperature, cyclic shear straining with associated stress relaxation was carried out on pre-strained eutectic Sn-Ag solder joints. These parameters may play significant roles during actual thermomechanical fatigue cycles of the solder joints in electronic devices. Cyclic straining may be able to provide more stress relaxation in specimens deformed to higher pre-strain/cyclic-strain at a higher pre-strain rate/cyclic-strain rate under low testing temperature. In specimens deformed at higher temperatures, residual stress build-up is less significant and as a consequence cyclic straining has no significant influence on the stress relaxation behavior. At high temperature, processes such as crack healing (or recovery) can take place, whereas microstructural damage may accumulate easier at lower temperatures.

to my parents, Hang-Chull Rhee and In-Kyung Chung, and family

## ACKNOWLEDGMENTS

I would like to express my sincere gratitude to my advisor, Professor K.N. Subramanian for all his excellent guidance, encouragement, and assistance throughout my doctoral studies at Michigan State University. Without his effort, patience, and support this work would not have been possible. I would also like to show my deep appreciation to Professor James P. Lucas and Professor Thomas R. Bieler for their kind help and instruction throughout the entire work. Thanks are also due to Professor Phillip M. Duxbury and Professor Dahsin Liu for serving on my graduate committee and giving me valuable suggestions and comments. Special thanks go to Professor Andre Lee for not only letting me use his apparatus but also giving me generous advice. Appreciation is also extended to my fellow graduate students and friends for providing both technical and social support over the long duration of my stay in East Lansing.

I would like to acknowledge the financial support provided by the National Science Foundation under grant number NSF-DMR-0081796, and the Air Force Research Laboratory in providing partial funding for the acquisition of the RSA-III.

My sincere gratitude and respect go to Professor Kihyon Kim at North Carolina Central University and Professor Patrick Y. Kwon for their devoted advice, moral support, and encouragement.

Finally, my deepest thanks from the bottom of my heart are extended to my parents, my sister and her family, and my brother and his family whose love, sacrifice, guidance, and encouragement have supported me throughout my life.

# TABLE OF CONTENTS

<b>LIST OF TABLES</b> .....	x
<b>LIST OF FIGURES</b> .....	xii
<b>CHAPTER 1</b>	
<b>INTRODUCTION</b> .....	1
<b>CHAPTER 2</b>	
<b>OVERVIEW</b> .....	6
2.1 MICROSTRUCTURAL COMPARISON BETWEEN BULK SOLDER AND SOLDER JOINT .....	6
2.2 THERMOMECHANICAL FATIGUE (TMF) .....	8
2.3 PARAMETERS CONTRIBUTING TO TMF BEHAVIOR .....	14
2.3.1 Overview (TMF Cycling) .....	14
2.3.2 Parameters Contributing to TMF Cycle .....	16
2.4 MECHANICAL PROPERTIES FOR AN UNDERSTANDING OF THE ROLES OF TMF PARAMETERS .....	19
2.4.1 Mechanical Properties Test .....	19
2.4.2 Stress Relaxation Test (Residual Mechanical Properties) .....	20
2.4.3 Nanoindentation Test .....	26
2.4.4 Alloyin/Composite Solders .....	27
2.4.4.1 Alloying Solders .....	27
2.4.4.2. Composite Solders .....	28
<b>CHAPTER 3</b>	
<b>MECHANICAL CHARACTERIZATION OF EUTECTIC Sn-3.5Ag</b>	

SOLDER JOINTS AT VARIOUS TEMPERATURES .....	31
3.1 INTRODUCTION .....	32
3.2 EXPERIMENTAL PROCEDURES .....	34
3.3 RESULTS AND DISCUSSION .....	40
3.4 SUMMARY .....	48
<b>CHAPTER 4</b>	
<b>EFFECTS OF PRE-STRAIN, RATE OF PRE-STRAIN, AND TEMPERATURE ON THE STRESS RELAXATION BEHAVIOR OF EUTECTIC Sn-3.5Ag SOLDER JOINTS .....</b>	<b>49</b>
4.1 INTRODUCTION .....	50
4.2 EXPERIMENTAL PROCEDURES .....	51
4.3 RESULTS AND DISCUSSION .....	53
4.4 SUMMARY AND CONCLUSIONS .....	66
<b>CHAPTER 5</b>	
<b>ROLES OF IMPOSED PRE-STRAIN, PRE-STRAIN RATE, AND TEMPERATURE ON THE CYCLIC STRESS RELAXATION BEHAVIOR OF PRE-STRAINED EUTECTIC Sn-3.5Ag SOLDER JOINTS .....</b>	<b>68</b>
5.1 INTRODUCTION .....	69
5.2 EXPERIMENTAL PROCEDURES .....	70
5.3 RESULTS AND DISCUSSION .....	74
5.3.1 Effects of Pre-Strain .....	74
5.3.2 Effects of Pre-Strain Rate .....	76
5.3.3 Effects of Testing Temperature .....	78
5.3.4 Microstructural Characterization .....	80
5.3.5 Comparisons of the Solder Joint Behavior between SR and SRC Conditions .....	83

5.3.5.1 Solder Joint Behavior .....	83
5.3.5.2 Creep Properties .....	87
5.3.5.3 General Trend .....	89
5.4 SUMMARY AND CONCLUSIONS .....	92
<b>CHAPTER 6</b>	
<b>ROLES OF IMPOSED CYCLIC STRAIN AMPLITUDE</b>	
<b>AND CYCLIC STRAIN RATE ON THE</b>	
<b>CYCLIC STRESS RELAXATION BEHAVIOR OF</b>	
<b>PRE-STRAINED EUTECTIC Sn-3.5Ag SOLDER JOINTS .....</b>	<b>93</b>
6.1 INTRODUCTION .....	94
6.2 EXPERIMENTAL PROCEDURES .....	96
6.3 RESULTS AND DISCUSSION .....	99
6.3.1 Effects of Cyclic Strain Amplitude .....	99
6.3.2 Effects of Cyclic Strain Rate .....	101
6.3.3 Microstructural Characterization .....	105
6.3.4 Comparisons of the Solder Joint Behavior between SR and SRC Conditions .....	110
6.4 SUMMARY AND CONCLUSIONS .....	118
<b>CHAPTER 7</b>	
<b>DISCUSSION .....</b>	<b>119</b>
<b>CHAPTER 8</b>	
<b>SUMMARY .....</b>	<b>124</b>
<b>APPENDIX A</b>	
<b>MICROMECHANICAL CHARACTERIZATION OF</b>	
<b>THERMOMECHANICALLY FATIGUED</b>	
<b>LEAD-FREE SOLDER JOINTS .....</b>	<b>129</b>

**APPENDIX B**  
**EFFECTS OF INTERMETALLIC MORPHOLOGY AT**  
**METALLIC PARTICLE/SOLDER INTERFACE ON**  
**MECHANICAL PROPERTIES OF Sn-Ag BASED SOLDER JOINTS ..... 156**

**REFERENCES ..... 181**

## LIST OF TABLES

### CHAPTER 4

Table 4.1	Peak shear stress values at a simple shear strain of 0.3 imposed prior to the stress relaxation events (MPa) .....	57
Table 4.2	Residual shear stress values in 300 seconds (and in 1,000 seconds) after the stress relaxation events for a fixed simple shear-strain of 0.3 (MPa) .....	57
Table 4.3	Peak shear stress values at a simple shear strain of 0.2 imposed prior to the stress relaxation events (MPa) .....	58
Table 4.4	Residual shear stress values in 300 seconds (and in 1,000 seconds) after the stress relaxation events for a fixed simple shear-strain of 0.2 (MPa) .....	58

### CHAPTER 5

Table 5.1	Testing parameters for SRC experiments. $\gamma_c$ imposed was 0.05, and hold times at maximum and minimum shear-strain extremes for stress relaxation experiments were 300 seconds .....	72
-----------	-------------------------------------------------------------------------------------------------------------------------------------------------------------------------------------------	----

### CHAPTER 6

Table 6.1	Testing parameters for SRC experiments. $\gamma_c$ imposed was 0.1, and hold times at maximum and minimum shear strain extremes for stress relaxation experiments were 300 seconds .....	98
-----------	------------------------------------------------------------------------------------------------------------------------------------------------------------------------------------------	----

### APPENDIX A

Table A.1	Micromechanical properties of constituent phases in eutectic Sn-3.5Ag solder joints .....	139
Table A.2	Micromechanical properties of constituent phases in Sn-4.0Ag-0.5Cu solder joints .....	143
Table A.3	Micromechanical properties of constituent phases	

in Sn-Ag-1.0Cu-1.0Ni solder joints ..... 145

## LIST OF FIGURES

### CHAPTER 2

- Figure 2.1 Typical microstructures of (a) bulk eutectic Sn-Ag solder and (b) eutectic Sn-Ag solder joint with Cu substrates ..... 7
- Figure 2.2 The behavior of the solder alloy and joint throughout a thermal cycle ..... 10
- Figure 2.3 The typical temperature-time profile experienced by solder joints in service condition ..... 17

### CHAPTER 3

- Figure 3.1 A schematic illustration of (a) a single shear-lap joint and (b) joint making fixture used in this study ..... 35
- Figure 3.2 A reflow profile for solder joint fabrication. Heating rate is 5°C/sec, peak (target) temperature is 250°C, and cooling rate is 1°C/sec in this profile ..... 37
- Figure 3.3 A thermal/mechanical analyzer used in this study. (a) Entire view of the apparatus, (b) specimen installation part, and (c) a schematic of the solder joint under shear state ..... 38
- Figure 3.4 Shear stress versus simple shear-strain plots for eutectic Sn-Ag solder joints at various simple shear-strain rates of (a) 0.001 /s, (b) 0.01 /s, and (c) 0.1 /s at different testing temperatures ..... 41
- Figure 3.5 (a) Peak shear stress and (b) simple shear-strain at peak shear stress, as a function of temperature at different simple shear-strain rates ..... 42
- Figure 3.6 Microstructures of the solder joint side surfaces (obtained from middle of the fine polished side of the specimen) after shear tests for specimens deformed at a simple shear-strain rate of 0.1 /s at (a) 25°C, (b) 75°C, (c) 100°C, (d) 125°C, and (e) 150°C ..... 43
- Figure 3.7 Microstructures of the middle of the solder joint

	side surfaces after shear testing for specimens deformed at simple shear-strain rates of (a) 0.001 /s at 25°C, (b) 0.1 /s at 25°C, (c) 0.001 /s at 150°C, and (d) 0.1 /s at 150°C .....	45
Figure 3.8	Relationship between simple shear-strain rate and peak shear stress obtained from shear tests .....	47
Figure 3.9	Relationship between shear stress and testing temperature at different simple shear-strain rates obtained from shear tests .....	47

#### CHAPTER 4

Figure 4.1	A schematic illustration of the effect of simple shear-strain rate during pre-loading on residual shear stress resulting from stress relaxation at a constant temperature after imposing a fixed simple shear-strain. Curve A - fast simple shear-strain rate (corresponds to fast ramp-rate), curve B - medium simple shear-strain rate (corresponds to medium ramp-rate), curve C - slow simple shear-strain rate (corresponds to slow ramp-rate) .....	54
Figure 4.2	Loading and stress relaxation curves of the eutectic Sn-Ag solder joints pre-strained prior to the stress relaxation events at simple shear-strain of 0.3 with various simple shear-strain rates of (a) 0.0001 /s, (b) 0.001 /s, and (c) 0.01 /s at various testing temperatures .....	56
Figure 4.3	Microstructures of the solder joint side surfaces after the stress relaxation tests. The specimens were pre-strained to a simple shear-strain of 0.3 at (a) 25°C, (b) 85°C, and (c) 150°C. (d), (e), and (f) are corresponding enlarged views of (a), (b), and (c). All specimens were pre-strained at a simple shear-strain rate of 0.01 /s prior to the stress relaxation .....	60
Figure 4.4	Microstructures of the solder joint side surfaces after the stress relaxation tests. The specimens were pre-strained to a simple shear-strain of 0.2 at (a) 25°C, (b) 85°C, and (c) 150°C. (d), (e), and (f) are corresponding enlarged views of (a), (b), and (c). All specimens were pre-strained at a simple shear-strain rate of 0.01 /s prior to	

	the stress relaxation .....	61
Figure 4.5	Microstructures of the solder joint side surfaces after the stress relaxation tests. The specimens were pre-strained at simple shear-strain rates of (a) 0.0001 /s at 25°C, (b) 0.01 /s at 25°C, (c) 0.0001 /s at 150°C, and (d) 0.01 /s at 150°C. Imposed pre simple shear-strain of (a) and (b) was 0.3, and that of (c) and (d) was 0.2 .....	63
Figure 4.6	Relationship between simple shear-strain rate and shear stress obtained from the stress relaxation part of the tests. The specimens were pre-strained to a simple shear-strain of 0.3 with various simple shear-strain rates of (a) 0.0001 /s, (b) 0.001 /s, and (c) 0.01 /s prior to the stress relaxation events .....	64
Figure 4.7	Schematic illustration of (a) ramp-up and (b) ramp-down situations during TMF cycle .....	65

## CHAPTER 5

Figure 5.1	A schematic of the SRC cycling. The $\gamma_{max}$ and $\gamma_{min}$ were obtained by dividing $\delta_{max}$ and $\delta_{min}$ by joint thickness. $\gamma_c$ ( $\gamma_{max} \sim \gamma_{min}$ ) employed in this study was 0.05 and the cycling was repeated 10 times .....	73
Figure 5.2	Effects of pre-strain on the solder joint behavior under SRC conditions. (a) SRC curves of the eutectic Sn-Ag solder joints, and (b) relationship between the maximum shear stress obtained during each cycle and number of cycles .....	75
Figure 5.3	Effects of pre-strain rate on the solder joint behavior under SRC conditions. (a) SRC curves of the eutectic Sn-Ag solder joints, and (b) relationship between the maximum shear stress obtained during each cycle and number of cycles .....	77
Figure 5.4	Effects of testing temperature on the solder joint behavior under SRC conditions. (a) SRC curves of the eutectic Sn-Ag solder joints at various testing temperatures, and (b) relationship between the maximum shear stress obtained during each cycle and number of cycles .....	79
Figure 5.5	Microstructures of the solder joint side surfaces after	

the SRC tests. All specimens were pre-strained to a  $\gamma_p$  of 0.2 prior to the first cycle, followed by imposing a fixed  $\gamma_c$  and  $\dot{\gamma}_c$ . The specimens were pre-strained at  $\dot{\gamma}_p$ 's of (a) 0.0001 /s at 25°C, (b) 0.0001 /s at 85°C, (c) 0.0001 /s at 150°C, (d) 0.01 /s at 25°C, (e) 0.01 /s at 85°C, and (f) 0.01 /s at 150°C ..... 81

**Figure 5.6** Microstructures of the solder joint side surfaces after the SRC tests. All specimens were pre-strained to a  $\gamma_p$  of 0.3 prior to the first cycle, followed by imposing a fixed  $\gamma_c$  and  $\dot{\gamma}_c$ . The specimens were pre-strained at  $\dot{\gamma}_p$ 's of (a) 0.0001 /s at 25°C, (b) 0.0001 /s at 85°C, (c) 0.0001 /s at 150°C, (d) 0.01 /s at 25°C, (e) 0.01 /s at 85°C, and (f) 0.01 /s at 150°C ..... 82

**Figure 5.7** Comparison of shear stress versus time plots obtained from stress relaxation part of the test between SR and SRC tests. The specimens were pre-strained to (a)  $\gamma_p$  of 0.2 at  $\dot{\gamma}_p$  of 0.0001 /s, (b)  $\gamma_p$  of 0.2 at  $\dot{\gamma}_p$  of 0.01 /s, (c)  $\gamma_p$  of 0.3 at  $\dot{\gamma}_p$  of 0.0001 /s, and (d)  $\gamma_p$  of 0.3 at  $\dot{\gamma}_p$  of 0.01 /s ..... 84

**Figure 5.8** Comparison between microstructures of the solder joint side surfaces after (a) SR and (b) SRC tests at 25°C ..... 86

**Figure 5.9** Relationship between simple shear-strain rate and peak shear stress in each cycle obtained from the stress relaxation part of the test. The specimens were pre-strained to a  $\gamma_p$  of 0.3 at a  $\dot{\gamma}_p$  of 0.01 /s, followed by imposing a fixed  $\gamma_c$  (0.05) and  $\dot{\gamma}_c$  (0.005 /s) ..... 88

**Figure 5.10** Relationship between peak shear stress in each cycle and testing temperature. The specimens were pre-strained to a  $\gamma_p$  of 0.3 at a  $\dot{\gamma}_p$  of 0.01 /s, followed by imposing a fixed  $\gamma_c$  (0.05) and  $\dot{\gamma}_c$  (0.005 /s) ..... 90

Figure 5.11	Schematic comparison of effects of various test parameters on solder joint behavior between SR and SRC tests. Effect of each test parameter can be achieved when all other parameters were held constant. Lines in the stress relaxation regime represent the stress profile under SR condition, and dashed lines represent that under SRC condition .....	91
-------------	------------------------------------------------------------------------------------------------------------------------------------------------------------------------------------------------------------------------------------------------------------------------------------------------------------------------------------------------------------	----

**CHAPTER 6**

Figure 6.1	Effects of cyclic strain amplitude on the solder joint behavior under SRC conditions. (a) SRC curves of the eutectic Sn-Ag solder joints, and (b) relationship between the maximum shear stress obtained during each cycle and number of cycles .....	100
Figure 6.2	Effects of cyclic strain amplitude on the solder joint behavior under SRC conditions as a function of cyclic strain rate. (a) $\dot{\gamma}_c = 0.00005$ /s, (b) $\dot{\gamma}_c = 0.0005$ /s, and (c) $\dot{\gamma}_c = 0.005$ /s .....	102
Figure 6.3	Effects of cyclic strain amplitude on the solder joint behavior under SRC conditions. (a) SRC curves of the eutectic Sn-Ag solder joints, and (b) relationship between the maximum shear stress obtained during each cycle and number of cycles .....	103
Figure 6.4	Effects of cyclic strain amplitude on the solder joint behavior under SRC conditions as a function of cyclic strain rate .....	104
Figure 6.5	Effects of cyclic strain rate on the solder joint behavior under SRC conditions. (a) SRC curves of the eutectic Sn-Ag solder joints, and (b) relationship between the maximum shear stress obtained during each cycle and number of cycles .....	106
Figure 6.6	Microstructures of the solder joint side surfaces after the SRC tests. All specimens were pre-strained to a $\gamma_p$ of 0.2 and $\dot{\gamma}_p$ of 0.001 /s prior to the first cycle, followed by imposing a fixed $\gamma_c$ of 0.1 and $\dot{\gamma}_c$ 's of (a) 0.00005 /s at 25°C, (b) 0.00005 /s at 85°C, (c) 0.00005 /s	

at 150°C, (d) 0.005 /s at 25°C, (e) 0.005 /s at 85°C, and  
 (f) 0.005 /s at 150°C ..... 107

**Figure 6.7** Microstructures of the solder joint side surfaces after the SRC tests. All specimens were pre-strained to a  $\gamma_p$  of 0.3 and  $\dot{\gamma}_p$  of 0.001 /s prior to the first cycle, followed by imposing a fixed  $\gamma_c$  of 0.1 and  $\dot{\gamma}_c$ 's of (a) 0.00005 /s at 25°C, (b) 0.00005 /s at 85°C, (c) 0.00005 /s at 150°C, (d) 0.005 /s at 25°C, (e) 0.005 /s at 85°C, and (f) 0.005 /s at 150°C ..... 109

**Figure 6.8** Comparison of shear stress versus time plots obtained from stress relaxation part of the test between SR and SRC tests. The specimens were pre-strained to (a)  $\gamma_p$  of 0.2 at  $\dot{\gamma}_c$  of 0.00005 /s, (b)  $\gamma_p$  of 0.2 at  $\dot{\gamma}_c$  of 0.005 /s, (c)  $\gamma_p$  of 0.3 at  $\dot{\gamma}_c$  of 0.00005 /s, and (d)  $\gamma_p$  of 0.3 at  $\dot{\gamma}_c$  of 0.005 /s ..... 111

**Figure 6.9** Shear test results obtained from the specimens tested SRC at various temperatures. All specimens were pre-strained to a  $\gamma_p$  of 0.3 and  $\dot{\gamma}_p$  of 0.001 /s prior to the first cycle, followed by imposing a fixed  $\gamma_c$  of 0.05 and  $\dot{\gamma}_c$  of 0.0005 /s for SRC experiments ..... 114

**Figure 6.10** Relationship between simple shear-strain rate and peak shear stress in each cycle obtained from the stress relaxation part of the test. The specimens were pre-strained to a  $\gamma_p$  of 0.3 at a  $\dot{\gamma}_p$  of 0.001 /s, followed by imposing a fixed  $\gamma_c$  of 0.1 and  $\dot{\gamma}_c$  of 0.005 /s ..... 115

**Figure 6.11** Relationship between peak shear stress in each cycle and testing temperature. The specimens were pre-strained to a  $\gamma_p$  of 0.3 at a  $\dot{\gamma}_p$  of 0.001 /s, followed by imposing a fixed  $\gamma_c$  of 0.1 and  $\dot{\gamma}_c$  of 0.005 /s ..... 117

## CHAPTER 7

- Figure 7.1 Creep activation energy values obtained from  
(a) both low and high temperature regimes, and  
(b) low temperature regime only. The specimens were  
pre-strained to a  $\gamma_p$  of 0.3 at a  $\dot{\gamma}_p$  of 0.01 /s, followed by  
imposing a fixed  $\gamma_c$  of 0.05 and  $\dot{\gamma}_c$  of 0.005 /s ..... 123

## APPENDIX A

- Figure A.1 A schematic of the indentation load/displacement plot  
showing loading, hold and unloading segments ..... 134
- Figure A.2 Microstructures of the as-fabricated solder joints:  
(a) Eutectic Sn-3.5Ag, (b) Sn-4.0Ag-0.5Cu,  
(c) Sn-2.5Ag-0.5Cu-0.5Ni, and  
(d) Sn-2.0Ag-1.0Cu-1.0Ni ..... 136
- Figure A.3 Microstructures of the solder joints after 1000 TMF cycles:  
(a) Eutectic Sn-3.5Ag, (b) Sn-4.0Ag-0.5Cu, and  
(c) Sn-2.0Ag-1.0Cu-1.0Ni solder joints ..... 137
- Figure A.4 Comparison of hardness values of eutectic Sn-Ag  
solder joints with respect to indenter location in  
as-fabricated and after 1000 TMF cycle conditions ..... 141
- Figure A.5 Comparison of hardness values of Sn-4.0Ag-0.5Cu  
solder joints within solder matrix region in as-fabricated  
and after 1000 TMF cycle conditions ..... 144
- Figure A.6 Comparison of hardness values of Sn-Ag-1.0Cu-1.0Ni  
solder joints within solder matrix region in as-fabricated  
and after 1000 TMF cycle conditions ..... 146
- Figure A.7 The overall comparison of the elastic modulus and  
hardness values of the Cu substrate, IMC layer and  
solder matrix region for the four different solder joints in  
as-fabricated condition ..... 148
- Figure A.8 The changes in (a) hardness and (b) relative yield strength  
of solder joints after 1000 TMF cycles ..... 150
- Figure A.9 The variability of (a) hardness and (b) relative yield strength  
values for 250, 500, 1000 cycle thermomechanically fatigued

and then crept solder joints as compared to as-fabricated  
solder joints ..... 151

Figure A.10 The stress exponent for steady-state creep of  
the solder matrix and the interfacial IMC layer for  
as-fabricated Sn-4.0Ag-0.5Cu solder joint.  
The micrographs show the location of the indent  
in the solder joint ..... 152

Figure A.11 The stress exponent for steady-state creep of  
the indent lying on the solder matrix region for  
as-fabricated Sn-4.0Ag-0.5Cu solder joint.  
The micrographs show the location of the indent  
in the solder joint microstructure ..... 153

## **APPENDIX B**

Figure B.1 Microstructures of composite solder joints based on  
eutectic Sn-3.5Ag solder: as-fabricated conditions of  
(a) Cu-composite, (b) Ag-composite, (c) Ni-composite  
solder joints, and (d) four times reflowed Ni-composite  
solder joint ..... 162

Figure B.2 Shear stress versus simple shear-strain plots for  
various composite solder joints at a simple shear-strain  
rate of 0.001 /s at different testing temperatures:  
as-fabricated conditions of (a) Cu-composite,  
(b) Ag-composite, (c) Ni-composite solder joints, and  
(d) four times reflowed Ni-composite solder joints ..... 163

Figure B.3 Shear stress versus simple shear-strain plots for  
various composite solder joints at 150°C at different  
simple shear-strain rates: as-fabricated conditions of  
(a) Cu-composite, (b) Ag-composite, (c) Ni-composite  
solder joints, and (d) four times reflowed Ni-composite  
solder joints ..... 165

Figure B.4 Maximum shear stress as a function of simple shear-strain  
rate at different temperatures: as-fabricated conditions of  
(a) Cu-composite, (b) Ag-composite, (c) Ni-composite  
solder joints, and (d) four times reflowed Ni-composite  
solder joints ..... 166

Figure B.5 Comparison of shear strength of the Cu, Ag, and  
Ni composite solder joints at various temperatures

	along with eutectic Sn-Ag solder joint .....	167
<b>Figure B.6</b>	<b>Microstructures of the composite solder joint side surfaces after shear test with a simple shear-strain rate of 0.01 /s at various temperatures: (a) Cu composite at 25°C, (b) Cu composite at 150°C, (c) Ag composite at 25°C, (d) Ag composite at 150°C, (e) Ni composite at 25°C, (f) Ni composite at 150°C, (g) four times reflowed Ni composite at 25°C, and (h) four times reflowed Ni composite at 150°C .....</b>	<b>169</b>
<b>Figure B.7</b>	<b>Features of the IMCs formed around reinforcing particles within the composite solder joints: (a) Ni composite solder joint with sunflower IMC morphology (specimen deformed to a simple shear-strain rate of 0.1 /s at 85°C), (b) Ni composite solder joint with blocky IMC morphology (enlarged view of Figure B.6 (g); specimen deformed to a simple shear-strain rate of 0.01 /s at 25°C), and (c) Ag composite solder joint (specimen deformed to a simple shear-strain rate of 0.001 /s at 25°C) .....</b>	<b>171</b>
<b>Figure B.8</b>	<b>Schematics of fracture paths in various composite solder joints: (a) Cu composite solder, (b) Ag composite solder, (c) Ni composite solder with sunflower IMC morphology, and (d) Ni composite solder with blocky IMC morphology .....</b>	<b>172</b>
<b>Figure B.9</b>	<b>Relationship between simple shear-strain rate and maximum shear stress: as-fabricated conditions of (a) Cu-composite, (b) Ag-composite, (c) Ni-composite solder joints, and (d) four times reflowed Ni-composite solder joints .....</b>	<b>174</b>
<b>Figure B.10</b>	<b>Relationship between shear stress and testing temperature at different simple shear-strain rates: as-fabricated conditions of (a) Cu-composite, (b) Ag-composite, (c) Ni-composite solder joints, and (d) four times reflowed Ni-composite solder joints .....</b>	<b>175</b>
<b>Figure B.11</b>	<b>Steady-state creep rates of composite solder joints .....</b>	<b>177</b>

# CHAPTER 1

## INTRODUCTION

Lead-based solders, especially Pb-Sn solders, have been used as interconnects in electronic packaging, telecommunications, automotive, and aircraft industries during the past several decades due to their low cost and suitable material properties [1-4]. However, in view of environmental and health concerns, the electronics industry is forced to develop lead-free alternative solders [1,2,4-9]. Alternatives to Pb-Sn solders consist of a variety of lead-free alloys along with some incorporated metallic, non-metallic, and intermetallic reinforcements. Among potential candidates to replace lead-bearing solders, several lead-free solder alloys based on eutectic Sn-3.5Ag solder are being considered as suitable substitutes due to their non-toxicity, higher melting temperatures, and comparable mechanical as well as electrical properties, especially for higher temperature applications [5,10-15]. Eutectic Sn-Ag solder has a melting temperature of 221°C, which is higher than Pb-based systems with a melting temperature of 183°C [1].

Solders are used in various applications such as automobile under-the-hood, aerospace and defense, power generation and distribution, and microelectronics, etc [5]. Several new technologies have made it possible to reduce the size of the electronic packages, and such a miniaturization requires higher package density and increased functionality of electronic devices that warrant good solder joint integrity during service [16]. With advances in surface

mount technology (SMT) and the increasing impetus for micro-miniaturization in emerging technologies employed in the transportation sector, there is a need for solders that can perform in more rigorous environments, where Pb-Sn solders' thermal and mechanical capabilities are exceeded [17,18]. Solders used in automobile under-the-hood applications are subjected to extremely harsh operational environments, where thermal-mechanical loading in static and cyclic manners promote microstructure evolution, creep, fatigue, creep/fatigue damage [19], stress relaxation, crack propagation and fracture [20], therefore requiring solders that are capable of higher performance and reliability [17,21]. Smaller electronic packaging imposes several constraints on the solder interconnect, and necessitates better inherent properties in the solder to resist failure during operation. Hence, it is important to develop a clear understanding of the eutectic Sn-Ag deformation behavior since it is the basis for several lead-free solder alloys that are currently being developed.

One of the most important deformation processes that solder joints experience is thermomechanical fatigue (TMF), wherein the solder material undergoes several cycles of repeated reversed stress states as a consequence of temperature variations and stress relaxation during the dwell periods at the temperature extremes. These stresses, mainly shear, can be induced by mechanical means, but in service environments with temperature excursions it is most often due to the coefficient of thermal expansion (CTE) mismatches between solder/substrate/components. In addition to the effects of temperature extremes imposed, dwell at these temperatures, and ramp-up and ramp-down

during the heating and cooling parts can play significant roles during TMF.

One of the prominent processes that occur in a solder joint during service is creep/stress relaxation, since homologous temperature of the eutectic Sn-Ag solder is greater than  $0.5T_m$  even at room temperature. In addition, the substrate affects the deformation of the solder joint by imposing the mechanical constraint and causing residual stress [22,23]. In order to assess the effect of dwell periods as well as ramp-up and ramp-down on the TMF behavior of such solder joints, evaluation of the stress relaxation process from supplementary tests is necessary due to experimental difficulties of TMF. Stress relaxation tests are useful because the deformation processes involved in the stress relaxation experiments are fairly representative of the stress history experienced by solder joints at the temperature extremes of thermomechanical cycling in service [12]. Therefore, the stress relaxation behavior may be a more realistic experimental approach to assist development of constitutive relationships needed for modeling TMF behavior of solder joints [24].

Reliability losses in many electronic systems were identified with mechanical failure of the solder joint rather than device malfunctions [2]. These concerns have stimulated substantial efforts in the research and development of alternative lead-free solder alloys with reinforcements. Two major approaches, so called an alloying approach and a composite approach, are being pursued to improve mechanical properties of the solder joints. Several studies involve the addition of alloying elements in order to improve the mechanical properties of the eutectic Sn-Ag solder [25-31]. Another way to achieve improvement is to

introduce dispersion of second phase reinforcements into the solder matrix to stabilize the microstructure and thereby enhance its mechanical properties [32-42].

The principal aim of this research is to investigate the fundamental mechanical properties of lead-free eutectic Sn-Ag solder in the joint configuration. The roles of various service related parameters on the stress relaxation behavior of the same solder joints are also evaluated. The results from present study may provide a better understanding of various parameters contributing to TMF behavior of lead-free solder joints.

In chapter two, the review of solder materials as well as solder joints is given in terms of microstructural comparison, TMF, parameters contributing to TMF behavior, and various mechanical properties, including stress relaxation behavior, for an understanding of the roles of TMF parameters.

In chapter three, the mechanical behavior of eutectic Sn-Ag solder joints, in shear, at various testing temperatures is investigated. Microstructural characterization related to the mechanical properties of the same solder joints is also presented.

Chapter four provides the effects of pre-strain, pre-strain rate, and testing temperature on the monotonic stress relaxation behavior of eutectic Sn-Ag solder joints. Possible scenarios for ramp-up and ramp-down situations during TMF cycle are illustrated by using these observations.

In chapters five and six, the roles of various pre-straining and cyclic straining parameters on the stress relaxation behavior of pre-strained eutectic

Sn-Ag solder joints are evaluated at various isothermal conditions. In order to understand the fundamental processes involved under such conditions, cyclic shear straining with associated stress relaxation at the imposed shear strain extremes is carried out. Results from such experiments are compared with findings from monotonic shear straining and stress relaxation tests.

Finally, important observations on fundamental mechanical properties and stress relaxation behavior of eutectic Sn-Ag solder joints are summarized.

In addition, the micromechanical properties of as-fabricated, thermomechanically fatigued, and thermomechanically fatigued and then crept Sn-Ag based alloys using nanoindentation testing (NIT), and the roles of morphological features of the reinforcing phases on the mechanical properties of the Sn-Ag based composite solder joints, are presented in appendices.

## CHAPTER 2

### OVERVIEW

In this chapter, a literature review of eutectic Sn-3.5Ag solder as well as solder joints will be given in terms of microstructural comparison, thermomechanical fatigue (TMF), parameters contributing to TMF behavior, and mechanical properties for an understanding of the roles of TMF parameters.

#### 2.1 MICROSTRUCTURAL COMPARISON BETWEEN BULK SOLDER AND SOLDER JOINT

The bulk eutectic Sn-Ag solder has an equilibrium microstructure consisting of  $\text{Ag}_3\text{Sn}$  intermetallic particles dispersed in a  $\beta\text{-Sn}$  phase with less than 0.04 wt% Ag [43]. However, depending on the cooling rate during solidification process, it shows either essentially pure  $\beta\text{-Sn}$  with rod-like  $\text{Ag}_3\text{Sn}$  intermetallics or primary  $\beta\text{-Sn}$  dendrites with interdendritic eutectic microstructure, which is the mixture of  $\text{Ag}_3\text{Sn}$  particles and  $\beta\text{-Sn}$  phase [4,8,15,44,45].

On the other hand, as-fabricated eutectic Sn-Ag solder joints generally contain the microstructure of primary  $\beta\text{-Sn}$  dendrites with an interdendritic eutectic mixture resulting from the faster cooling rate. Figure 2.1 provides the typical microstructures of the bulk eutectic Sn-Ag solder and the eutectic Sn-Ag solder joint with Cu substrates. Eutectic Sn-Ag solder joint revealed four distinct regions of the Cu substrate, the Cu-Sn interfacial intermetallic compound (IMC) layer, primary Sn-rich phase, and the eutectic Sn-Ag phase. The Cu-Sn interfacial intermetallic phases in IMC layer are  $\text{Cu}_6\text{Sn}_5$  ( $\eta$ -phase) and  $\text{Cu}_3\text{Sn}$  ( $\epsilon$ -

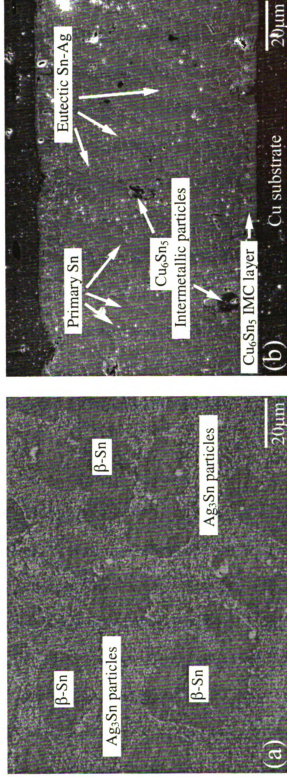


**Figure 2.1** Typical microstructures of (a) bulk eutectic Sn-Ag solder and (b) eutectic Sn-Ag solder joint with Cu substrates.

phase), where  $\text{Cu}_6\text{Sn}_5$  is adjacent to solder and  $\text{Cu}_3\text{Sn}$  is adjacent to Cu [46,47]. The microstructure and composition of the solder joint are altered when it is soldered to a substrate due to the dissolution of the substrate. During soldering of the eutectic Sn-Ag solder with Cu substrates, Cu dissolves in the liquid solder and reacts with Sn, forming  $\text{Cu}_6\text{Sn}_5$  intermetallic dendrites or particles in solder matrix during solidification [15,44,48-50].

The microstructures of bulk solder materials inevitably are different from those of actual solder joints so that mechanical properties are quite different as well. The deformation behavior of the solder joint becomes more complicated due to the complexity of microstructure of the solder joints, such as substrates, interfacial IMC layer, IMC particles within the solder matrix, etc., as compared to bulk solder. Also, due to the constraints imposed on the solder in the joint configuration, mechanical response of the solder joint will be different from that of bulk solder.

## **2.2 THERMOMECHANICAL FATIGUE (TMF)**

TMF is one of the most important deformation processes that solder joints experience in service condition. TMF of solder joints appears when temperature fluctuations are encountered during operation, imposing cyclic strains in the solder joints due to coefficients of thermal expansion (CTE) mismatch. It is generally believed that the TMF behavior of solder materials is controlled by creep-fatigue mechanisms since the solder alloys experience high homologous service temperatures. During turning on and off operations of the electrical

circuitry when heat up or cool down, they also experience low cycle (thermomechanical) fatigue due to stresses that develop as a consequence of CTE mismatch between the solder/substrate/components. Several extensive failure analysis studies have shown that the primary cause of solder joint failure in the electronics industry is a low cycle fatigue failure of the solder joint [51]. Severe thermal environments, such as space and avionics systems requiring numerous thermal cycles with extreme temperature variations, can create severe solder joint stresses resulting in low cycle fatigue failure of the joint. The behavior of the solder alloy and joint throughout a thermal cycle is quite complicated as depicted in Figure 2.2. For example, at ramp up situation (elevated temperatures) in the cycle, the joint is significantly weaker, as creep and stress relaxation of the solder occur rapidly. Thus, joint stresses are reduced. At lower temperatures in the thermal cycle, the joint is stronger as stresses are sustained with much slower relaxation or creep. Thus, stresses are higher. The evolution of microstructure which occurs during thermal cycling cannot be ignored either, especially during the ramp up excursion and the elevated temperature dwell period. Since TMF resistance is difficult to measure directly, either isothermal cyclic fatigue test or thermal cycling test for modeling the TMF resistance was used in many studies.

Solomon [49] carried out isothermal fatigue experiments on eutectic Sn-Ag solder joint made by soldering together two brass or Cu blocks, and compared fatigue behavior of this solder to that of eutectic 60Sn-40Pb solder and 92.5Pb-2.5Ag-5.0Sn solder. The experiments were run under total strain control, and

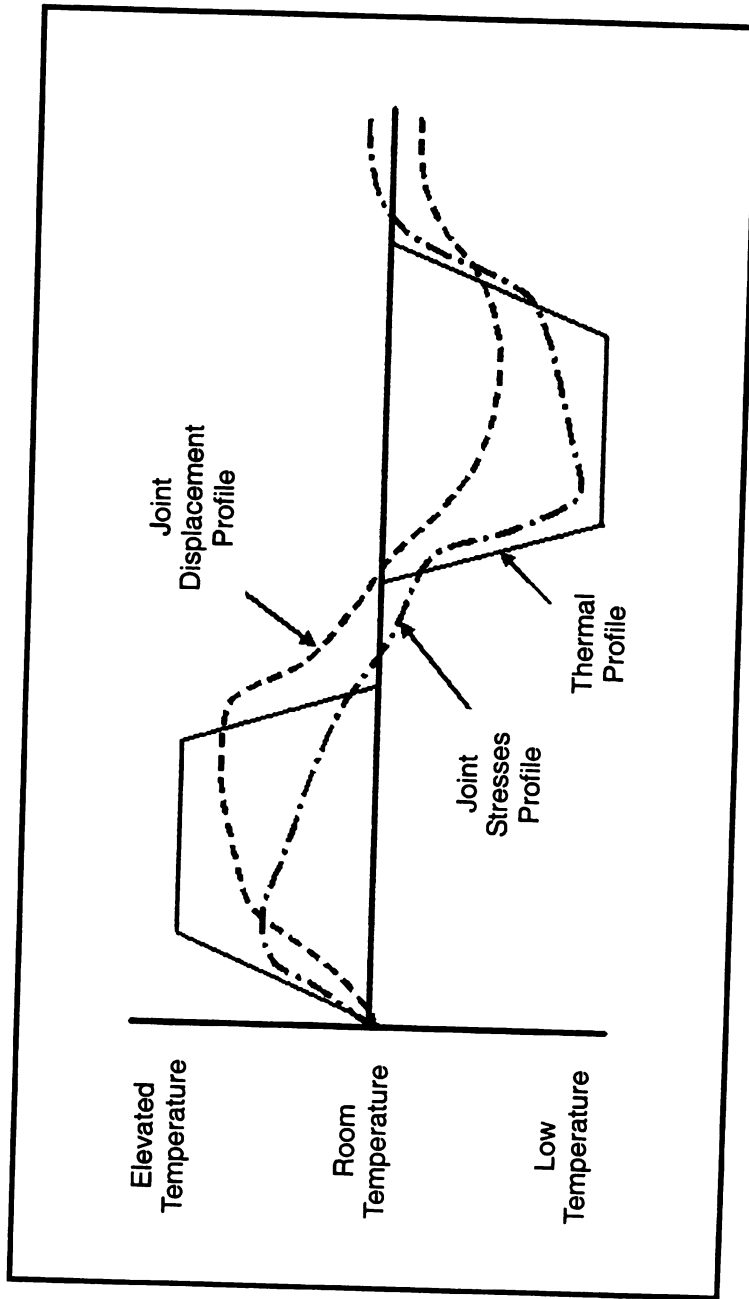


**Figure 2.2** The behavior of the solder alloy and joint throughout a thermal cycle [51].

the loading was done with equal positive and negative plastic strain limits, with equal loading rates. A cycling frequency of ~ 0.3 Hz was used, and the tests were run at either 35°C or 150°C. The author used the drop in the hysteresis load as a measure of fatigue cracking and this can also be used as a measure of fatigue failure. The number of cycles to failure was decreased with increasing plastic strain range, following Coffin-Manson low cycle fatigue law, *i.e.*

$$N_f^\alpha \Delta\gamma_p = \theta$$

where, ' $N_f$ ' is the cycles to failure, ' $\alpha$ ' is the Coffin-Manson low cycle fatigue exponent, ' $\Delta\gamma_p$ ' is the plastic strain range, and ' $\theta$ ' is constant in the Coffin-Manson low cycle fatigue law. The hysteresis load drop is characterized by the load drop parameter,  $\phi$ , given by,

$$\phi = 1 - (\Delta P / \Delta P_M)$$

where, ' $\Delta P$ ' is the load range at any number of cycle and ' $\Delta P_M$ ' is the maximum load range observed in the first cycle. The author found that the load drop parameter is a linear function of number of cycles following,

$$\phi = AN^B$$

where, ' $N$ ' is the number of cycles, and ' $A$ ' and ' $B$ ' are the constants representing the intercept and the slope of this relationship respectively. For plastic strain ranges between 1 to 10 percent, fatigue life of eutectic Sn-Ag solder was generally greater than that of 60Sn-40Pb solder or 92.5Pb-2.5Ag-5.0Sn solder.

Guo *et al.* [52] performed isothermal monotonic and low cycle fatigue tests in shear at 300 K on various solder alloys (Sn-42Bi, Sn-43Pb-14Bi, Sn-39.6Pb-

1.1Sb, Sn-35Pb-10In, and Sn-4Ag), and compared with 63Sn-37Pb alloy. Triangular wave type fatigue tests were conducted under constant total shear strain control, completely reversed ramp cycling, and cycling frequency of 0.1 Hz. The monotonic shear test data up to  $\tau_{\max}$  were in accord with the Ludwik-Holloman equation, *i.e.*

$$\tau = K\gamma^n$$

where, ' $\tau$ ' is the shear stress, 'K' is the strength coefficient, and 'n' is the strain hardening exponent. The data from cyclic fatigue tests were also found to follow the Coffin-Manson low cycle fatigue law. The Sn-4Ag alloy had the highest fatigue resistance at the largest strain ranges, but it had among the least resistance at the smallest strain ranges.

Mavoori *et al.* [53-55] compared isothermal fatigue related properties of the eutectic Sn-Ag and Sn-9Zn alloy systems with those of Sn-Pb eutectic solder. The specimens were heat treated at 150°C for 24 hours followed by aging at room temperature for 6~10 days. The isothermal fatigue tests were run on bulk specimens at 25°C and 80°C under total-strain control with uniaxial loading using triangular strain waveforms. The ramp time was fixed at a cycling frequency of 0.5 Hz with and without hold time at maximum strain. In the test without hold time, the eutectic Sn-Ag solder was observed to fail at a greater number of cycles than eutectic Sn-Pb solder in the total strain range investigated (0.002 ~ 0.02), and followed the Coffin-Manson type relation. In the test with hold time at maximum strain, small increases in hold time cause drastic reduction in the number of cycles to failure, but beyond a critical hold time there was no further

reduction. The effect of increasing testing temperature and decreasing frequency was to reduce the number of cycles to failure.

The linear relationship between the strain range and the logarithm of the cycles to failure defined in Coffin-Manson equation has been demonstrated with numerous isothermal and thermal fatigue experiments. However, it has been shown experimentally that various parameters such as the frequency of temperature cycling, temperature extremes, ramp rate, dwell times, and the magnitude of the strain range etc. can influence the number of cycles to failure. It has become apparent that this simple model is an over-simplification, and for more accurate life predictions, a more accurate model is needed. Winterbottom [5] introduced several results of significance in the strain mapping produced by the simulation using nonlinear finite-element analysis. The first feature is that the distribution of the accumulated strain in the joint was inhomogeneous and highly localized depending on the joint geometry. This does not support the uniform strain assumption used in the Coffin-Manson relation. The localized strain accumulation at certain locations of the joint suggested that the crack initiation and propagation processes would be more appropriate for predicting lifetime than an approach assuming uniform strain based on global displacements. Secondly, the deformation produced during the heating and cooling regimes of the thermal cycling was not reversible but produced continually changing distortions and stress distributions. As a result, the joint shape and the stress distribution changed irreversibly as well. This behavior implied that isothermal fatigue testing cannot be expected to exactly replicate the

failure mechanism, *i.e.* the cracking trajectory, induced by thermal cycling. Thirdly, the comparison of the time-independent plastic deformation and the time-dependent creep deformation provided insight into the cracking process for the fatigue fracture. The crack trajectory in the joint was found to pass through the regions having greatly accumulated plastic strain and very little creep strain. With inputs from the study on deformation process, a failure criterion was taken as follows. Once a critical strain density is reached at a location in the joint, a crack is nucleated and extended. The solder joint will fail when the cracked area reduces the joint strength below that required to support the imposed load.

## **2.3 PARAMETERS CONTRIBUTING TO TMF BEHAVIOR**

### **2.3.1 Overview (TMF Cycling)**

The stress generated within the solder joint depends on the value of the imposed thermal strain. To increase joint reliability there exists a need to understand the aspects that lead to failures in solder joints. This need can be met by the experimental testing of solder joints under conditions of TMF. This work can be divided into three types of testing terms: thermal cycling of components, isothermal fatigue, and thermal fatigue of simplified test specimens [56].

Thermal cycling of components involves imposing thermal cycles on actual components soldered to printed circuit boards (PCBs). Strain is imposed by the difference in CTE between the component and the board. The main advantage of this technique is that the fatigue resistance can be directly evaluated from a

given assembly system by monitoring the number of cycles to failure. However, this method has two major disadvantages that the strain state is too complicated in the joints, and stress measurements are impossible. There are three ways by which thermal cycles may be applied: thermal shock, thermal cycling, and power cycling. In thermal shock mode, the solder joints are cycled with extremely short ramp times and some hold time at the temperature extremes, resulting in very rapid deformation rate due to the rapid transfer of heat. So, this method cannot account the effect of ramp rates during the heating and cooling parts of the test, which is one of the important parameters contributing to TMF behavior. In thermal cycling mode, the solder joints are cycled with a moderate ramp rate to temperature extremes. Heat transferred to system and the deformation rate is slower than that in thermal shock mode, resulting in reduced possibility of damage of the solder joints during testing. Power cycling is conducted by turning power electronic device on and off. Kubik and Li [57] found thermal shock was the least conservative of the three where thermal shock yielded a longer life than thermal cycling. Power cycling is very important for consumer applications such as computer and home appliances since components are turned on and off in an ambient environment [58].

Isothermal fatigue is mechanically induced strain-controlled fatigue at a constant temperature. In isothermal fatigue method, the testing procedure and analysis are much simpler than those in thermal cycling, and stress can be simply measured. However, this method also has some disadvantages. Firstly, the test results widely vary with respect to the specimen design. For example,

bulk samples do not behave the same as joints, nor do they deform solely in shear. Secondly, it is virtually impossible to determine when a joint has failed. Electrical detection of failure is difficult because the entire specimen is conductive. Finally, the microstructure that develops during isothermal fatigue differs greatly from that found in thermal fatigue.

In thermal fatigue of simplified test specimens method, solder joints are constrained between two materials having different CTE. By cycling between two temperature extremes simple shear is imposed on the joint tested. The advantage of this method is that the joint is under a simple shear state. However, direct detection of the number of cycles to failure is impossible like in case of isothermal fatigue testing.

To simulate and obtain an accurate TMF database, testing of solder joints has to satisfy the following conditions:

- 1) test in a simple shear orientation
- 2) collect mechanical properties data during testing
- 3) accurately determine the number of cycles to failure
- 4) be able to quantify the microstructural changes of the solder joints.

### **2.3.2 Parameters Contributing to TMF Cycle**

In addition to the effects of methods of thermal cycles, temperature extremes imposed, dwell at these temperatures, and rates of ramp-up and ramp-down during the heating and cooling parts can play significant roles during TMF. Figure 2.3 shows the typical temperature-time profile experienced by solder joints

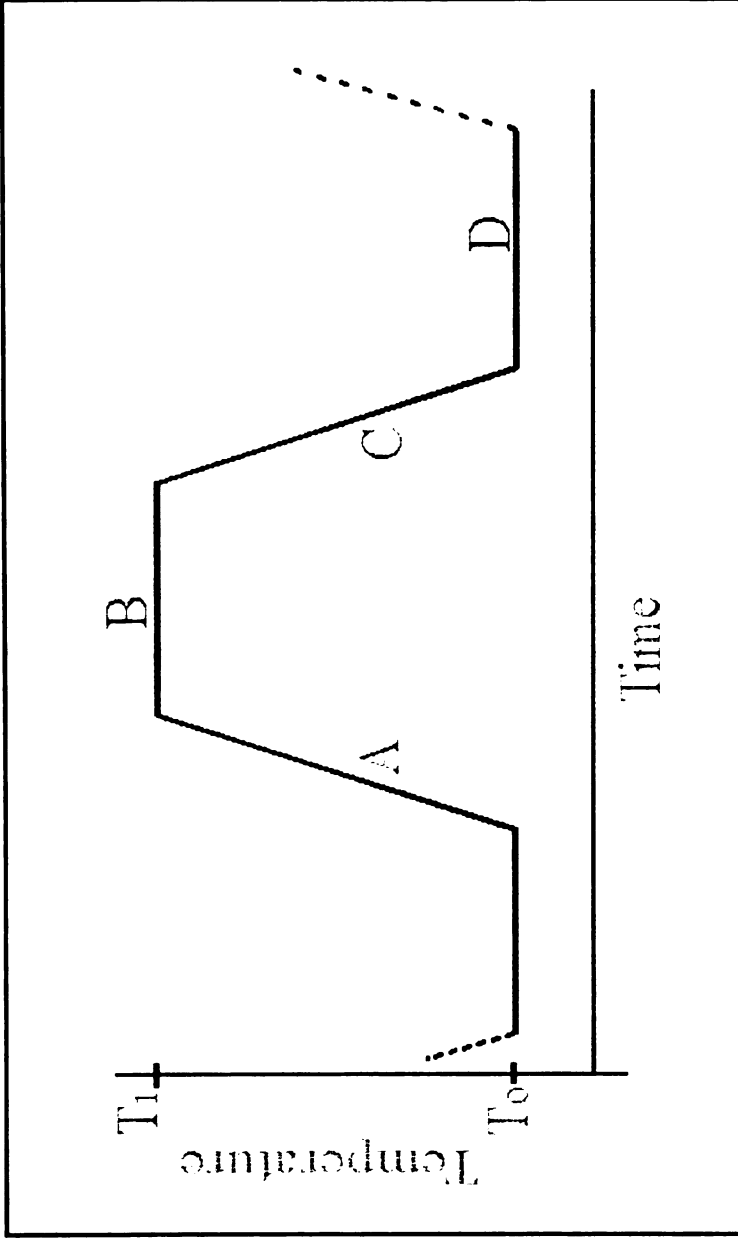


**Figure 2.3** The typical temperature-time profile experienced by solder joints in service condition.

in service condition. Temperature extremes ( $T_0$  and  $T_1$ ), dwell times at temperature extremes (B and D), and temperature excursions (A and C) are important factors contributing to TMF behavior of the solder joints.

Dwell periods ranging from several hours to several days at a relatively constant temperature are a normal part of the functioning of an electronic package [59]. The total fatigue life of solder joints is most dramatically affected when dwell periods occur at the temperature extremes. In addition, dwell periods which produce tensile stresses in the solder joints tend to be more damaging than dwell periods producing compressive stresses in the solder joints due to the formation of grain boundary voids [60,61]. When comparing fatigue cycles with and without dwell periods at the temperature extremes, the dwell-containing cycles have a considerably stronger influence on the overall fatigue life of the electronic package. Even if the cycle frequencies are the same, inelastic deformation accumulates at a slower rate during the tensile dwells as compared to cycles where the applied strain is always changing. As a result, the heterogeneous accumulation of concentrated damage between adjacent grains is more likely during tensile dwells than during forward loading. During the periods where temperature or mechanical strain is actively changing, deformation is distributed more uniformly over the bulk of the grain than when the total strain is held constant.

Significant damage accumulation occurs during TMF causing deterioration of residual mechanical properties [62,63]. The effect of dwell times has been characterized by observing the surface damage and residual mechanical

properties of solder joint. However, the effects of thermal strains resulting from CTE mismatches and temperature changes, and the rate at which this strain is imposed depending on ramp-rates have not been investigated. These rates may play significant roles in the TMF process since solder exhibits significant high strain-rate sensitivity both at low and high temperatures.

## **2.4 MECHANICAL PROPERTIES FOR AN UNDERSTANDING OF ROLES OF TMF PARAMETERS**

It is important to evaluate various mechanical properties of Sn-based solder joints to gain a better understanding of above TMF parameters. Moreover, the reliability of solder joints often depends directly on the mechanical properties of the solder alloy as well as joints.

### **2.4.1 Mechanical Properties Test**

When an electronic device is in operation, the solder connections are subjected to mechanical stresses and strains due to the CTE mismatch between electronic component and the board. The solder joint can be subjected to tensile loading, typically when the board or substrate is bent. During its service life, solder joints in microelectronics systems also experience shear loading most of the time. The tensile/shear properties are therefore necessary to determine the extent of mechanical deformation of the solder connection that can withstand without failure. Throughout the reported literature, the dependence of those properties on the strain rate and test temperature is evident. This strong dependence is reasonable because the solder alloys are typically at a high

homologous temperature even under room temperature conditions. So, thermally activated processes such as diffusion and creep have sufficient activation energy to occur.

The main objective of those mechanical tests, especially time-independent stress/strain test, is to establish a general material properties database. This could provide inputs to models for other mechanical properties such as creep resistance, fatigue strength, rigidity, etc., which are sufficient to ensure the reliability of solder joint in an electronic device. The development of a constitutive model for predicting the TMF of solder interconnects requires the measurement of time-dependent mechanical properties. Tensile and shear strength of the alloy determines the resistance of the joint to mechanical rupture under short term direct loading.

Although several studies on mechanical properties of lead-bearing as well as lead-free solders have been reported in the literature [4,11,12,24,49,51,56], most of these investigations have been carried out on bulk tensile solder specimens, in the absence of the constraint effects present in a joint configuration.

#### **2.4.2 Stress Relaxation Test (Residual Mechanical Properties)**

Stress relaxation is the time-dependent deformation of a material under constant constraint (*i.e.* total strain) conditions. Although the total strain is constant throughout the stress relaxation test, the plastic (or permanent) strain within the material increases with time at the expense of the recoverable strain.

Consequently the rate of plastic deformation of the material during stress relaxation is not zero but a function of stress, temperature, and time. The deformation mechanisms within the material that occur during stress relaxation are the same as those occurring during creep for the same strain rates. A mathematical model can be used for creep and stress relaxation which incorporates the Arrhenius model to describe the effect of temperature. These models often use an empirical power law to predict the effect of stress on the plastic strain rate of the material, *i.e.*

$$\dot{\gamma} = A \tau^n \exp\left(\frac{-Q_c}{RT}\right)$$

where, ' $\dot{\gamma}$ ' is the steady-state shear-strain rate in creep, 'A' is the material constant, ' $\tau$ ' is the shear stress, ' $n$ ' is the stress exponent that depends on operating creep mechanisms, ' $Q_c$ ' is the creep activation energy, 'R' is the gas constant, and 'T' is the absolute temperature.

In TMF at high homologous temperatures, both thermal and athermal processes are active. At low strain rates or high temperatures, creep dominates; however, at high frequencies or low temperatures, failure is dominated by athermal processes as creep has little time to act. During the low temperature extreme of a TMF cycle, there is less stress relaxation than during the high temperature extreme of the cycle due to lower thermal energy. During stress relaxation tests, the deformation processes involved are closely representative of those in an actual solder joint during the temperature hold periods of the actual TMF cycle during operation of the electronic device. This

makes the stress relaxation test more suitable for reliability modeling than creep tests [24]. In other words, evaluation of the stress relaxation process is necessary to assess the effect of dwell periods on the TMF behavior of such solder joints. Also, it is able to account for residual stress in stress relaxation and should be useful in incorporating time-dependent effects into numerical techniques for solder joint analysis and reliability prediction.

Compressive stress relaxation was studied in four hyper-eutectic Sn-Pb alloys (29, 37, 54, and 60% Sn) to establish parameters for an analytical model which can be used at very low strain rates, by Baker [64]. At these low strain rates the activation enthalpy and the stress exponent were found to be 67 kJ/mol and 3.4, respectively.

Arrowood and Mukherjee [65] carried out stress relaxation tests involved loading the eutectic Sn-Pb bulk specimen by constant-velocity compression to a predetermined load, and then stopping the cross-head and recording the load as a function of time. When this alloy was subjected to stress relaxation from a high stress, it displayed a threshold-like behavior which is a reflection of superanelasticity. When relaxed from a low stress level, the material displayed no threshold and mimics the creep behavior, except that the stress sensitivity is slightly higher than that from creep experiments.

Stress relaxation experiments were performed on cast tensile specimens of commercial eutectic Sn-Pb solder at 25°C, 50°C, 75°C, 100°C, and 125°C, by Hare and Stang [24]. They analyzed the stress relaxation data to extract constitutive relations for creep. The strain rate during relaxation was found to

follow two power law expressions. The results showed an apparent activation energy of 69 kJ/mol and stress exponent of 3.2 in the low stress regime, suggesting that the rate controlling mechanism in the low stress regime is viscous dislocation glide. In the high stress regime, the activation energy was found to be 64 kJ/mol and the stress exponent was 6.2, suggesting that the rate controlling mechanism is dislocation climb controlled creep in the high stress regime.

Mavoori *et al.* [12] performed stress relaxation tests under constant-strain conditions with strains in the range of 0.3-2.4% and at 25°C and 80°C for two eutectic lead-free solders (96.5Sn-3.5Ag and 91Sn-9Zn). At 25°C, most of the stress was seen to relax rapidly in less than 120 seconds for both Sn-Ag and Sn-Zn eutectic. The stresses did not reduce all the way to zero, but leveled off at non-zero values. The stress relaxation thereafter was found to be insignificant over a period of 24 hours. At 80°C, however, the stresses relaxed completely to zero in less than 24 hours for all the cases. They suggested the operation of two mechanisms, the first with an activation energy low enough to cause relaxation at both temperatures, and the second mechanism which comes into operation at 80°C allowing relaxation of stresses all the way to zero.

Stress relaxation tests were performed to both eutectic Sn-Ag and Sn-Ag based composite solder joints at 25°C and 150°C, by Jadhav *et al.* [66] The magnitude of the stress drop during relaxation depended primarily on the plastic shear strain imposed prior to the stress relaxation process. The stress in single shear-lap joints did not relax to zero stress, as was observed in stress relaxation

of bulk tension specimens in case of Mavoori *et al.* The stress exponent values calculated from the stress relaxation test were consistent with conventional creep data.

Woodmansee and Neu [67] investigated the prior deformation history-dependence of the stress relaxation behavior of 60Sn-40Pb, 96Sn-4Ag, and 96.2Sn-2.5Ag-0.8Cu-0.5Sb bulk specimens. These solder alloys exhibited short-term prior strain rate dependence during stress relaxation. Higher prior strain rates led to higher initial stress levels prior to stress relaxation and these increased prior strain rates caused these alloys to relax to lower stress levels.

As in mechanical tests, most of the stress relaxation investigations have also been conducted on bulk tensile solder specimens without considering the constraint effects present in a joint configuration. Also, there is no systematic study on the effects of pre shear-loading conditions and temperature on the stress relaxation behavior of eutectic Sn-Ag solder in the joint configuration. Recent publications [68,69] on the repeated reverse straining and stress relaxation properties of lead-free solder using joint configuration have been carried out at room temperature.

Chen *et al.* [68] designed a large sized solder joint geometry by joining three rectangular copper blocks with two symmetrical eutectic Sn-Ag solder joints in a Y-shaped configuration. The specimens were tested in shear at room temperature with an Instron tensile tester at a displacement rate of 0.5 mm/min. The samples were first loaded in tension to a predetermined strain to avoid any mechanical slack during testing. Different hold times at the extreme strains

were employed for stress relaxation studies before applying shear in the reverse direction. Thus, cycling between maximum shear strain and minimum shear strain was performed. They picked stress relaxation data from hold times at the maximum strain amplitude only since hold times at the minimum strain extreme was found to always result in a very small increase in load. They reported that continued cycling of reverse shearing resulted in additional damage accumulation with the striations (or shear bands) became more intense, and stress relaxation decreased much more rapidly with cycling since each application of reversed stress contributes to microstructural damage. The magnitude of stress relaxation decreased with each successive cycle, but full relaxation to zero load was not achieved with the constrained samples as observed by Jadhav *et al.* [66]. The maximum stress decreased with each successive cycle since microcracks may have developed during the repeated reverse shear.

The surface deformation and mechanical behavior of specimens with different solidification microstructures that underwent reverse shear straining with stress relaxation at the extreme strains were analyzed by Ferguson *et al.* [69] using a same solder joint geometry with Chen *et al.* [68]. The solder joints were cooled down from the peak soldering temperature by controlling cooling rates to fabricate three different solidification microstructures of air-cooled, water quenched, and iced-brine quenched. The faster the cooling rates the less dendrite formation of Sn-rich cells. Surface damage can be intensified at larger strain amplitude and a larger number of cycles imposed. Extensive damage

was observed in the specimen cycled with a longer hold time at the strain extreme. No significant drop in stress was found for specimens cycled at a smaller shear strain amplitude, and the water-quenched specimens exhibited the highest shear stress for a given strain amplitude.

However, these investigations [68,69] used a solder joint thickness of about 700  $\mu\text{m}$ , while a typical joint thickness in electronic application will be about 100 ~ 200  $\mu\text{m}$ , and tested only at room temperature that can not be representative of actual service environments.

### **2.4.3 Nanoindentation Test**

The conventional approach for assessing the mechanical behavior of solder materials such as tension, compression, hardness, creep, fatigue testing etc. cannot be readily used to study the micromechanical properties of actual microelectronic solder joints because of size constraints. Furthermore, the microstructure of the joint is significantly different as compared to bulk solder materials. This could be the most challenging issue to investigate the micromechanical properties of alloyed and composite solder joints since the microstructures of those solder materials are much more complicated. Submicron indentation testing represents an alternative approach [21,70]. By measuring the force and the indent depth of indentations made in actual solder joints, it is possible to obtain information about the elastic and plastic deformation properties of the solder joints. Submicron indentation provides information about the micromechanical properties and deformation processes of solder joints

that cannot be obtained easily by other means [21,71].

#### **2.4.4 Alloying/Composite Solders**

Several approaches have been reported to improve the overall properties of various solders including Sn-based solders such as mechanical strength, creep resistance, thermomechanical fatigue resistance, and solder joint reliability, etc. [25-31]

##### **2.4.4.1 Alloying Solders**

Adding alloying elements to solders is one methodology reported by some researchers to improve the mechanical properties of solders as well as solder joints [25-31].

McCormack and Jin [4] observed the effect of alloy additions on Sn-3.5Ag-Zn and Sn-9Zn-In solders. In Sn-3.5Ag-Zn alloy system with different Zn additions, all compositions with the ternary Zn additions to the eutectic Sn-Ag solder exhibited significant increases in both 0.2% offset yield stress and ultimate tensile strength, reaching a peak strength at 1 wt.% Zn. At 1 wt.% Zn, the microstructure appeared to be uniform and remarkable creep resistance was exhibited. The improvements of mechanical properties were interpreted in terms of microstructural refinement. The Zn addition suppressed dendrite formation of soft Sn phase and refined  $Ag_3Sn$  particles, resulting in very fine and uniform microstructure. In Sn-9Zn-In alloys with 5 and 10 wt.% additions of In, the creep resistances of both alloys were vastly superior to that of the Sn-Pb

eutectic. Indium additions also improved both the wetting force and the wetting speed compared to the binary Sn-Zn eutectic.

McCormack *et al.* [29] also examined two ternary alloys, Sn-3.5Ag-5In and Sn-3.5Ag-5Bi, produced by incorporating In or Bi into Sn-3.5Ag solder. They obtained a reduced melting temperature of 213°C and 212°C for the In and Bi additions, respectively. Both types of additions strengthened the alloys at small strains, but they severely degraded the strain that the alloy can withstand, showing a brittle fracture. This was attributed to the segregation of In and Bi in Sn phase.

Kariya *et al.* [30] investigated the effects of Cu and Bi on Sn-3.5Ag solder with up to 1% Cu and 5% Bi addition during TMF using actual solder joint with Quad Flat Pack (QFP) leads. They found that the increased addition of Bi drastically degraded the thermal fatigue resistance of Sn-3.5Ag solder, attributing to the formation of Bi precipitates in Sn phase when Bi more than the solubility limit of 2 mass% in Sn was added. The Cu addition did not change significantly the thermal fatigue property of the Sn-3.5Ag solder.

#### 2.4.4.2. Composite Solders

The composite approach is another potential methodologies to improve the properties of lead-free solder joints. Mechanical behavior of composite solder joints depends on the reinforcing phases present. Such reinforcements can be introduced by *in-situ* methods or by mechanical means. Choices of such reinforcements serve several purposes. Proper choice of foreign reinforcement

additions could desirably introduce uniformly distributed intermetallic hard particles and/or non-coarsening particles. Well-dispersed reinforcements can serve as obstacles to grain growth, crack growth and dislocation motion so as to strengthen the solder against creep and fatigue deformation by promoting homogeneous deformation [4].

McCormack *et al.* developed composite solders by adding 2.5 wt.% of magnetic Fe powders into eutectic Bi-Sn solder [4]. Fine, essentially insoluble dispersoid particles were uniformly distributed in the Bi-Sn eutectic solder to suppress creep deformation, inhomogeneous shear, and microstructural coarsening. Using magnetically aligned dispersions, remarkably improved strength and creep resistance have been achieved. This composite solder exhibited more than 5 times the creep resistance and at least 10% more tensile strength compared to the Fe-free sample.

Sastry *et al.* also prepared dispersion strengthened *in-situ* composite solders of Sn-Pb-Ni and Sn-Pb-Cu alloys containing 0.1 - 1.0  $\mu\text{m}$   $\text{Cu}_6\text{Sn}_5$  or  $\text{Ni}_3\text{Sn}_4$  intermetallic dispersoids [35].  $\text{Cu}_6\text{Sn}_5$  or  $\text{Ni}_3\text{Sn}_4$  intermetallic dispersoids were produced by reaction between Cu or Ni particles added to the solder alloy. An increase of 25-180% in yield stress and 20-80% in the modulus values were noted compared to eutectic Sn-37Pb solder.

Marshall *et al.* have carried out studies in microcharacterization of composite solders [38-40]. Their composite solders were primarily prepared by mixing  $\text{Cu}_6\text{Sn}_5$  (10, 20, 30wt%),  $\text{Cu}_3\text{Sn}$  (10,20, 30wt%), Cu (7.6wt%), Ag (4wt%), or Ni (4 wt%) particles with the eutectic Sn-37Pb solder paste. Microstructural

analysis showed good bonding of the particulate reinforcements to the solder matrix. Their subsequent solderability tests concluded that the solderability was improved when the concentration of the reinforcements is low [41]. Mechanical property tests of the composite solders generally revealed an improvement in tensile strength without loss of ductility.  $\text{Cu}_6\text{Sn}_5$ ,  $\text{Cu}_3\text{Sn}$ , and Ag particle reinforced composite solders showed better mechanical performance than Cu and Ni reinforced composite solders with a high degree of internal porosity [42].

## CHAPTER 3

### MECHANICAL CHARACTERIZATION OF EUTECTIC Sn-3.5Ag SOLDER JOINTS AT VARIOUS TEMPERATURES

#### ABSTRACT

In order to investigate the mechanical behavior of eutectic Sn-Ag solder (Sn-3.5Ag in wt%) joints, deformation studies on such solder joints were carried out at a range of temperatures using a Rheometric Solids Analyzer (RSA-III). Various performance parameters were evaluated with this equipment by subjecting geometrically realistic solder joints to shear loading at various temperatures (25°C, 75°C, 100°C, 125°C, and 150°C) with a nominal joint thickness of ~ 100µm and 1mm × 1mm solder joint area. Mechanical properties, such as shear stress versus simple shear-strain relationships, peak shear stress as a function of simple shear-strain rate and testing temperature, and creep parameters, were evaluated to gain a better understanding of the parameters contributing to thermomechanical fatigue (TMF).

### **3.1 INTRODUCTION**

Lead-based solders have been used as interconnects in electronic packaging, telecommunications, automotive, and aircraft industries over the past few decades [1]. However, in view of environmental and health concerns, the electronics industry is being forced to develop lead-free alternative solders [1,7-9]. Several lead-free solder alloys based on eutectic Sn-Ag solder are being considered as suitable substitutes for the Sn-37Pb solder due to their non-toxicity, higher melting temperatures, and comparable mechanical/electrical properties especially for higher temperature applications [5,10-15]. Several new technologies have made it possible to reduce the size of the electronic packages and such a miniaturization requires a higher interconnection density. The increased functionality of electronic devices also requires good solder joint integrity [16]. Smaller electronic packaging imposes several constraints on the solder interconnect and necessitates better inherent properties in the solder to resist failure during operation. It is therefore important to develop a clear understanding of the solder deformation behavior and fracture mechanisms.

One of the most important deformation processes that solder joints experience during service is thermomechanical fatigue (TMF), wherein the solder material undergoes several cycles of repeated reversed stress states and stress relaxation as a consequence of temperature variations. The stresses can also be induced by mechanical means, but in service environments with temperature excursions, fatigue is most often due to the coefficient of thermal expansion (CTE) mismatches among solder, substrate, and component. These CTE

mismatches particularly result in shear stresses. Other service parameters that influence TMF include the temperature extremes, heating/cooling rates, and dwell times at the temperature extremes. These parameters play significant roles in the rate of damage accumulation during service.

Other prominent deformation processes occurring in a solder joint during service are creep and stress relaxation, since the homologous temperature of eutectic Sn-Ag solder is greater than  $0.5T_m$  even at room temperature. There have been studies characterizing isothermal creep behavior using bulk and joint configurations for this solder [12,13,72-76]. However, the stresses that develop during heating and cooling parts of the TMF cycle will depend on the rate at which these temperature changes occur, and the compliance of the solder material at the temperature extremes which will control the rate of dissipation of such stresses by relaxation.

Several studies of the mechanical properties of lead-bearing as well as lead-free solders have been reported in the literature [4,11,12,76-78]. However, most of these investigations have been carried out on bulk tensile solder specimens, in the absence of the constraint effects present in an actual joint configuration. Also, there have been no systematic studies of the effect of strain-rate and temperature on the mechanical behavior of eutectic Sn-Ag solder in the joint configuration.

The objective of the present research is to use a thermal/mechanical analyzer to investigate the behavior of lead-free eutectic Sn-Ag solder joints using sub-millimeter size solder joints, in shear. The findings from this study

should serve to provide a better understanding of the various parameters contributing to the thermomechanical properties of lead-free solder joints.

### **3.2 EXPERIMENTAL PROCEDURES**

Single shear-lap solder joints were fabricated by soldering two dog-bone shaped copper strips together using a binary eutectic Sn-Ag solder paste material obtained from a commercial source. The schematic of the solder joint configuration and the joint making fixture is depicted in Figure 3.1. Copper dog-bone specimens were made by electro discharge machining (EDM) from a 0.5mm thick copper sheet, and cleaned in a 50% Nitric acid ( $\text{HNO}_3$ ) solution to remove the oxide layer at soldering area. The dog-bone specimens were then placed in the aluminum solder making fixture with glass plates which eliminate the need for a mask that was required in previous studies [21,50,55,56,59,72-75,79-91]. Once the lower dog-bone piece and a glass plate were laid in the fixture, the solder paste was placed on top of the free copper surface. The upper dog-bone piece was then placed on top with another glass plate, and the entire assembly was placed on a pre-heated hot plate. The temperatures of solder joints during joining operation were monitored by a thermocouple attached to the aluminum fixture. Since aluminum has very high thermal conductivity, it was assumed that the temperatures of the aluminum fixture were nearly the same as those of the solder joints during joining operation. The assembly was kept on the hot plate until the temperature reached 250°C, which is higher than the melting point of eutectic Sn-Ag solder and commercially used temperature for

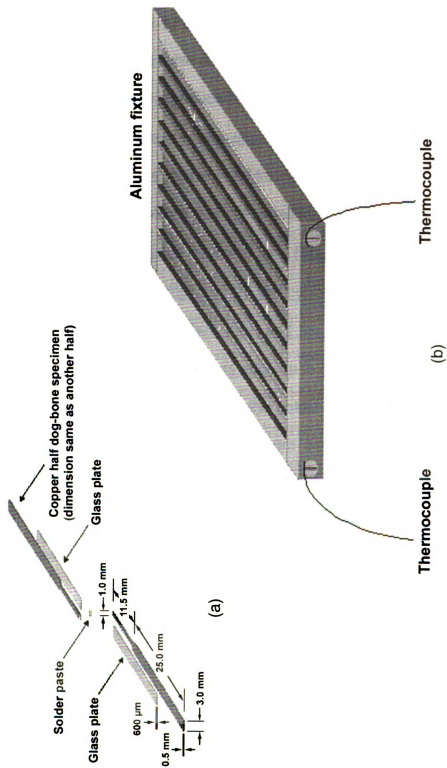


**Figure 3.1** A schematic illustration of (a) a single shear-lap joint and (b) joint making fixture used in this study.

fabricating eutectic Sn-Ag solder joint. After that the entire assembly was removed from the hot plate to an aluminum chill block to cool down to room temperature. The thermal profile for solder joint fabrication is shown in Figure 3.2. This method can easily produce the solder joint area of  $1\text{mm} \times 1\text{mm}$ , and the desired solder joint thickness with reasonable consistency by using a glass plate of proper thickness as a spacer. Additional details on specimen fabrication can be obtained from elsewhere [92]. For example,  $600\mu\text{m}$ -thick glass plates were used to make solder joint thickness of  $\sim 100\mu\text{m}$  in this study. Soldering was confined to the volume enclosed by the copper substrates and the glass plates. The solder joint was  $100\mu\text{m}$  thick and the copper dog-bone thickness was  $500\mu\text{m}$ . Hence, the total thickness adds up to  $600\mu\text{m}$ . This is equal to the gap within a few microns. After making the solder joint, both sides of the joint were roughly polished using 400 to 1000 grit sand papers to eliminate the possibility of any effects due to solder extruded out from the edges, followed by fine polishing of one side of the joint using 2000 grit sand paper to  $0.05\mu\text{m}$   $\text{SiO}_2$  colloidal suspension to allow observation of the microstructure evolution.

The solder joints were then tested using a thermal/mechanical analyzer made by Rheometric Scientific, Inc. The apparatus used in this study is shown in Figure 3.3. This apparatus can measure minute changes of imposed displacement and load more accurately compared to the conventional materials testing machines. Also, this apparatus has a large built-in oven, which is a forced air convection environmental chamber that can enclose the entire solder joint assembly. Hence, controlling the strain-rate and the temperature ramp time,

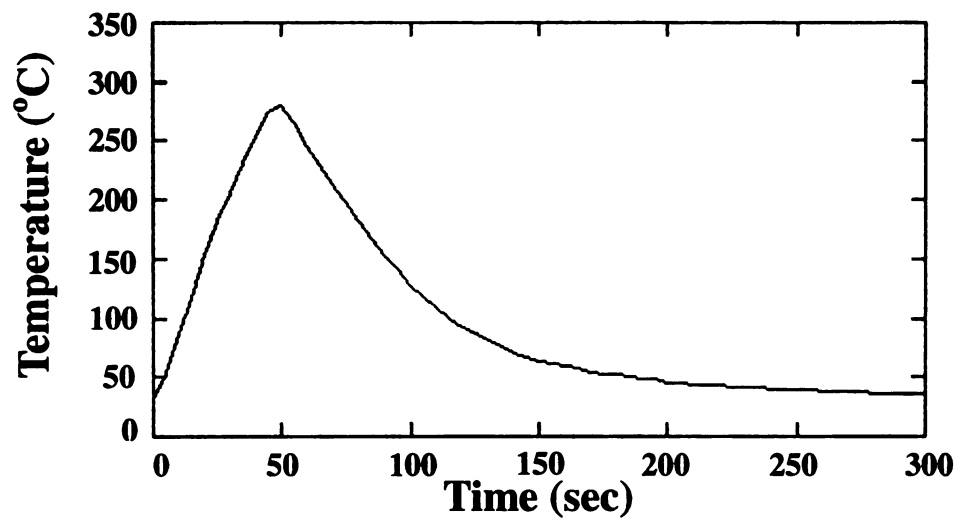


**Figure 3.2** A reflow profile for solder joint fabrication. Heating rate is  $\sim 5^{\circ}\text{C}/\text{sec}$ , peak (target) temperature is  $\sim 250^{\circ}\text{C}$ , and cooling rate is  $\sim 1^{\circ}\text{C}/\text{sec}$  in this profile.

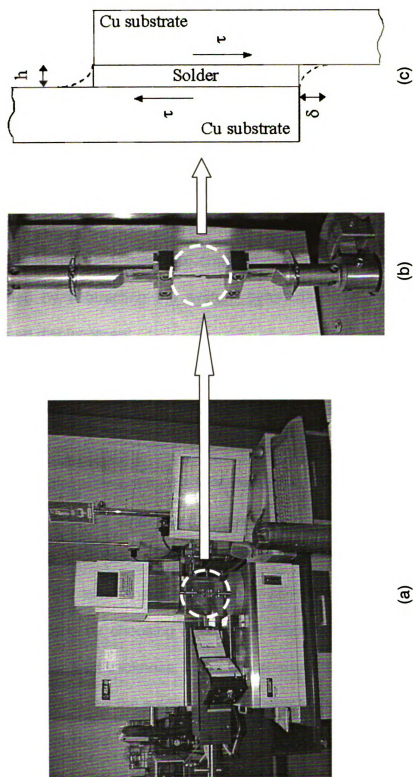


**Figure 3.3** A thermal/mechanical analyzer used in this study. (a) Entire view of the apparatus, (b) specimen installation part, and (c) a schematic of the solder joint under shear state.

and obtaining almost null temperature gradient along the specimen length, are much easier than in conventional testing machines. Although this apparatus is basically a tension/compression testing machine, because of the joint geometry the solder present in the joints experiences shear loading.

Since the RSA-III used in this study is an extremely soft machine, the shear stress versus simple shear-strain plots provided in this paper had to be corrected for machine/specimen compliances. The machine compliance value was obtained by testing a couple of specimens with known Young's modulus values. After obtaining the machine compliance value, actual displacements were obtained by subtracting the system deformation for the given load from the imposed displacement.

\_\_\_\_ The shear tests were carried out at different simple shear-strain rates of 0.001 /s, 0.01 /s, and 0.1 /s at various temperatures ranging from 25°C to 150°C. The simple shear-strain within each tested solder joint was calculated by dividing the actual displacement by the joint thickness. This parameter is too large to be termed as a 'shear strain', and 'simple shear-strain' is considered to be a more appropriate term [93]. Likewise, the term 'simple shear-strain rate' is used instead of the term 'shear strain-rate'. The simple shear-strain rates imposed were obtained by choosing appropriate displacement rates depending on the actual solder joint thickness. The actual shear stress values were obtained by dividing the load by the solder joint area after subtracting the pore area observed in fracture surfaces.

### 3.3 RESULTS AND DISCUSSION

The shear stress versus simple shear-strain plots of the eutectic Sn-Ag solder joints for the simple shear-strain rates of 0.001 /s, 0.01 /s, and 0.1 /s at various testing temperatures ranging from 25°C to 150°C are shown in Figure 3.4. The peak shear stress and the flow stress level of the eutectic Sn-Ag solder joints strongly depend on the testing temperature and simple shear-strain rate. The plots presented in Figure 3.5 provide the peak shear stress (Figure 3.5 (a)), and the simple shear-strain at peak shear stress (Figure 3.5 (b)) as a function of temperature at different simple shear-strain rates. There is significant drop in peak shear stress at lower temperatures than at higher temperatures for all levels of simple shear-strain rates. Although the peak shear stress at 125°C is about one-half of that at 25°C, no significant changes are noted between 125°C and 150°C. Simple shear-strain at the peak shear stress also decreases with increasing testing temperature at a given simple shear-strain rate. Also, one can clearly observe that the peak shear stress is strongly affected by the simple shear-strain rate especially at lower temperatures (below 125°C). However, no significant changes are found between 125°C and 150°C. The simple shear-strain at the peak shear stress decreases with decreasing simple shear-strain rate at a given testing temperature.

Figure 3.6 depicts the microstructures of the solder joint side surfaces after shear testing at a simple shear-strain rate of 0.1 /s at various testing temperatures. The deformation at lower temperatures (below 125°C) is by a shear-banding mode, whereas that at higher temperatures (above 125°C) is

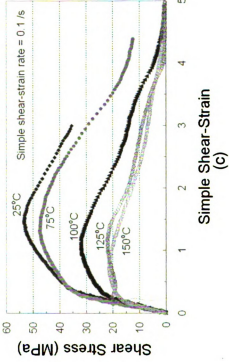
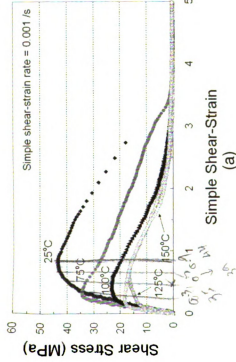
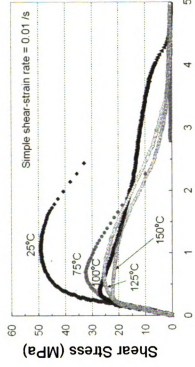


**Figure 3.4** Shear stress versus simple shear-strain plots for eutectic Sn-Ag solder joints at various simple shear-strain rates of (a) 0.001 /s, (b) 0.01 /s, and (c) 0.1 /s at different testing temperatures.

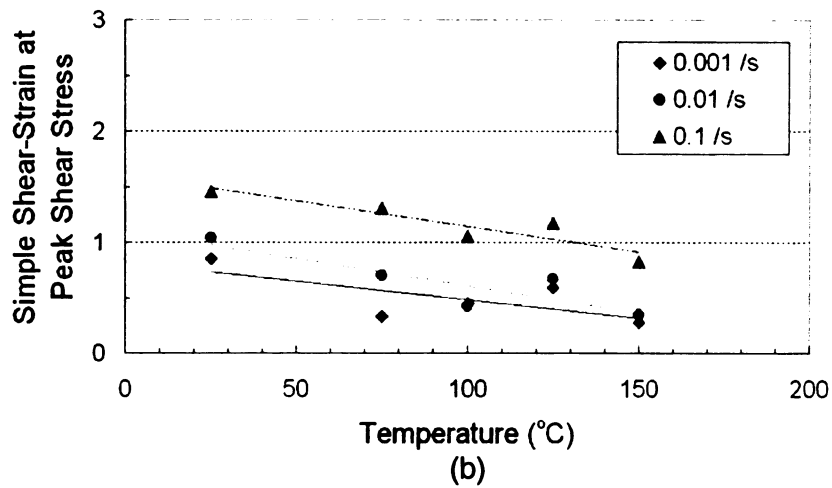
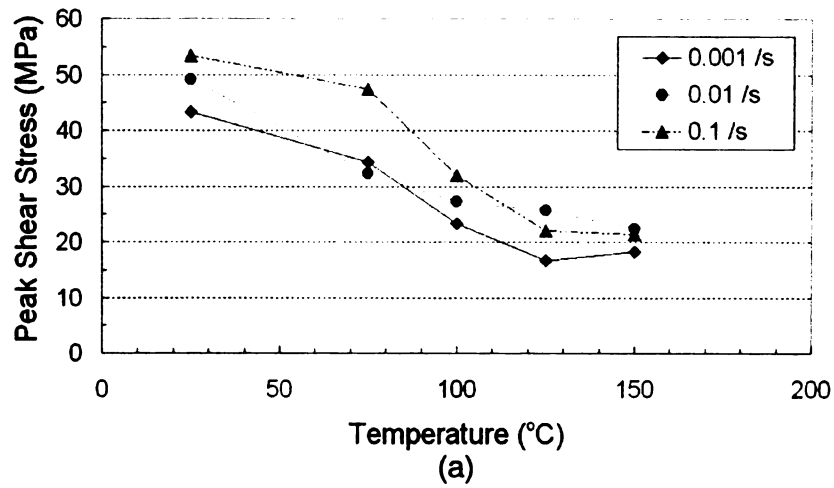


**Figure 3.5** (a) Peak shear stress and (b) simple shear-strain at peak shear stress, as a function of temperature at different simple shear-strain rates.

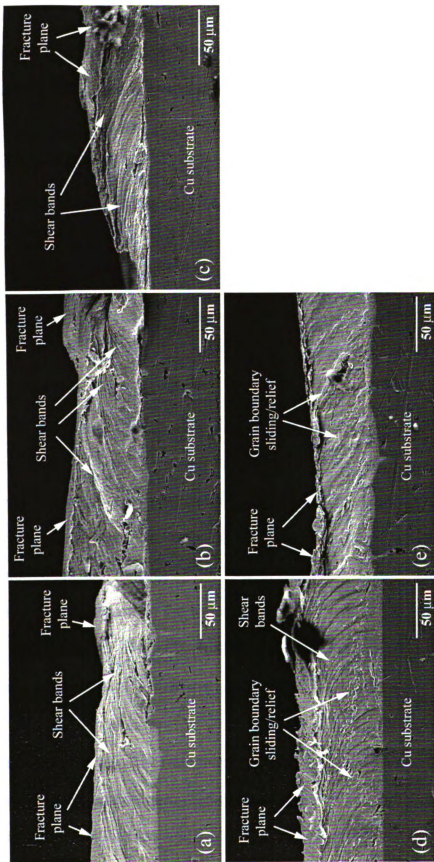


**Figure 3.6** Microstructures of the solder joint side surfaces (obtained from middle of the fine polished side of the specimen) after shear tests for specimens deformed at a simple shear-strain rate of 0.1 /s at (a) 25°C, (b) 75°C, (c) 100°C, (d) 125°C, and (e) 150°C.

dominated by grain boundary deformation. Although, the deformation features are mostly grain boundary sliding, grain boundary relief, and grain boundary decohesion for the specimens deformed at 125°C, shear bands were still seen to exist within the solder region. However, there were no shear bands visible in the specimen deformed at 150°C. It appears that in the temperature range of 125°C to 150°C a change in deformation mechanism occurs in this solder. In Figure 3.7, one can clearly observe that the specimens deformed at a higher temperature (Figure 3.7 (c) and (d)) exhibit grain boundary sliding, relief, and decohesion features unlike those deformed at a lower temperature (Figure 3.7 (a) and (b)). This was found to occur for simple shear-strain rates of both 0.001 /s, the slowest simple shear-strain rate tested, and 0.1 /s, the fastest simple shear-strain rate tested. The deformation tends to be more diffuse at a slower simple shear-strain rate and a higher temperature, whereas faster simple shear-strain rates and lower temperatures tend to cause highly localized deformation. Shear bands observed at lower temperature deformation, and grain boundary deformation exhibited at higher temperature deformation, show slightly different features with respect to the simple shear-strain rate. The specimen deformed at a 0.1 /s at lower temperature (25°C) has more concentrated shear bands than those observed in the specimen deformed at a 0.001 /s at the same temperature. At a higher temperature (150°C), the degree of grain boundary sliding, relief, and decohesion in the specimen deformed at a 0.001 /s is more severe compared to that in the specimen deformed at a 0.1 /s at the same temperature. Observed microstructural features and mechanical test results indicate that in the range of

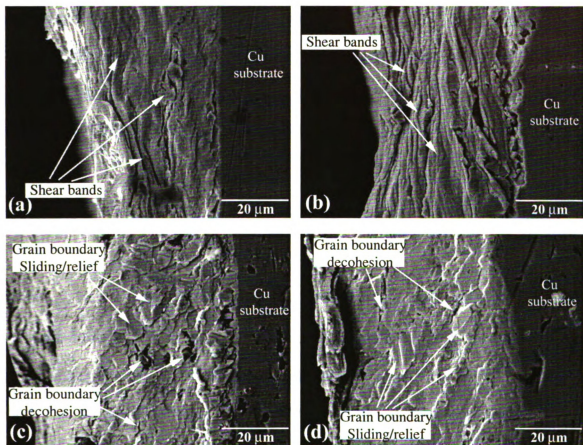


**Figure 3.7** Microstructures of the middle of the solder joint side surfaces after shear testing for specimens deformed at simple shear-strain rates of (a) 0.001 /s at 25°C, (b) 0.1 /s at 25°C, (c) 0.001 /s at 150°C, and (d) 0.1 /s at 150°C.

125°C to 150°C there is a change in the operative deformation mechanisms in the eutectic Sn-Ag solder. A similar trend has also been observed in prior studies during aging and creep of the same solder [74,89-91].

The creep parameters for the eutectic Sn-Ag solder joints can be extracted by fitting the data to power-law creep equation [94] to obtain creep properties of these solder joints from shear tests, and to compare these properties to those obtained from prior creep tests. The power-law relationship between steady-state shear-strain rate and shear stress is given as:

$$\dot{\gamma} = A \tau^n \exp\left(\frac{-Q_c}{RT}\right)$$

where, ' $\dot{\gamma}$ ' is the steady-state shear-strain rate in creep, 'A' is a material constant, ' $\tau$ ' is the shear stress, ' $n$ ' is the stress exponent, which depends on the operating creep mechanisms, ' $Q_c$ ' is the creep activation energy, 'R' is the gas constant, and 'T' is the absolute temperature. Figure 3.8 shows the relationship between simple shear-strain rate and peak shear stress at different testing temperatures, and Figure 3.9 illustrates the relationship between shear stress and the testing temperature at different simple shear-strain rates for the eutectic Sn-Ag solder joints obtained from shear tests. These results provide a range of stress exponent values of 10.0 ~ 11.7, and the creep activation energy value of ~78.4 kJ/mol, both consistent with the values obtained in prior creep studies on this solder [12,72-75,78].

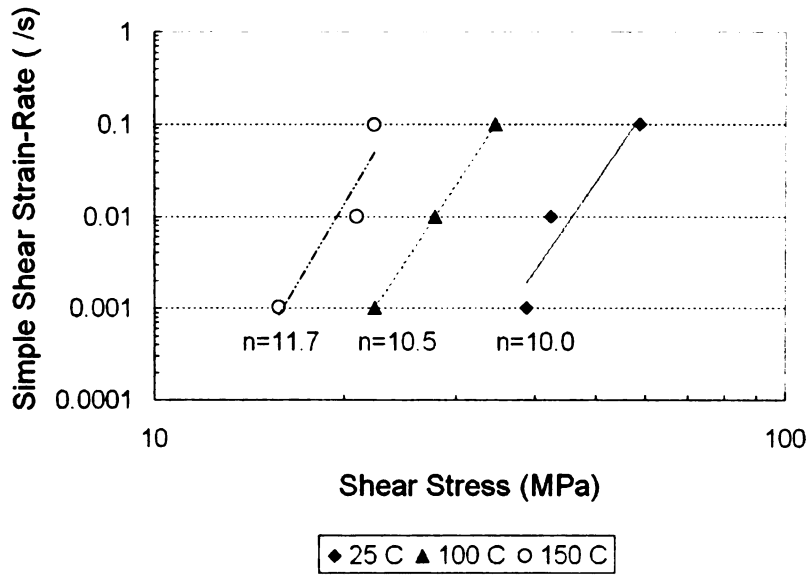


**Figure 3.8** Relationship between simple shear-strain rate and peak shear stress obtained from shear tests.

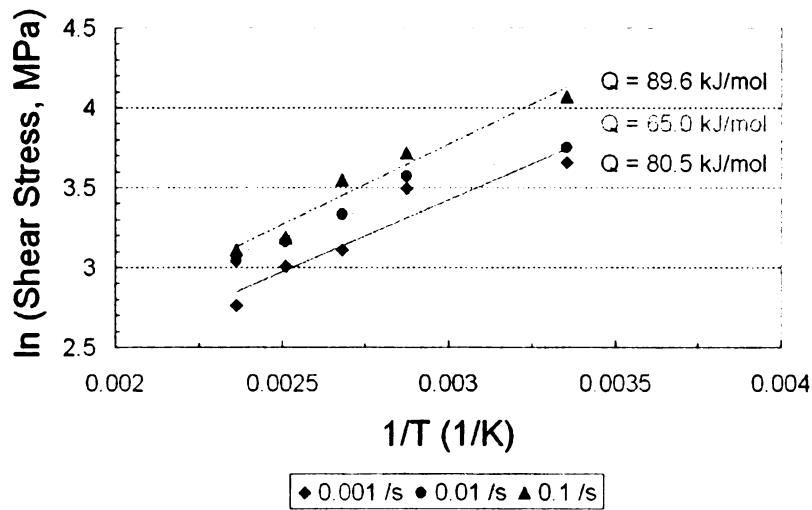


**Figure 3.9** Relationship between shear stress and testing temperature at different simple shear-strain rates obtained from shear tests.

### 3.4 SUMMARY

In this study, the fundamental mechanical behaviors, such as shear stress versus simple shear-strain curves, peak shear stress, simple shear-strain at peak shear stress, etc., of eutectic Sn-Ag solder joints were evaluated as a function of various testing temperatures and different simple shear-strain rates. Various creep parameters were also extracted from the shear test results.

Both peak shear stress and flow stress level strongly depend on testing temperature and simple shear-strain rate. The peak shear stress and the flow stress level decrease with increasing testing temperature, and with decreasing simple shear-strain rate. The effect of simple shear-strain rate on the peak shear stress is more significant at temperature regimes less than 125°C.

The deformation structure of specimens deformed at higher temperature region of 125°C to 150°C is dominated by grain boundary deformation while that at lower temperatures it is dominated by shear banding. Faster simple shear-strain rates cause concentrated deformation in localized region while slower simple shear-strain rates result in diffused deformation characteristics. Changes in the microstructural characteristics in specimens deformed at various temperatures ranging from 25°C to 150°C indicate a change in operative mechanism in low and high temperature regimes contributes to the mechanical behavior of eutectic Sn-Ag solder joints.

The power-law stress exponent and the activation energy for creep values obtained from the shear tests were consistent with previous findings from steady-state creep tests.

## CHAPTER 4

### EFFECTS OF PRE-STRAIN, RATE OF PRE-STRAIN, AND TEMPERATURE ON THE STRESS RELAXATION BEHAVIOR OF EUTECTIC Sn-3.5Ag SOLDER JOINTS

#### ABSTRACT

Stress relaxation studies on eutectic Sn-Ag solder (Sn-3.5Ag in wt%) joints were carried out at various temperatures after imposing different amounts and rates of simple shear-strain. Stress relaxation parameters were evaluated by subjecting geometrically realistic solder joints with a nominal joint thickness of  $\sim 100\mu\text{m}$  and  $1\text{mm} \times 1\text{mm}$  solder joint area. The peak shear stress during pre-loading, and residual shear stress resulting from stress relaxation were higher at the low temperature extremes than those at high temperature extremes. Also, those values increased with increasing simple shear-strain and simple shear-strain rate imposed prior to the stress relaxation events. The relaxation stress is insensitive to simple shear-strain at  $150^\circ\text{C}$  but at lower temperatures, a faster simple shear-strain rate causes higher relaxed stress value. The resulting deformation structures observed from the solder joint side surfaces were also strongly affected by these parameters. At high temperature, grain boundary sliding effects were commonly observed. At low temperature, intense shear bands dominated, and no grain boundary sliding effects were observed.

## 4.1 INTRODUCTION

The miniaturization of solder joint in electronic devices imposes several constraints on the solder interconnect affecting its integrity during service. One of the most important deformation processes that solder joints experience is thermomechanical fatigue (TMF), wherein the solder material undergoes several cycles of repeated reversed stress states as a consequence of temperature variations and stress relaxation during the dwell periods at the temperature extremes. These stresses, mainly shear, can be induced by mechanical means, but in service environments with temperature excursions it is most often due to the coefficient of thermal expansion (CTE) mismatches between solder/substrate/components. Significant damage accumulation occurs during TMF causing deterioration of residual mechanical properties [62,63,88]. TMF damage depends on temperature profile imposed during TMF. In addition to the effects of temperature extremes imposed, dwell at these temperatures, and ramp-up and ramp-down during the heating and cooling parts can play significant roles during TMF. The effect of dwell times has been characterized by observing the surface damage and residual mechanical properties of solder joint [62,63,88]. However, the effects of thermal strains resulting from CTE mismatches and temperature changes, and the rate at which this strain is imposed depending on ramp-rates have not been investigated. These rates may play significant roles in the TMF process since solder exhibits significant high strain-rate sensitivity both at low and high temperatures.

One of the prominent processes that occurs in a solder joint during service

is stress relaxation, since homologous temperature of the eutectic Sn-Ag solder is greater than  $0.5T_m$  at room temperature. Several studies on stress relaxation properties of lead-bearing as well as lead-free solders have been reported in the literature [12,24,64-66,95,96]. However, most of these investigations have been carried out on bulk tensile solder specimens without the constraint effects present in a joint configuration. Also, there is no systematic study on the effects of pre shear-loading conditions and temperature on the stress relaxation behavior of eutectic Sn-Ag solder in the joint configuration.

In order to avoid the experimental difficulties that will be encountered in evaluating the roles of these parameters during the actual TMF cycles, tests were carried out with a sensitive machine at various temperatures after imposing two different pre-strains with three different pre-strain rates. The findings of this study could provide a better understanding of the roles of thermal strain amplitudes, and ramp-rates during heating and cooling parts of TMF.

## **4.2 EXPERIMENTAL PROCEDURES**

A eutectic Sn-Ag solder paste material obtained from a commercial source was used in the present study. Single shear-lap solder joints were fabricated by soldering two dog-bone shaped copper strips together using this solder paste. The details of the specimen preparation and fabrication of single shear-lap solder joint used in this study are described in Chapter 3.2. After making the solder joint, both sides of the joint were roughly polished to eliminate the effect of solder extruded out from the edges, followed by a fine polishing of one side of the joint

to observe the deformation features in an un-etched condition. Thermal strain resulting from CTE mismatches in a given solder joint depends on the temperature change imposed, and the rate at which the temperature varies will determine the rate at which this thermal strain is imposed.

The stress relaxation experiments were carried out on a thermal/mechanical analyzer (RSA-III) made by Rheometric Scientific, Inc. at various temperatures (25°C, 85°C, and 150°C) after imposing different extents of simple shear-strain and various simple shear-strain rates prior to the stress relaxation process. The main purpose of selecting those three temperatures is that the temperature ranges that the solder joints are operated are around 80°C for typical electronic products such as computer and home appliances, and are raised up to 150°C for automotive under-the-hood applications [5,8]. The detailed performance and methods used to correct for machine compliance of this apparatus are illustrated in Chapter 3.2. The compliance due to the copper strips present in the single shear-lap joint was also corrected in the method used. The simple shear-strain values of 0.2 and 0.3, that could be calculated by dividing actual displacement of the solder by joint thickness, were selected for the pre shear-loading part of the test. The actual shear displacement of the solder was obtained by subtracting the contributions from machine compliance (including that of the copper strip) from total imposed displacement. In the pre shear-loading part of the test, 0.0001 /s, 0.001 /s, and 0.01 /s were the compliance corrected simple shear-strain rates that were employed. Detailed explanation of the nomenclature and calculation for 'simple shear-strain' and

'simple shear-strain rate' was given in Chapter 3.2. Throughout this chapter, simple shear-strain and simple shear-strain rate stand for pre-strain and rate of pre-strain imposed prior to the stress relaxation process (e.g. pre-loading part of the test), respectively. Following the pre-strain the solder joint specimens were permitted to undergo stress relaxation. The stress states that result after 300 and 1,000 seconds of relaxation were determined. After the completion of the stress relaxation test on a given specimen, deformation structures were observed from the fine-polished side of the solder joint using scanning electron microscope (SEM) without any additional surface preparation.

The specimen was then deformed to failure to obtain the solid joint area supporting the stress by subtracting pore area in fracture surfaces from the total joint area. The actual shear stress values were obtained by dividing the load by the solder joint area that supported the loading.

#### **4.3 RESULTS AND DISCUSSION**

Modeling of the TMF damage of solder joints requires an understanding of ramp-rate effects, because the residual stresses that cause creep/stress relaxation during the dwell times of TMF cycles depend on the thermal strain imposed (that depends on the temperature changes), and the rate at which this strain is imposed (that depends on the rate of temperature changes). Figure 4.1 illustrates the effect of simple shear-strain rate during pre-loading on residual shear stress resulting from stress relaxation at a constant temperature after imposing a constant simple shear-strain. Three different simple shear-strain

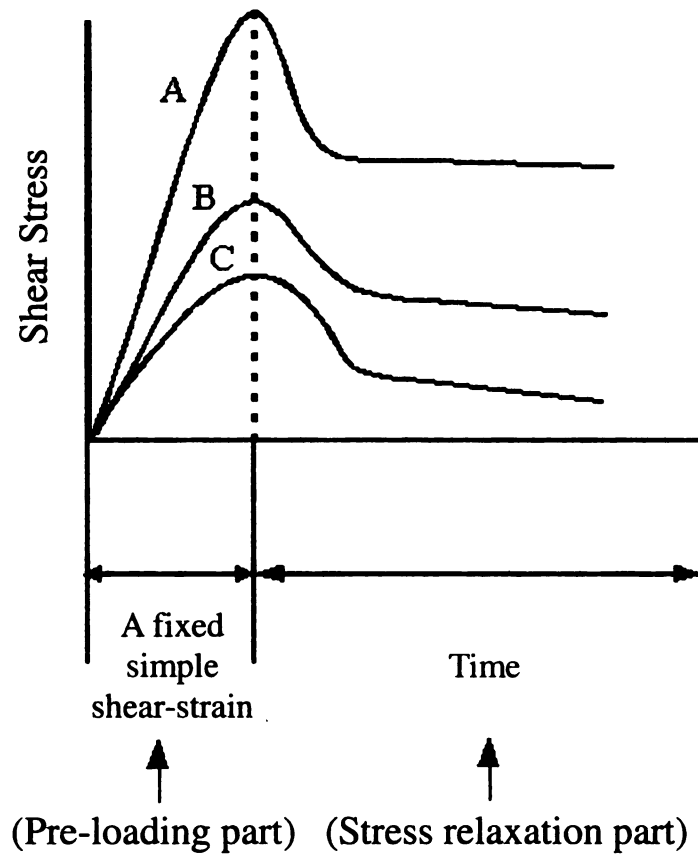


**Figure 4.1** A schematic illustration of the effect of simple shear-strain rate during pre-loading on residual shear stress resulting from stress relaxation at a constant temperature after imposing a fixed simple shear-strain. Curve A - fast simple shear-strain rate (corresponds to fast ramp-rate), curve B - medium simple shear-strain rate (corresponds to medium ramp-rate), curve C - slow simple shear-strain rate (corresponds to slow ramp-rate).

rates at a fixed simple shear-strain and temperature can be a means to understand the role of ramp-rates.

Typical shear stress versus time plots of the eutectic Sn-Ag solder joints obtained from the stress relaxation tests after imposing various simple shear-strain rates for a fixed simple shear-strain at different testing temperatures are given in Figure 4.2. The peak shear stress values at a fixed simple shear-strain imposed prior to the stress relaxation events as a function of simple shear-strain rate at various testing temperatures are provided in Table 4.1. For a given pre-strain the peak shear stress is the largest with the fastest simple shear-strain rate at any testing temperature. Also, the peak shear stress decreases with increasing testing temperature for any given simple shear-strain rate. Table 4.2 lists the measured residual shear stress values after 300 and 1,000 seconds of the stress relaxation for a fixed pre simple shear-strain of 0.3. The faster the ramp-rate (simple shear-strain rate), the greater the residual shear stress during the stress relaxation periods. Also, the residual shear stress decreases with increasing testing temperatures. The peak shear stress prior to the stress relaxation, and the residual shear stress 300 and 1,000 seconds after the stress relaxation events after imposing a pre simple shear-strain of 0.2 are shown in Tables 4.3 and 4.4, respectively. The behavior documented in these two tables is consistent with those in Tables 4.1 and 4.2. The residual shear stress during low temperature dwell is 2 to 2.5 times larger than that experienced at the higher temperature dwell. These results indicate that the residual stress after ramp-down excursion is much greater than that after ramp-up condition. In other

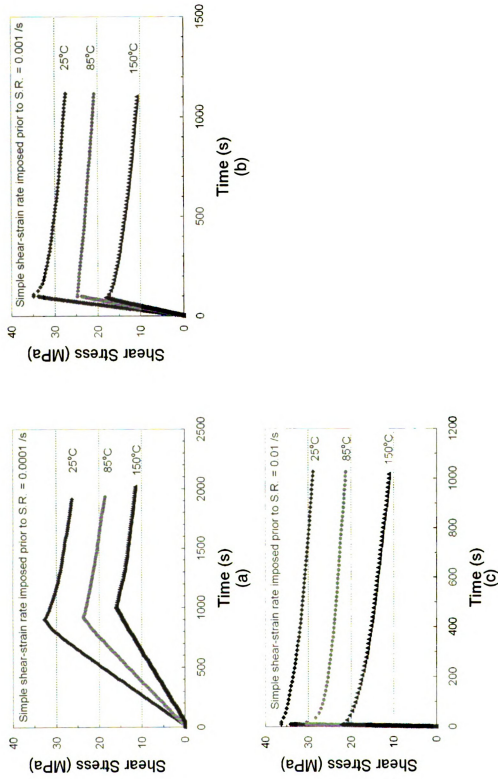


**Figure 4.2** Loading and stress relaxation curves of the eutectic Sn-Ag solder joints pre-strained prior to the stress relaxation events at simple shear-strain of 0.3 with various simple shear-strain rates of (a) 0.0001 /s, (b) 0.001 /s, and (c) 0.01 /s at various testing temperatures.

**Table 4.1** Peak shear stress values at a simple shear strain of 0.3 imposed prior to the stress relaxation events (MPa).

Temperature (°C)	Simple Shear-Strain Rate at Loading Part ( /s)		
	0.0001	0.001	0.01
25	32.8	34.9	36.3
85	23.6	24.7	30.3
150	16.0	18.1	22.3

**Table 4.2** Residual shear stress values in 300 seconds (and in 1,000 seconds) after the stress relaxation events for a fixed simple shear-strain of 0.3 (MPa).

Temperature (°C)	Simple Shear-Strain Rate at Loading Part ( /s)		
	0.0001	0.001	0.01
25	29.7 (26.3)	30.6 (27.4)	32.4 (28.8)
85	21.7 (18.5)	23.3 (20.7)	24.4 (21.1)
150	14.0 (11.5)	14.4 (10.7)	16.1 (11.1)

**Table 4.3** Peak shear stress values at a simple shear strain of 0.2 imposed prior to the stress relaxation events (MPa).

Temperature (°C)	Simple Shear-Strain Rate at Loading Part (/s)		
	0.0001	0.001	0.01
25	25.6	28.0	28.7
85	19.5	20.1	22.8
150	15.9	15.2	20.7

**Table 4.4** Residual shear stress values in 300 seconds (and in 1,000 seconds) after the stress relaxation events for a fixed simple shear-strain of 0.2 (MPa).

Temperature (°C)	Simple Shear-Strain Rate at Loading Part (/s)		
	0.0001	0.001	0.01
25	24.8 (22.2)	27.2 (24.9)	27.5 (25.4)
85	19.0 (16.7)	19.0 (16.8)	21.2 (18.7)
150	13.5 (10.3)	12.1 (9.9)	17.1 (13.8)

words, the stress level of the solder when the electronic device exists at lower temperature extremes is much higher than that when the electronic device operates at higher temperature extremes. In addition, the peak shear stress prior to the stress relaxation, and the residual shear stress resulting from the stress relaxation strongly depend on the extents of pre-strain. These values increase with increasing extent of simple shear-strain imposed at pre-loading part of the test. In actual service conditions, the magnitude of this pre-strain, in addition to CTE mismatch considerations, will be controlled by the difference between the upper and lower extreme temperatures encountered.

Figure 4.3 shows the microstructures of the side surfaces of the solder joints after the stress relaxation tests pre-strained to a simple shear-strain of 0.3 at various testing temperatures. All specimens were pre-strained at a simple shear-strain rate of 0.01 /s prior to the stress relaxation events. The deformation noted in specimens tested at 25°C and 85°C are by a shear-banding mode, while that at 150°C is dominated by grain boundary deformation. Shear banding mode represents the deformation features were dominated by shear banding with deformation progressing through the grains. Grain boundary deformation was commonly observed at high temperature, whereas intense shear bands dominated and no grain boundary deformation was observed at low temperature. One can clearly observe these deformation features upon closer examination (Figure 4.3 (d), (e), and (f)). Figure 4.4 depicts the microstructures of the side surfaces of the solder joints after stress relaxation in a specimen pre-strained to a simple shear-strain of 0.2 at various testing temperatures. Unlike

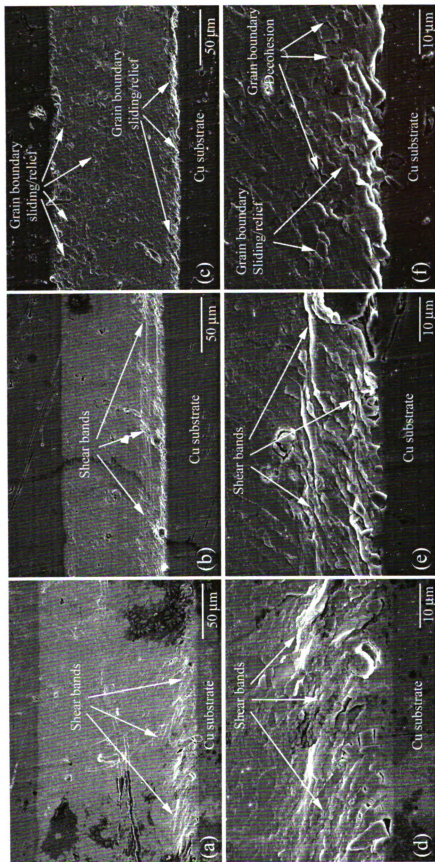


**Figure 4.3** Microstructures of the solder joint side surfaces after the stress relaxation tests. The specimens were pre-strained to a simple shear-strain of 0.3 at (a) 25°C, (b) 85°C, and (c) 150°C. (d), (e), and (f) are corresponding enlarged views of (a), (b), and (c). All specimens were pre-strained at a simple shear strain rate of 0.01 /s prior to the stress relaxation.

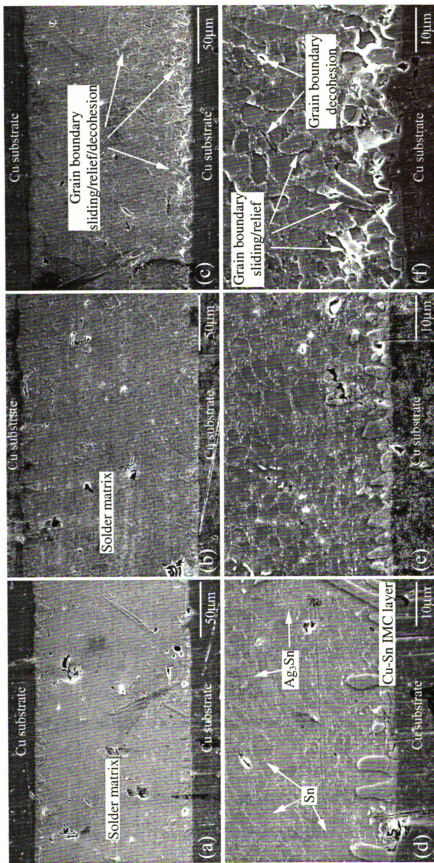


**Figure 4.4** Microstructures of the solder joint side surfaces after the stress relaxation tests. The specimens were pre-strained to a simple shear-strain of 0.2 at (a) 25°C, (b) 85°C, and (c) 150°C. (d), (e), and (f) are corresponding enlarged views of (a), (b), and (c). All specimens were pre-strained at a simple shear strain rate of 0.01 /s prior to the stress relaxation.

the specimens pre-strained to a simple shear-strain of 0.3, no significant deformation can be noted at the fine-polished side surface, at the level of magnification employed, in the specimens tested at 25°C and 85°C (Figure 4.4 (d) and (e)) since the magnitude of pre-strain is relatively small. However, grain boundary deformation features can still be observed in the specimen tested at 150°C (Figure 4.4 (f)). The effect of simple shear-strain rate on the deformation features is shown in Figure 4.5. The specimen pre-strained at a faster simple shear-strain rate (0.01 /s) at a lower temperature (25°C) has more concentrated shear bands as compared to the specimen pre-strained at a slower simple shear-strain rate (0.0001 /s) at the same temperature. At a higher temperature (150°C), the degree of grain boundary sliding, relief, and decohesion in the specimen pre-strained at a slower simple shear-strain rate (0.0001 /s) are more severe compared to that in the specimen pre-strained at a faster simple shear-strain rate (0.01 /s) at the same temperature. Similar trends in the deformation features have also been observed in prior studies during shear tests of joints made with the same solder as provided in Chapter 3 [97].

The creep parameter for the eutectic Sn-Ag solder joints during the stress relaxation period was extracted by using power-law creep equation [98] and depicted in Figure 4.6. The specimens tested at lower testing temperatures and/or faster simple shear-strain rates have the higher stress exponent ( $n$ ) values.

The schematic illustrations depicting possible scenarios for ramp-up and ramp-down situations during TMF cycle are shown in Figure 4.7. Different

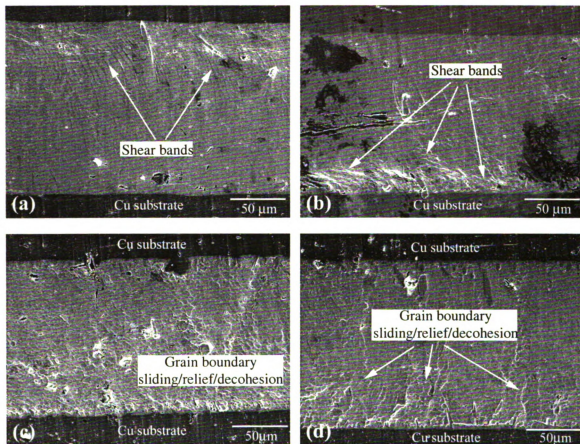


**Figure 4.5** Microstructures of the solder joint side surfaces after the stress relaxation tests. The specimens were pre-strained at simple shear-strain rates of (a) 0.0001 /s at 25°C, (b) 0.01 /s at 25°C, (c) 0.0001 /s at 150°C, and (d) 0.01 /s at 150°C. Imposed pre simple shear-strain of (a) and (b) was 0.3, and that of (c) and (d) was 0.2.

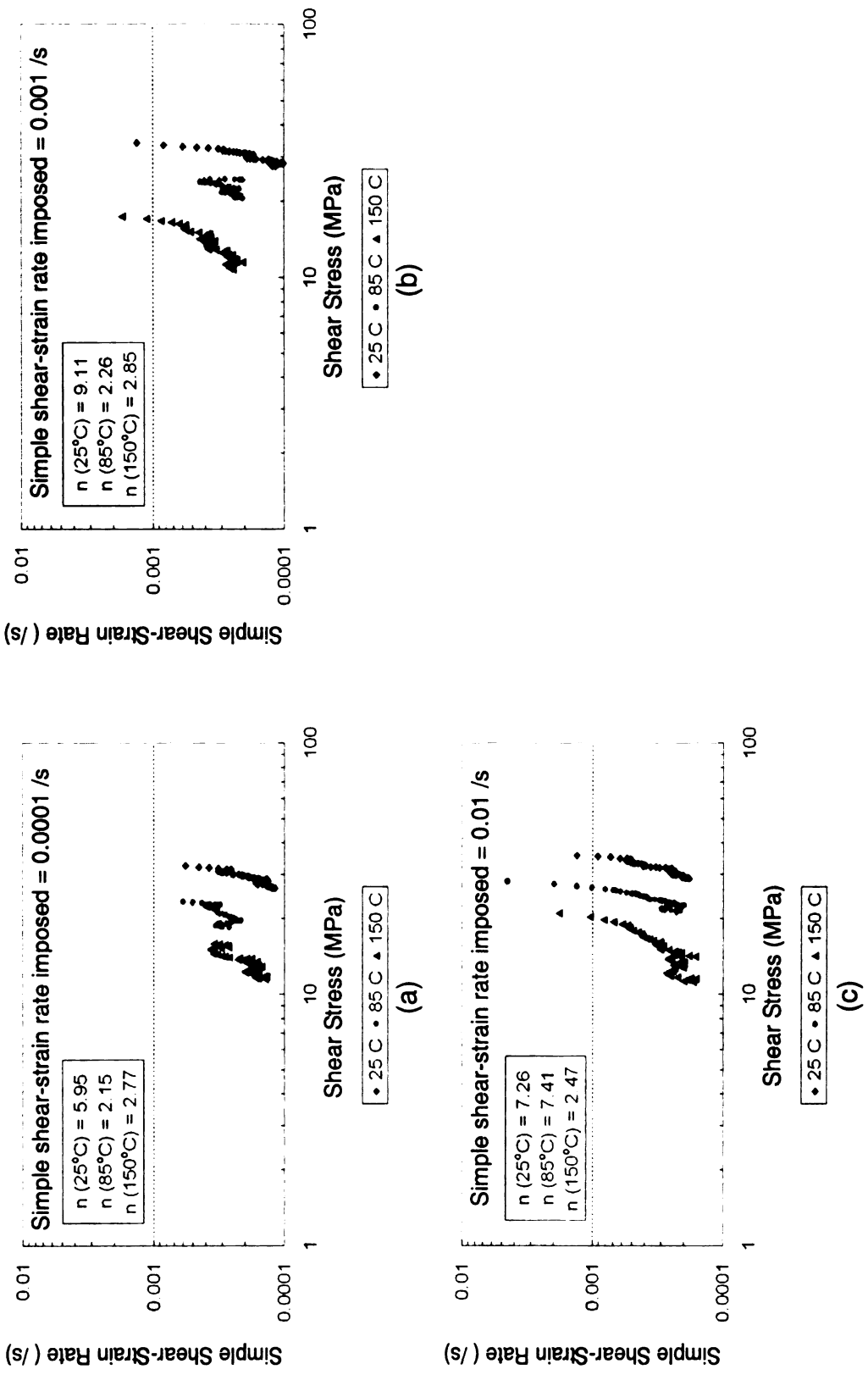


**Figure 4.6** Relationship between simple shear-strain rate and shear stress obtained from the stress relaxation part of the tests. The specimens were pre-strained to a simple shear-strain of 0.3 with various simple shear-strain rates of (a) 0.0001 /s, (b) 0.001 /s, and (c) 0.01 /s prior to the stress relaxation events.

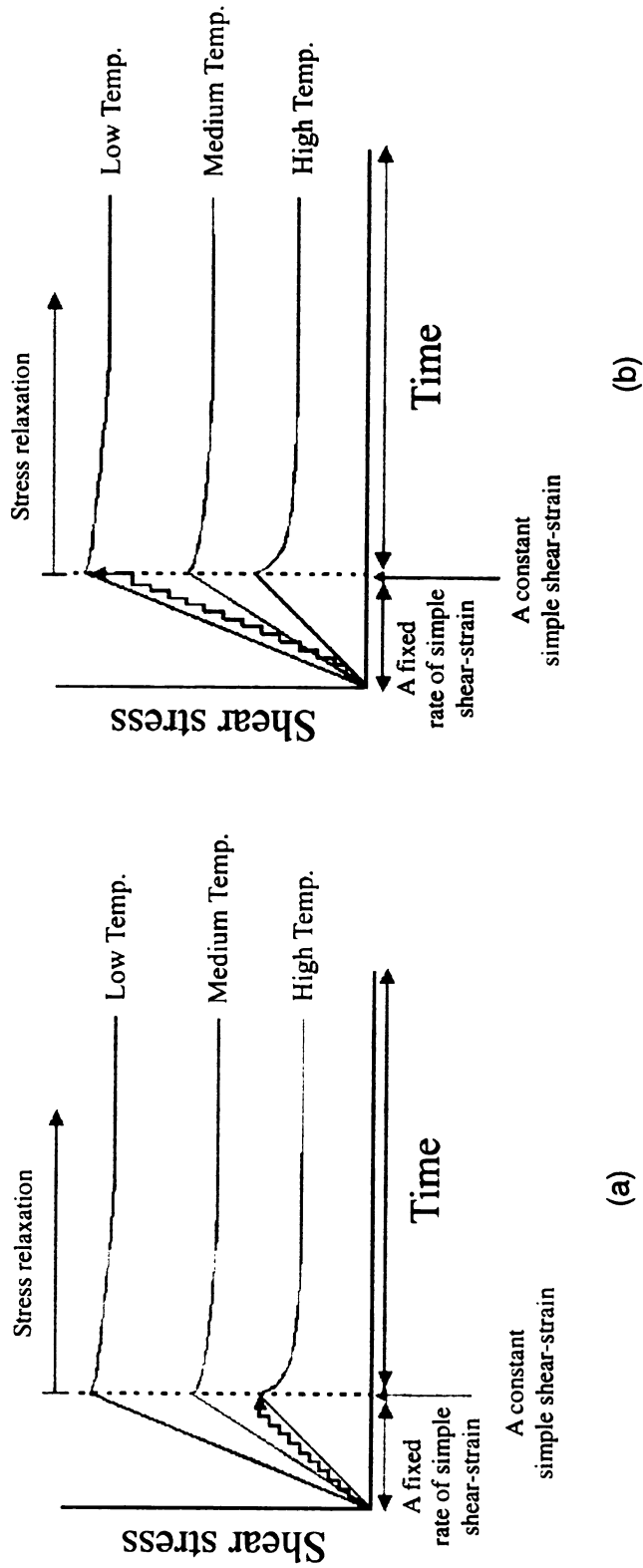


**Figure 4.7** Schematic illustration of (a) ramp-up and (b) ramp-down situations during TMF cycle.

testing temperatures at a fixed simple shear-strain and simple shear-strain rate can provide ramp-up and ramp-down situations prior to the stress relaxation process. When the electronic device is turned on or heating up, the stress level of the solder in the electronic device should firstly follow that of low temperature curve, and then gradually change to that of higher temperature curves with increasing internal temperature of the device. As a consequence, the actual stress profile of the solder should change during ramp-up excursion (Figure 4.7 (a)) resulting in lower residual shear stress. When the electronic device is turned off or cooling down, on the other hand, the stress level of the solder in the electronic device should change from high temperature curve, and gradually change to that of lower temperature curve with decreasing internal temperature of the device as shown in Figure 4.7 (b). This will result in a higher residual stress during low temperature dwell.

#### **4.4 SUMMARY AND CONCLUSIONS**

Stress relaxation tests at various pre-strain conditions and testing temperatures with various rates of pre-strain can provide information relevant to the effects of ramp-rates during heating/cooling excursions experienced during TMF.

The peak shear stress during the pre-loading part of the test strongly depends on the pre-strain, rate of pre-strain and testing temperature. The peak shear stress increases with increasing simple shear-strain and simple shear-strain rate imposed prior to the stress relaxation at a fixed testing temperature.

The peak shear stress decreases with increasing testing temperature for a given pre-strain condition. Residual shear stress resulting from the stress relaxation period decreases with increasing testing temperature at a given pre-strain. This value also increases with increasing simple shear-strain and simple shear-strain rate at a fixed testing temperature.

Grain boundary deformation is dominated in the specimen tested at 150°C while shear-banding occurs in the specimen tested at lower temperatures. The stress exponent values obtained from the stress relaxation part of the tests depend on pre-strain conditions prior to the stress relaxation and testing temperature. Faster ramp-rates will cause higher resultant residual stress as compared to slower ramp-rates.

## **CHAPTER 5**

### **ROLES OF IMPOSED PRE-STRAIN, PRE-STRAIN RATE, AND TEMPERATURE ON THE CYCLIC STRESS RELAXATION BEHAVIOR OF PRE-STRAINED EUTECTIC Sn-3.5Ag SOLDER JOINTS**

#### **ABSTRACT**

Solder joints experience repeated reverse straining during thermal excursions encountered in service, as a consequence of stresses that arise due to coefficient of thermal expansion (CTE) mismatches between entities present in the joint. They also undergo stress relaxation under fixed strain during dwell times at temperature extremes encountered during service. In order to understand the fundamental processes involved under such conditions, cyclic shear straining with associated stress relaxation at the shear strain extremes were imposed during stress relaxation of pre-strained solder joints at various temperatures. Results of such studies were compared with previously reported findings from monotonic shear stressing and stress relaxation tests. Residual stress during stress relaxation under repeated reverse straining exhibited significant decrease for specimens deformed to a higher pre-strain at a higher pre-strain rate, at lower temperature. Stress relaxation during subsequent cycles of straining was found to be strongly dependant on the test temperature and the imposed pre-strain amplitude and pre-strain rate.

## 5.1 INTRODUCTION

Thermomechanical fatigue (TMF) behavior of solder joints during service is a critical concern in electronic packaging. Solder joints used in harsh operational environments, such as automotive under-the-hood, aerospace, defense, and densely packed microelectronics, experience severe TMF as a consequence of stresses arising not only due to mechanical means but also due to CTE mismatches between the solder and components under thermal fluctuations [5,13,17,23]. Failure under such conditions is mainly caused by the repeated straining resulting from the thermal fluctuations.

Solder joints undergo several cycles of repeated reverse stress states as a consequence of temperature variations and stress relaxation during the dwell periods at the temperature extremes. These repeated reverse stress states occur during heating and cooling periods of the thermal cycles in service. During dwell times at the temperature extremes of the thermal cycle, the stresses that develop due to CTE mismatches tend to relax. Residual stresses resulting from stress relaxation are affected by the thermal strain imposed, the rates at which this strain is imposed, and temperature [99].

Several studies on either repeated straining or stress relaxation properties of lead-bearing as well as lead-free solders have been reported in the literature [12,24,49,51,56,64-66,100,101]. However, most of these investigations have been carried out with bulk solder specimens without the constraint effects present in a joint configuration. Recent publications on the repeated reverse straining and stress relaxation properties of lead-free solder using joint configuration have

been carried out at room temperature [68,69,102]. However, these investigations used a solder joint thickness of about 700 $\mu\text{m}$ , while a typical joint thickness in electronic applications will be about 100~200 $\mu\text{m}$ .

The objective of the present study is to evaluate the behavior of eutectic Sn-Ag solder joints with about 100 $\mu\text{m}$  joint thickness, representative of those used in microelectronics, under repeated reverse shear straining with associated stress relaxation at the shear strain extremes at various temperatures. Comparisons between the findings from present study, and previously reported monotonic shear straining and stress relaxation tests [99] could identify the differences in the solder joint behavior under monotonic and repeated straining. Also, the present study may aid in life prediction of solder joints undergoing TMF, since the process and service related parameters in the present study could shed some light on the operative processes under such conditions.

## **5.2 EXPERIMENTAL PROCEDURES**

This study deals with the role of imposed cyclic straining on the stress relaxation behavior of eutectic Sn-Ag solder joints. In order to simplify the presentation of relevant experimental details, following abbreviations are used in this chapter. The terms ' $\gamma_p$ ' and ' $\gamma_c$ ' are used to represent 'pre simple shear-strain amplitude' and 'cyclic simple shear-strain amplitude' respectively. The simple shear-strain within each tested solder joint was calculated by dividing the actual displacement imposed on the solder by the joint thickness. This parameter is too large to be termed as a 'shear strain', and 'simple shear-strain'

is considered to be a more appropriate term. Likewise, the term 'simple shear-strain rate' is more appropriate instead of the term 'shear strain-rate' [97]. ' $\dot{\gamma}_p$ ' and ' $\dot{\gamma}_c$ ' are used for 'pre simple shear-strain rate' and 'cyclic simple shear-strain rate'. 'SRC' and 'SR' are used to represent stress relaxation with and without imposed cyclic strains respectively.

Single shear-lap solder joints were fabricated with a eutectic Sn-Ag solder paste material obtained from a commercial source by soldering two dog-bone shaped copper substrates together. The details of the specimen preparation and fabrication of single shear-lap solder joint used in this study are provided in Chapter 3.2. All mechanical tests were carried out with a thermomechanical analyzer at 25°C, 85°C, and 150°C. Although the specimens were primarily loaded in tension mode using this apparatus, the solder joints underwent simple shear states because of the joint geometry. The detailed performance and advantages, and methods used to correct for machine compliance are given in Chapter 3.2.  $\gamma_p$ ,  $\dot{\gamma}_p$ ,  $\gamma_c$ ,  $\dot{\gamma}_c$ , and testing temperatures used in the present investigation are listed in Table 5.1. During the cyclic straining part of the tests, the specimens were permitted to undergo stress relaxation, at the strain extremes, for a period of 300 seconds. This cycling was repeated for 10 times.

A schematic of such repeated reverse cycling is depicted in Figure 5.1. The different  $\gamma_p$  values of 0.2 and 0.3 were selected for the pre-straining segment of the test to facilitate comparison with previously reported findings from SR tests [99]. These pre-strains prevented the stress state from becoming

**Table 5.1.** Testing parameters for SRC experiments.  $\gamma_c$  imposed was 0.05, and hold times at maximum and minimum shear-strain extremes for stress relaxation experiments were 300 seconds.

Pre simple shear-strain, $\gamma_p$	Pre simple shear-strain rate, $\dot{\gamma}_p$ (/s)	Cyclic simple shear-strain rate, $\dot{\gamma}_c$ (/s)
0.2	0.0001	0.00005
		0.0005
		0.005
	0.001	0.00005
		0.0005
		0.005
	0.01	0.00005
		0.0005
		0.005
0.3	0.0001	0.00005
		0.0005
		0.005
	0.001	0.00005
		0.0005
		0.005
	0.01	0.00005
		0.0005
		0.005

**Note:** Experiment under each test condition was carried out at three different testing temperatures of 25°C, 85°C, and 150°C.

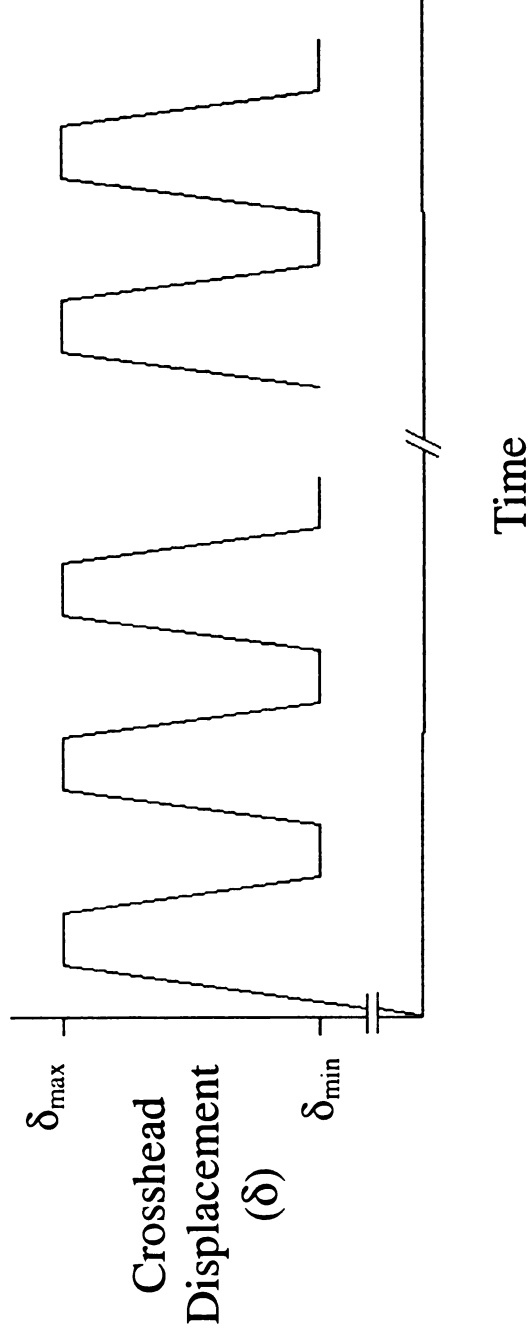


**Figure 5.1** A schematic of the SRC cycling. The  $\gamma_{\max}$  and  $\gamma_{\min}$  were obtained by dividing  $\delta_{\max}$  and  $\delta_{\min}$  by joint thickness.  $\gamma_c$  ( $\gamma_{\max} \sim \gamma_{\min}$ ) employed in this study was 0.05 and the cycling was repeated 10 times.

negative during SRC allowing the specimens to be held in the tensile mode during cycling without buckling. After the completion of the SRC test on a given specimen, deformation structures were observed from the fine-polished side of the solder joint using SEM. The specimen was then deformed to failure to obtain the solid joint area supporting the stress by subtracting pore area in fracture surfaces from the total joint area. The actual shear stress values were obtained by dividing the load by the solder joint area that supported the loading.

## 5.3 RESULTS AND DISCUSSION

### 5.3.1 Effects of Pre-Strain

Experimental results obtained from fixed  $\dot{\gamma}_p$ ,  $\gamma_c$ ,  $\dot{\gamma}_c$ , and testing temperature conditions were used to identify the role of  $\gamma_p$ . Shear stress versus time plot obtained from the SRC experiments under such condition is shown in Figure 5.2 (a). In order to minimize the number of figures, the general trends observed are provided for a chosen test condition. For example, test results obtained from different temperatures are used to illustrate the general trends regarding the effects of  $\gamma_p$ ,  $\dot{\gamma}_p$ ,  $\dot{\gamma}_c$ , etc. in these sketches. The peak shear stress obtained during loading part of the test, and residual shear stress during stress relaxation period are strongly affected by the amount of  $\gamma_p$  imposed. One can clearly observe this effect in Figure 5.2 (b) showing the maximum shear stress obtained in each cycle as a function of number of cycles. In this figure, only positive shear stress region is presented to illustrate the important features.

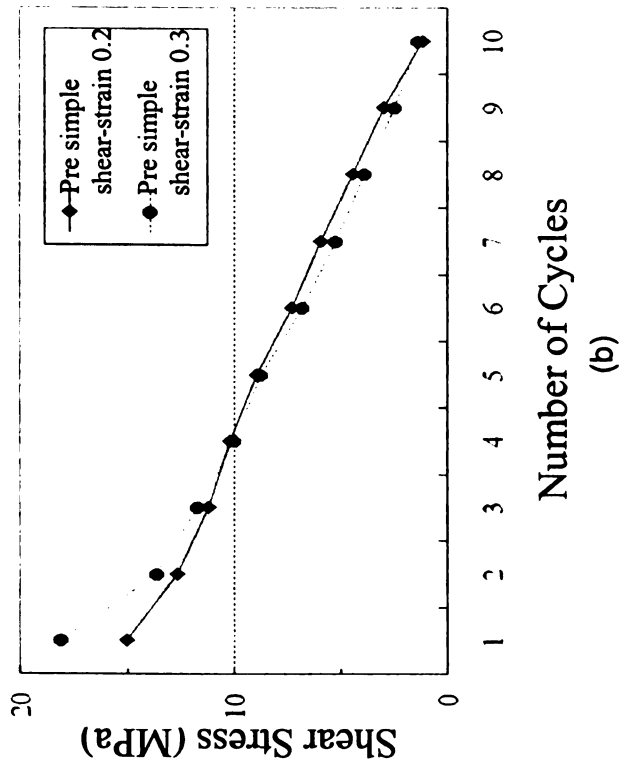
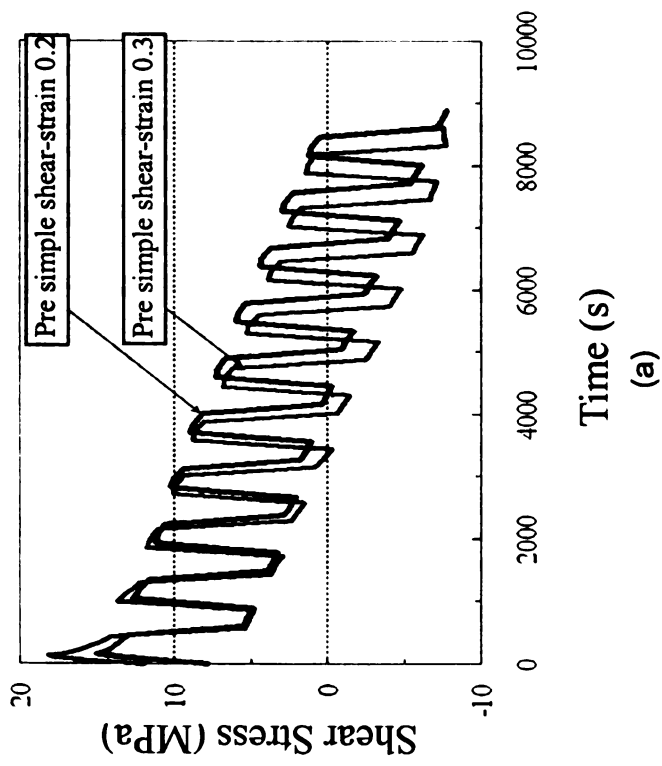


**Figure 5.2** Effects of pre-strain on the solder joint behavior under SRC conditions. (a) SRC curves of the eutectic Sn-Ag solder joints, and (b) relationship between the maximum shear stress obtained during each cycle and number of cycles.

**Note:** Other test parameters are fixed at  $\dot{\gamma}_p$  of 0.001 /s, testing temperature of 150°C,  $\gamma_c$  of 0.05, and  $\dot{\gamma}_c$  of 0.0005 /s.

For a given  $\dot{\gamma}_p$  followed by imposing a fixed  $\gamma_c$  and  $\dot{\gamma}_c$  at isothermal testing temperature, the maximum shear stress experienced at first cycle is larger for a higher imposed  $\gamma_p$ . Although the maximum shear stress experienced at the first cycle of the tests is higher in the specimens pre-strained to a larger  $\gamma_p$ , the maximum shear stresses obtained after few cycles are lower than those in the specimens pre-strained to a smaller  $\gamma_p$  since the initial shear stress drop during stress relaxation is much larger in the specimen that experienced higher imposed  $\gamma_p$ . This implies that the curvature of the plot illustrating the maximum shear stress change with respect to the number of cycles depends strongly on the initial drop of maximum shear stress.

### 5.3.2 Effects of Pre-Strain Rate

To assess the effects of  $\dot{\gamma}_p$ , results obtained from fixed  $\gamma_p$ ,  $\gamma_c$ ,  $\dot{\gamma}_c$ , and testing temperature conditions were used in this analysis. As shown in Figure 5.3 (a), the peak shear stress realized prior to the stress relaxation process in each cycle, and residual shear stress during stress relaxation period after 300 seconds, are strongly affected by  $\dot{\gamma}_p$  imposed. The change in maximum shear stress obtained from each cycle of the stress relaxation as a function of number of cycles is shown in Figure 5.3 (b). Imposition of faster  $\dot{\gamma}_p$  resulted in higher maximum shear stress at first cycle of the tests, and larger stress drop during subsequent cycles for a given test condition. As a consequence, the maximum

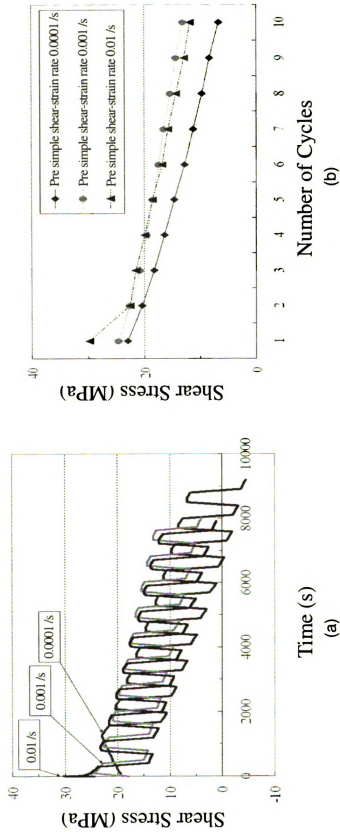


**Figure 5.3** Effects of pre-strain rate on the solder joint behavior under SRC conditions. (a) SRC curves of the eutectic Sn-Ag solder joints, and (b) relationship between the maximum shear stress obtained during each cycle and number of cycles.

**Note:** Other test parameters are fixed at  $\gamma_p$  of 0.3, testing temperature of 85°C,  $\gamma_c$  of 0.05, and  $\dot{\gamma}_c$  of 0.0005 /s.

shear stress obtained after few cycles is sometimes lower than that in the specimens tested at slower  $\dot{\gamma}_p$ 's, although the maximum shear stress experienced at the first cycle of the tests is higher in the specimens tested with faster  $\dot{\gamma}_p$ 's.

### 5.3.3 Effects of Testing Temperature

Test results obtained from fixed  $\gamma_p$ ,  $\dot{\gamma}_p$ ,  $\gamma_c$ ,  $\dot{\gamma}_c$  conditions were selected to evaluate the role of testing temperature in this series of tests. In Figure 5.4 (a), the shear stress versus time plot obtained from the SRC experiments under such condition is shown. The peak shear stress experienced during loading part of each cycle, and residual shear stress during stress relaxation period are strongly affected by testing temperature. For a given pre-strain condition (a fixed  $\gamma_p$  and  $\dot{\gamma}_p$  imposed prior to the first cycle) followed by imposing a fixed  $\gamma_c$  and  $\dot{\gamma}_c$ , the maximum shear stress obtained from each cycle of the tests, and residual stress during stress relaxation period decrease with increasing testing temperature. Maximum shear stress experienced in each cycle as a function of number of cycles is plotted in Figure 5.4 (b). The lower testing temperature resulted in higher maximum shear stress at each cycle for a given test condition. Also, the initial shear stress drop and the percent drop in shear stress with number of cycles are larger at higher testing temperature. The stress drop at early stage of SRC condition is very sensitive to testing temperature.

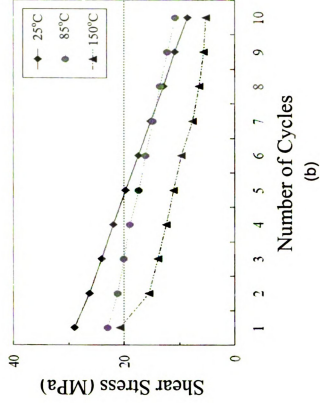
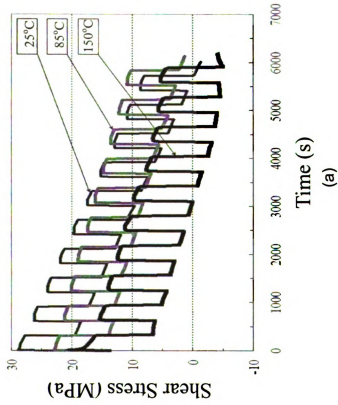


**Figure 5.4** Effects of testing temperature on the solder joint behavior under SRC conditions. (a) SRC curves of the eutectic Sn-Ag solder joints at various testing temperatures, and (b) relationship between the maximum shear stress obtained during each cycle and number of cycles.

**Note:** Other test parameters are fixed at  $\dot{\gamma}_p$  of 0.2,  $\dot{\gamma}_c$  of 0.01 /s,  $\gamma_c$  of 0.05, and  $\dot{\gamma}_c$  of 0.005 /s.

### 5.3.4 Microstructural Characterization

Figure 5.5 shows the microstructures of the side surfaces of the solder joints after the SRC tests. These specimens were subjected to a  $\gamma_p$  of 0.2 with different  $\dot{\gamma}_p$ 's followed by a fixed  $\gamma_c$  and  $\dot{\gamma}_c$  at various testing temperatures. No significant deformation can be noted at the fine-polished side surface of the specimen pre-strained to a  $\gamma_p$  of 0.2 at the level of magnification employed in the specimens tested at 25°C and 85°C (Figure 5.5 (a) and (d), (b) and (e)), since the magnitude of pre-strain is relatively small. However, grain boundary deformation features can be observed in the specimens tested at 150°C (Figure 5.5 (c) and (f)). The microstructures of the side surfaces of the solder joints after the SRC tests in the specimen pre-strained to a  $\gamma_p$  of 0.3 with different  $\dot{\gamma}_p$ 's are provided in Figure 5.6. Unlike that in the specimens pre-strained to a  $\gamma_p$  of 0.2, the deformation feature by a shear-banding mode can be observed in the specimens tested at 25°C. The specimen pre-strained at a faster  $\dot{\gamma}_p$  at 25°C (Figure 5.6 (d)) has more concentrated shear bands as compared to the specimen pre-strained at a slower  $\dot{\gamma}_p$  at the same temperature (Figure 5.6 (a)). Deformation features in the specimen deformed at a higher temperature (150°C) are mostly grain boundary deformations, whereas a combination of shear banding and grain boundary deformation is present in the specimens tested at an intermediate temperature (85°C). The grain boundary deformations and shear bands are aligned with respect to the shear direction at this temperature.

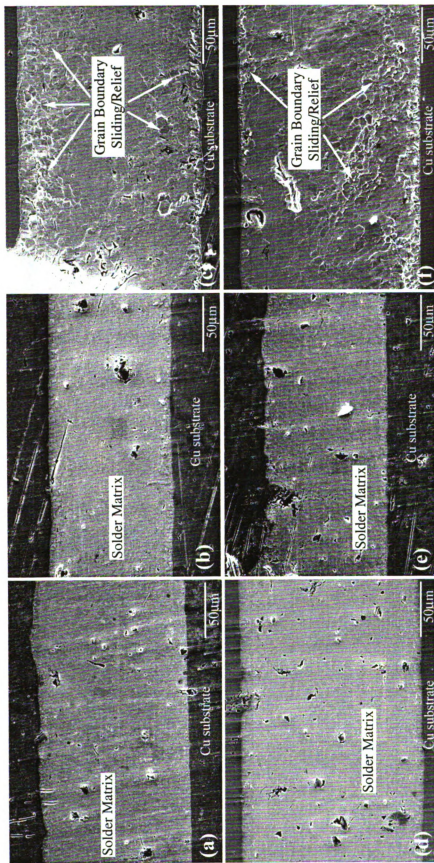


**Figure 5.5** Microstructures of the solder joint side surfaces after the SRC tests. All specimens were pre-strained to a  $\gamma_p$  of 0.2 prior to the first cycle, followed by imposing a fixed  $\gamma_c$  and  $\dot{\gamma}_c$ . The specimens were pre-strained at  $\dot{\gamma}_p$ 's of (a) 0.0001 /s at 25°C, (b) 0.0001 /s at 85°C, (c) 0.0001 /s at 150°C, (d) 0.01 /s at 25°C, (e) 0.01 /s at 85°C, and (f) 0.01 /s at 150°C.

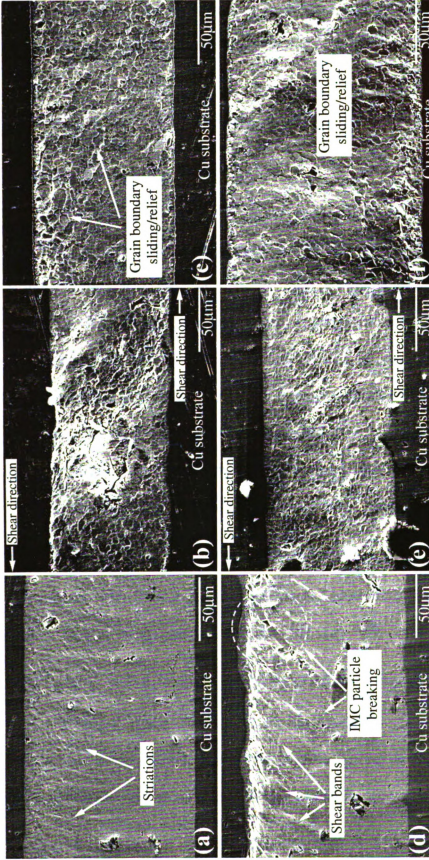


**Figure 5.6** Microstructures of the solder joint side surfaces after the SRC tests. All specimens were pre-strained to a  $\dot{\gamma}_p$  of 0.3 prior to the first cycle, followed by imposing a fixed  $\dot{\gamma}_c$  and  $\dot{\gamma}_c$ . The specimens were pre-strained at  $\dot{\gamma}_p$ 's of (a) 0.0001 /s at 25°C, (b) 0.0001 /s at 85°C, (c) 0.0001 /s at 150°C, (d) 0.01 /s at 25°C, (e) 0.01 /s at 85°C, and (f) 0.01 /s at 150°C.

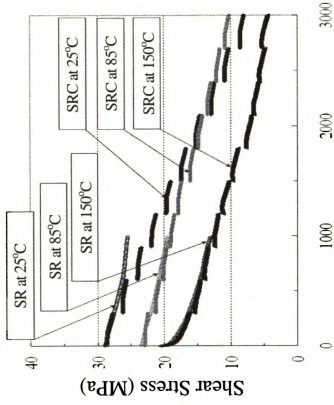
Similar trends in the deformation features have also been observed in the previously reported monotonic shear test results [97], and SR test results [99].

### **5.3.5 Comparisons of the Solder Joint Behavior between SR and SRC Conditions**

#### **5.3.5.1 Solder Joint Behavior**

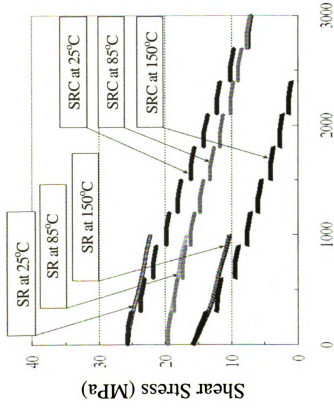
The comparison of shear stress versus time plots obtained from stress relaxation part of the test between SR and SRC conditions is shown in Figure 5.7. Stress decreases more rapidly under SRC condition as compared to SR tests especially at lower temperature, since repeated reverse stresses may facilitate easy accommodation of microstructural damage as depicted in Figure 5.8. At a lower temperature, some striations can be found after SR test (Figure 5.8 (a)), whereas more concentrated shear bands can be found after SRC test, especially in solder region near the intermetallic compound (IMC) layer (Figure 5.8 (b)).

The difference in the extent of stress drop during stress relaxation under SR and SRC conditions depends on the imposed  $\dot{\gamma}_p$ . At a slower  $\dot{\gamma}_p$  imposed, stress state after SRC condition decreases faster than that after SR tests in all testing temperature ranges (Figure 5.7 (a) and (c)). At higher testing temperatures with a faster  $\dot{\gamma}_p$ , however, stress states after SRC condition are comparable to that after SR tests since the maximum shear stress realized at the subsequent cycle reaches shear stress experienced at the end of the previous cycle at high temperature under SRC conditions, probably due to crack healing (Figure 5.7 (b) and (d)). This implies that both  $\dot{\gamma}_p$  imposed and testing



Time (stress relaxation portion only, s)

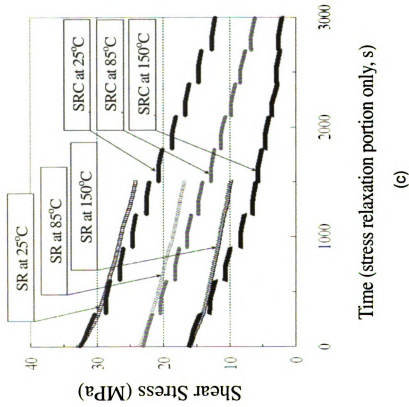
(a)



Time (stress relaxation portion only, s)

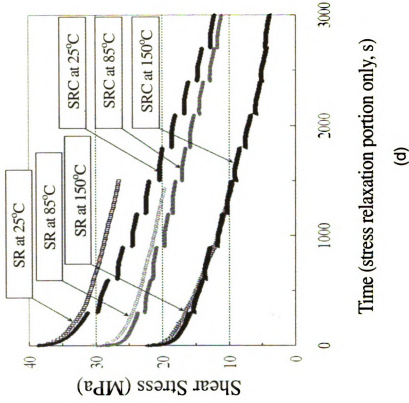
(b)

**Figure 5.7** Comparison of shear stress versus time plots obtained from stress relaxation part of the test between SR and SRC tests. The specimens were pre-strained to (a)  $\dot{\gamma}_p$  of 0.2 at  $\dot{\gamma}_p$  of 0.0001 /s, (b)  $\dot{\gamma}_p$  of 0.2 at  $\dot{\gamma}_p$  of 0.01 /s, (c)  $\dot{\gamma}_p$  of 0.3 at  $\dot{\gamma}_p$  of 0.0001 /s, and (d)  $\dot{\gamma}_p$  of 0.3 at  $\dot{\gamma}_p$  of 0.01 /s. **(cont'd)**  
**Note:** Other test parameters are fixed at  $\dot{\gamma}_c$  of 0.05 and  $\dot{\gamma}_c$  of 0.0005 /s.



Time (stress relaxation portion only, s)

(c)



Time (stress relaxation portion only, s)

(d)

Figure 5.7 (cont'd)

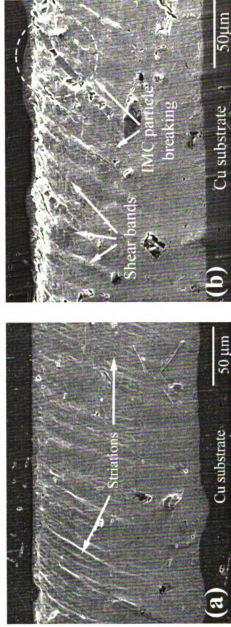


**Figure 5.8** Comparison between microstructures of the solder joint side surfaces after (a) SR and (b) SRC tests at 25°C.

**Note:** Other test conditions are fixed at  $\dot{\gamma}_p$  of 0.3,  $\dot{\gamma}_c$  of 0.01 /s,  $\dot{\gamma}_c$  of 0.05, and  $\dot{\gamma}_c$  of 0.005 /s.

temperature can play significant roles for solder joint behavior under repeated reverse stressing.

### 5.3.5.2 Creep Properties

The creep parameters for the eutectic Sn-Ag solder joints under SRC conditions can be extracted by fitting the data to a power-law creep equation since homologous temperatures of such solder joints are greater than  $0.5T_m$  even at room temperature;

$$\dot{\gamma} = A \tau^n \exp\left(-\frac{Q}{RT}\right)$$

where, ' $\dot{\gamma}$ ' is the steady-state shear-strain rate in creep, 'A' is the material constant, ' $\tau$ ' is the shear stress, ' $n$ ' is the stress exponent, 'Q' is the creep activation energy, 'R' is the gas constant, and 'T' is the absolute temperature. Figure 5.9 shows the relationship between simple shear-strain rate and shear stress obtained from the stress relaxation part of the SRC tests along with that obtained from SR tests (open symbols) [99], and repeated reverse stressing with a large solder joint geometry (asterisk symbols) [68]. The stress exponents, which depend on the operating creep mechanisms, under such SRC condition range from 9.4 to 9.7, and are comparable to the stress exponents reported in the literature [74]. Although the stress exponents obtained are very similar, the simple shear-strain rates vary with respect to the test conditions. For the same stress level, simple shear-strain rates under SRC condition are much larger than those under SR condition at low temperature. However, values for both

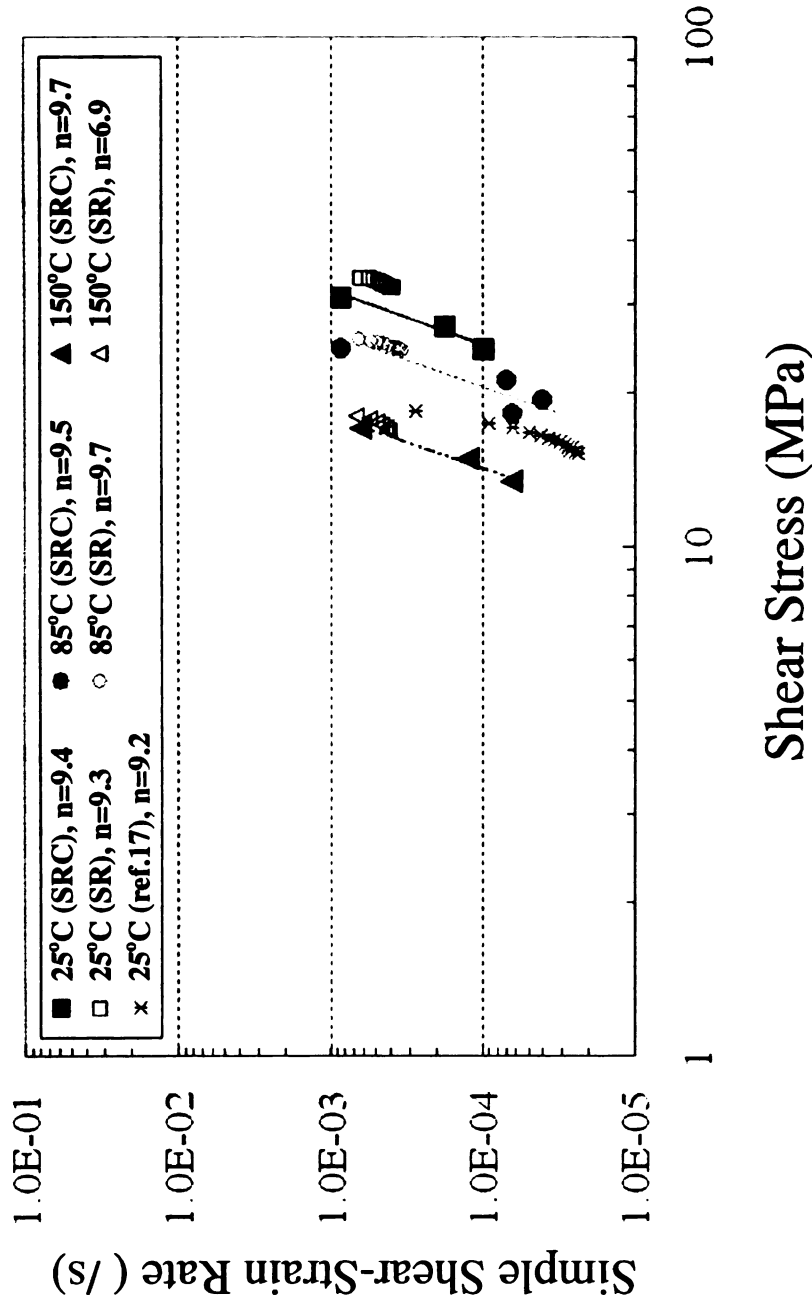


**Figure 5.9** Relationship between simple shear-strain rate and peak shear stress in each cycle obtained from the stress relaxation part of the test. The specimens were pre-strained to a  $\gamma_p$  of 0.3 at a  $\dot{\gamma}_p$  of 0.01 /s, followed by imposing a fixed  $\dot{\gamma}_c$  (0.05) and  $\dot{\gamma}_c$  (0.005 /s).

**Note:** Closed symbols represent data obtained from current study.  
 Rest from previously published data [68,99].

conditions are much closer at higher temperatures. This can be attributed to the continuing damage accumulation at lower temperature under such test condition as depicted in Figure 5.7 (d).

Figure 5.10 displays the relationship between peak shear stress in each cycle and testing temperature under SRC tests using data from Figure 5.9. The creep activation energy values obtained from stress relaxation during each cycle range from 39 to 70 kJ/mol, and are consistent with the values obtained in prior creep studies on joints made with this solder [74].

### 5.3.5.3 General Trend

Figure 5.11 shows an overall schematic comparison of effects of various testing parameters on eutectic Sn-Ag solder joints behavior under SR and SRC conditions. Imposing smaller  $\gamma_p$ , slower  $\dot{\gamma}_p$ , and/or higher testing temperature resulted in lower residual shear stress, and comparable stress level during stress relaxation period between SR and SRC conditions, since such test conditions may allow the joint to adapt to imposed stress easier than in case of with larger  $\gamma_p$ , faster  $\dot{\gamma}_p$ , and/or lower testing temperature. The results obtained from such test conditions could provide a better understanding of the roles of process and service related parameters on the solder joints behavior under actual TMF condition. A simple parametric approach to model the life time prediction on Sn-based solder joints has been suggested [103]. The findings from present study should also serve to provide the various parametric functions for such an approach contributing to reliability prediction of the lead-free solder joints.

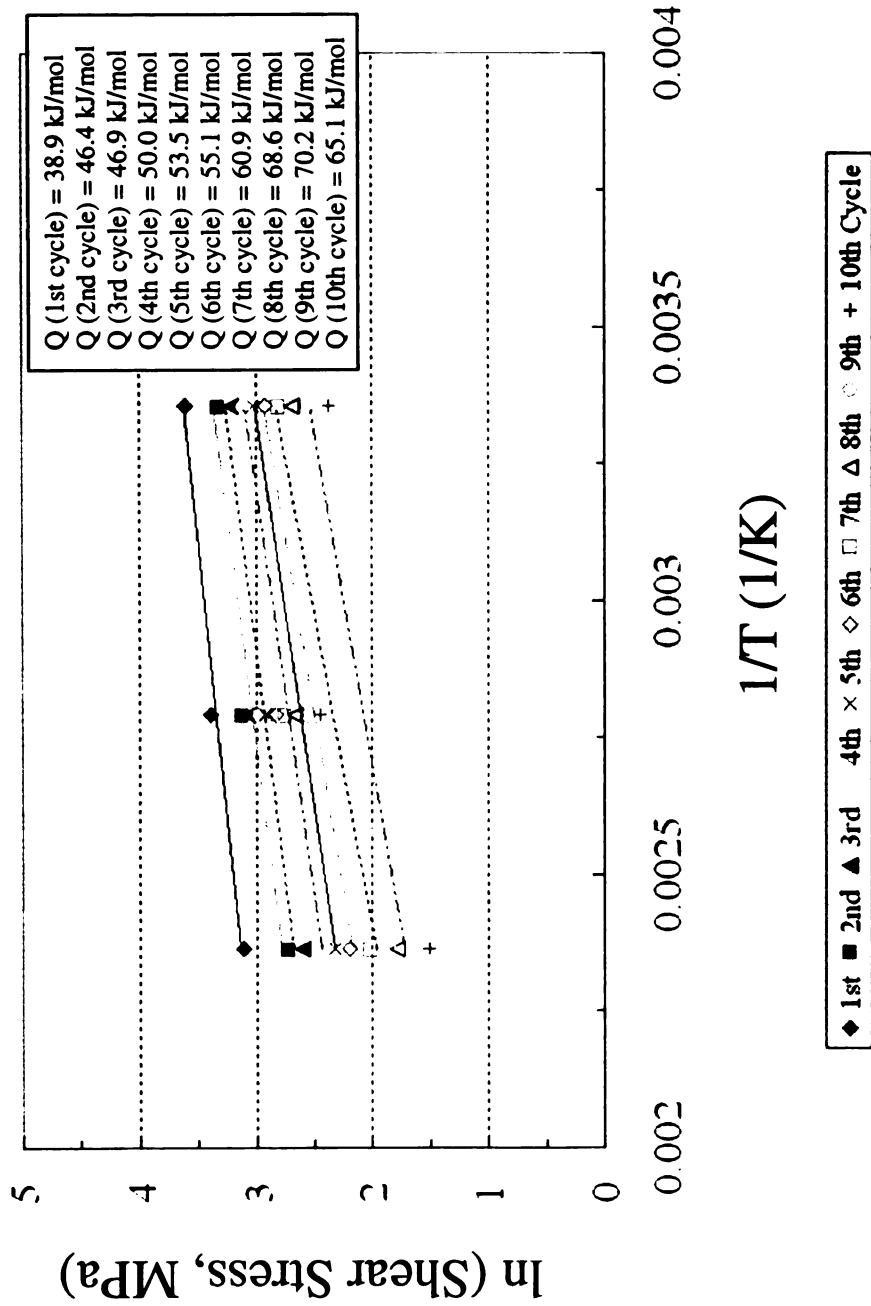


**Figure 5.10** Relationship between peak shear stress in each cycle and testing temperature. The specimens were pre-strained to a  $\gamma_p$  of 0.3 at a  $\dot{\gamma}_p$  of 0.01 /s, followed by imposing a fixed  $\gamma_c$  (0.05) and  $\dot{\gamma}_c$  (0.005 /s).

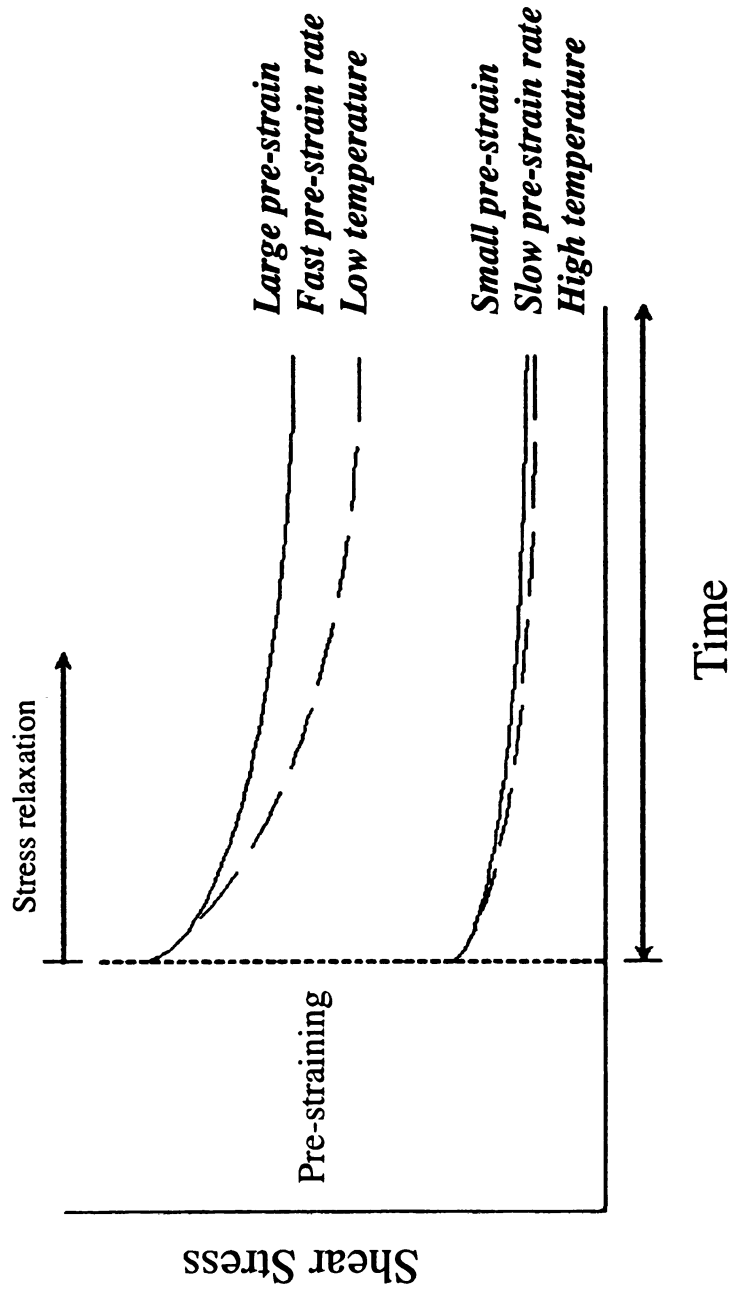


**Figure 5.11** Schematic comparison of effects of various test parameters on solder joint behavior between SR and SRC tests. Effect of each test parameter can be achieved when all other parameters were held constant. Lines in the stress relaxation regime represent the stress profile under SRC condition, and dashed lines represent that under SRC condition.

## **5.4 SUMMARY AND CONCLUSIONS**

Process and service related test parameters, such as pre-strain and pre-strain rate imposed prior to the repeated reverse strain cycling, and testing temperature, strongly affect the maximum shear stress and residual stress during each cycle. These parameters may play significant roles during actual TMF cycles of the solder joints.

Grain boundary deformation is dominated in the specimen tested at 150°C while shear-banding or combined deformation features occur in the specimen tested at lower temperatures. Microstructural features of the solder joint are also strongly affected by pre-strain conditions and testing temperatures.

Cyclic straining may be able to provide more stress relaxation in specimens deformed to higher pre-strain at a higher pre-strain rate under lower testing temperatures. At high temperature, the maximum shear stress at the subsequent cycle reaches shear stress experienced at the end of the previous cycle under repeated reverse strain cycling condition. In specimens deformed at higher temperature to a lower pre-strain at lower pre-strain rate, residual stress build-up is less significant and as a consequence cyclic straining has no significant influence on the stress relaxation behavior.

## CHAPTER 6

### **ROLES OF IMPOSED CYCLIC STRAIN AMPLITUDE AND CYCLIC STRAIN RATE ON THE CYCLIC STRESS RELAXATION BEHAVIOR OF PRE-STRAINED EUTECTIC Sn-3.5Ag SOLDER JOINTS**

#### **ABSTRACT**

The main purpose is to understand the roles of service-related parameters, such as imposed cyclic strain amplitude and cyclic strain rate, on the stress relaxation behavior of eutectic Sn-Ag solder joints. Cyclic shear straining with associated stress relaxation at the shear strain extremes imposed was carried out on pre-strained eutectic Sn-Ag solder joints with various cyclic shear straining conditions. Results from such experiments were compared with previously reported findings from monotonic shear straining and stress relaxation tests. At higher testing temperatures with a larger cyclic strain amplitude, stress states realized at the subsequent cycle are comparable to, or even gradually increase, compared to those experienced at the previous cycle, especially after few cycles. The maximum shear stress obtained at each cycle and residual stress during stress relaxation are strongly affected by cyclic strain rate. Stress relaxation during subsequent cycles of straining was found to be strongly dependant on the testing temperature, and the imposed cyclic strain amplitude and cyclic strain rate. The experiments were carried out on the eutectic Sn-Ag solder joints with about 100 $\mu$ m joint thickness, representative of those used in microelectronics. Also, there is no systematic study reporting the effects of cyclic straining conditions on the stress relaxation behavior of eutectic Sn-Ag solder in the joint configuration in published literature.

## 6.1 INTRODUCTION

Reliability and lifetime predictions of solder joints in electronic packages are a critical concern in the electronics industry. With advances in surface mount technology (SMT) and the increasing impetus for microminiaturization in emerging technologies, the ability to absorb the thermal and mechanical strains in electronic devices is degraded. Reliability of solder joints is mainly dependent on the coefficient of thermal expansion (CTE), fundamental mechanical properties, such as elastic modulus, yield strength, shear strength, etc., fatigue, and creep behavior of the entities present in the joint [104].

Prominent deformation processes occurring in a solder joint during service are creep and stress relaxation, since most solder alloys operate at a high homologous temperature ( $>0.5T_m$ ) even at room temperature [99]. One of the limitations of interconnection schemes is the degradation of mechanical contact between the bump and the substrate, resulting in a corresponding increase in the electrical contact resistance. This problem is due to the phenomenon of stress relaxation, manifested in the reduction of localized compressive pressure between the bump and the substrate [105]. During temperature changes within the electronic package, temperature gradients and CTE mismatches are usually realized as stresses in the solder joint when it is the only structural bridge. It is important to understand the stress relaxation characteristic of the solder joints for developing the reliable electronic packaging because it typically occurs in electronic packaging during thermal hold times after a change in temperature [67]. When an electronic device is in operation, the solder connections are subjected

to cyclic stresses and strains arising due to mismatches in the CTE between electronic components and the board. Most of the cyclic straining takes place within the solder region since the solder is much softer than other components. Therefore, thermomechanical fatigue (TMF) failure is likely to occur in the solder joint between solder and components [106].

To date, the cyclic relaxation characteristics of lead-free solder joints are yet to be understood. Several studies on either repeated straining or stress relaxation properties of lead-bearing as well as lead-free solders have been reported in the literature [12,24,49,51,56,64-66,100,101]. However, most of these investigations have been carried out with bulk solder specimens without the constraint effects present in a joint configuration. The microstructures of bulk solder materials inevitably are different from those of actual solder joints so that mechanical properties are quite different as well. Rhee *et al.* [107] reported the roles of pre-strain, pre-strain rate, and temperature on the stress relaxation behavior of eutectic Sn-Ag solder joints by cyclic straining with associated stress relaxation for pre-strained solder joints.

The objective of the present study is to expand the understandings of the roles of service parameters, such as cyclic strain amplitude and cyclic strain rate, on the stress relaxation behavior of eutectic Sn-Ag solder joints with about 100 $\mu$ m joint thickness, representative of those used in microelectronics, under repeated reverse shear straining with associated stress relaxation at various temperatures. Comparisons between the findings from present study, and previously reported monotonic shear straining and stress relaxation tests [99]

could identify the differences in the solder joint behavior under monotonic and repeated straining.

## 6.2 EXPERIMENTAL PROCEDURES

The effects of pre-strain, pre-strain rate, and temperature on the stress relaxation behavior of cyclic straining experiments for eutectic Sn-Ag solder joints were evaluated in Chapter 5. In this chapter, the effects of cyclic strain amplitude and cyclic strain rate on the mechanical behavior of the eutectic Sn-Ag solder joints are investigated. In order to simplify the presentation of relevant experimental details, following abbreviations are used in this chapter. The terms ' $\gamma_p$ ' and ' $\gamma_c$ ' are used to represent 'pre simple shear-strain amplitude' and 'cyclic simple shear-strain amplitude' respectively. The simple shear-strain within each tested solder joint was calculated by dividing the actual displacement imposed to the joint by its thickness. This parameter is too large to be termed as a 'shear strain', and 'simple shear-strain' is considered to be a more appropriate term. Likewise, the term 'simple shear-strain rate' is more appropriate instead of the term 'shear strain-rate' [97]. ' $\dot{\gamma}_p$ ' and ' $\dot{\gamma}_c$ ' are used for 'pre simple shear-strain rate' and 'cyclic simple shear-strain rate'. 'SRC' and 'SR' are used to represent stress relaxation with and without imposed cyclic strains respectively.

Single shear-lap solder joints were used by soldering two copper dog-bone specimens together with a eutectic Sn-Ag solder paste material obtained from a commercial source for the present study. The details of the specimen preparation and fabrication of single shear-lap solder joint used in this study are

depicted in Chapter 3.2. All mechanical tests were carried out with a thermomechanical analyzer at 25°C, 85°C, and 150°C. Although the specimens were primarily loaded in tension mode using this apparatus, the solder joints underwent simple shear states because of the joint geometry. The detailed performance and advantages, and methods used to correct for machine compliance are described in Chapter 3.2.  $\gamma_p$ ,  $\dot{\gamma}_p$ ,  $\gamma_c$ ,  $\dot{\gamma}_c$ , and testing temperatures used in the present investigation are listed in Table 6.1. During the cyclic straining part of the tests, the specimens were permitted to undergo stress relaxation, at the strain extremes, for a period of 300 seconds. This cycling was repeated for 10 times. Two different  $\gamma_p$  values of 0.2 and 0.3 were selected for the pre-straining segment of the test to facilitate comparison with previously reported findings from SR tests [99]. These pre-strains prevented the stress state from becoming negative during SRC allowing the specimens to be held in the tensile mode during cycling without buckling. After the completion of the SRC test on a given specimen, deformation structures were observed from the fine-polished side of the solder joint using SEM. The specimen was then deformed to failure to obtain the solid joint area supporting the stress by subtracting pore area in fracture surfaces from the total joint area. The actual shear stress values were obtained by dividing the load by the solder joint area that supported the loading.

In this experimental condition of cyclic shear straining with associated stress relaxation, the deformation processes involved are closely representative of those in an actual solder joint during the temperature hold periods of the actual

**Table 6.1** Testing parameters for SRC experiments.  $\gamma_c$  imposed was 0.1, and hold times at maximum and minimum shear strain extremes for stress relaxation experiments were 300 seconds.

Pre simple shear-strain, $\gamma_p$	Pre simple shear-strain rate, $\dot{\gamma}_p$ (/s)	Cyclic simple shear-strain rate, $\dot{\gamma}_c$ (/s)
0.2	0.0001	0.00005
		0.0005
		0.005
	0.001	0.00005
		0.0005
		0.005
	0.01	0.00005
		0.0005
		0.005
0.3	0.0001	0.00005
		0.0005
		0.005
	0.001	0.00005
		0.0005
		0.005
	0.01	0.00005
		0.0005
		0.005

**Note:** Experiment under each test condition was carried out at three different testing temperatures of 25°C, 85°C, and 150°C.

TMF cycle during operation of the electronic device, such as relay that operates radiator fans in automobile, cooling fans in computer, temperature control unit for appliances, etc.

## 6.3 RESULTS AND DISCUSSION

### 6.3.1 Effects of Cyclic Strain Amplitude

Experimental results obtained from fixed  $\gamma_p$ ,  $\dot{\gamma}_p$ ,  $\dot{\gamma}_c$ , and testing temperature conditions were used to identify the role of  $\gamma_c$ . In order to minimize the number of figures, the general trends observed are provided for a chosen test condition. Shear stress versus time plot obtained from the SRC experiments under  $\gamma_p$  of 0.2,  $\dot{\gamma}_p$  of 0.001 /s,  $\dot{\gamma}_c$  of 0.00005 /s, at a testing temperature of 25°C is shown in Figure 6.1 (a). The peak shear stress obtained during loading part of the test, and residual shear stress during stress relaxation period are strongly affected by the amount of imposed  $\gamma_c$ . This can be clearly observed in Figure 6.1 (b) showing the maximum shear stress experienced in each cycle as a function of number of cycles. In this figure, only positive shear stress region is presented to illustrate the important features. For a given  $\gamma_p$  and  $\dot{\gamma}_p$  followed by imposing a fixed  $\dot{\gamma}_c$  at isothermal testing temperature, the maximum shear stress experienced at first cycle is comparable in both cases since  $\gamma_p$ ,  $\dot{\gamma}_p$ , and testing temperature are the same. The maximum shear stress experienced in successive cycles in the specimen imposed to a larger  $\gamma_c$

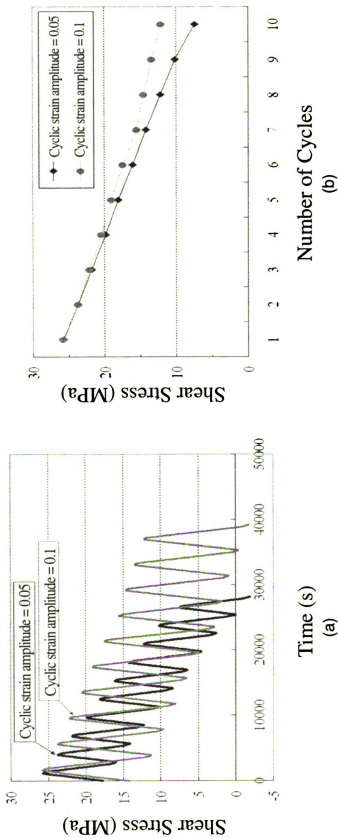


**Figure 6.1** Effects of cyclic strain amplitude on the solder joint behavior under SRC conditions. (a) SRC curves of the eutectic Sn-Ag solder joints, and (b) relationship between the maximum shear stress obtained during each cycle and number of cycles.

**Note:** Other test parameters are fixed at  $\gamma_p$  of 0.2,  $\dot{\gamma}_p$  of 0.001 /s,  $\dot{\gamma}_c$  of 0.00005 /s, and at a testing temperature of 25°C.

is higher than that in the specimen with a smaller imposed  $\dot{\gamma}_c$ . This can be observed for all  $\dot{\gamma}_c$  ranges tested except in case of  $\dot{\gamma}_c$  of 0.005 /s, as depicted in Figure 6.2, since the initial shear stress drop during stress relaxation is much larger in the specimen that experienced faster  $\dot{\gamma}_c$ . This implies that the curvature of the plot illustrating the maximum shear stress change with respect to the number of cycles depends strongly on the initial drop of maximum shear stress.

At higher temperatures, solder joint behavior affected by cyclic strain amplitude was slightly different from that at lower temperature as provided in Figure 6.3. Like the case of lower temperature experiments, the maximum shear stress experienced at first cycle is comparable for a given  $\gamma_p$  and  $\dot{\gamma}_p$  followed by imposing a fixed  $\dot{\gamma}_c$  at isothermal testing temperature. At higher testing temperatures with a larger  $\dot{\gamma}_c$ , however, stress states realized at the subsequent cycle are comparable to or even gradually increase compared to those experienced at the previous cycle after few cycles, probably due to recovery (or crack healing) process. This phenomenon can also be observed for all  $\dot{\gamma}_c$  ranges tested as illustrated in Figure 6.4.

### 6.3.2 Effects of Cyclic Strain Rate

To assess the effects of  $\dot{\gamma}_c$ , results obtained from fixed  $\gamma_p$ ,  $\dot{\gamma}_p$ ,  $\dot{\gamma}_c$ , and testing temperature conditions were used in this analysis. As shown in Figure

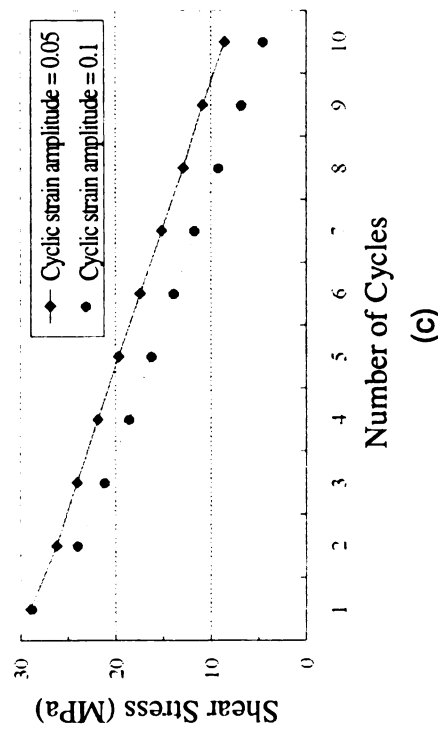
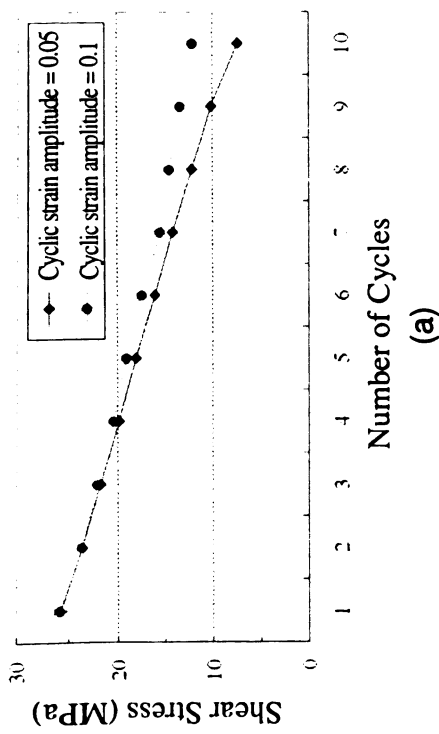
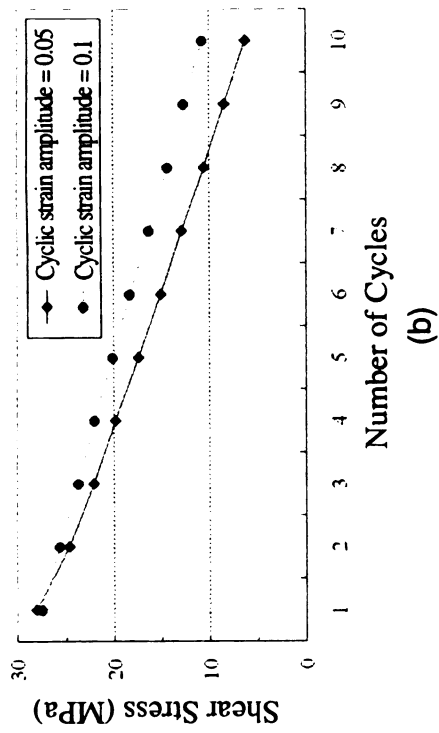


**Figure 6.2** Effects of cyclic strain amplitude on the solder joint behavior under SRC conditions as a function of cyclic strain rate. (a)  $\dot{\gamma}_c = 0.00005$  /s, (b)  $\dot{\gamma}_c = 0.0005$  /s, and (c)  $\dot{\gamma}_c = 0.005$  /s.

**Note:** Other test parameters are fixed at  $\gamma_p$  of 0.2,  $\dot{\gamma}_p$  of 0.001 /s, and testing temperature of 25°C.

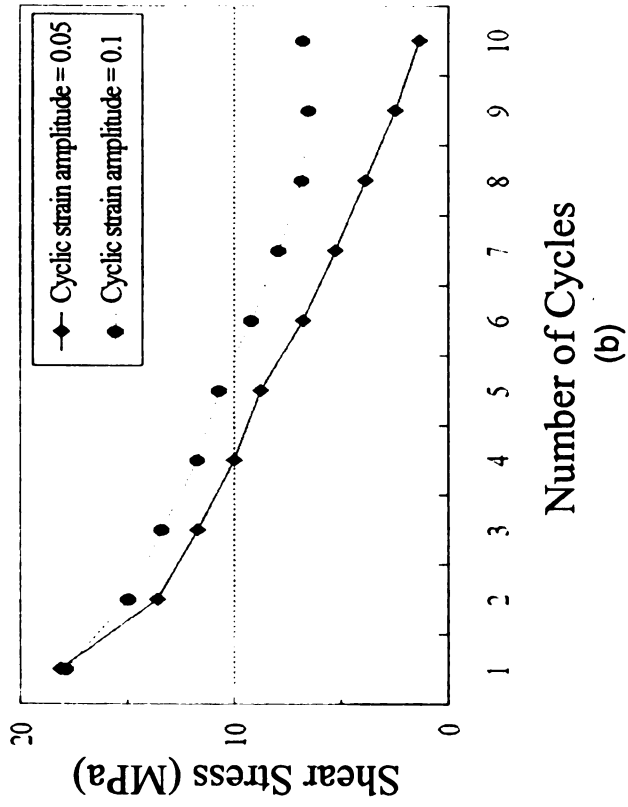
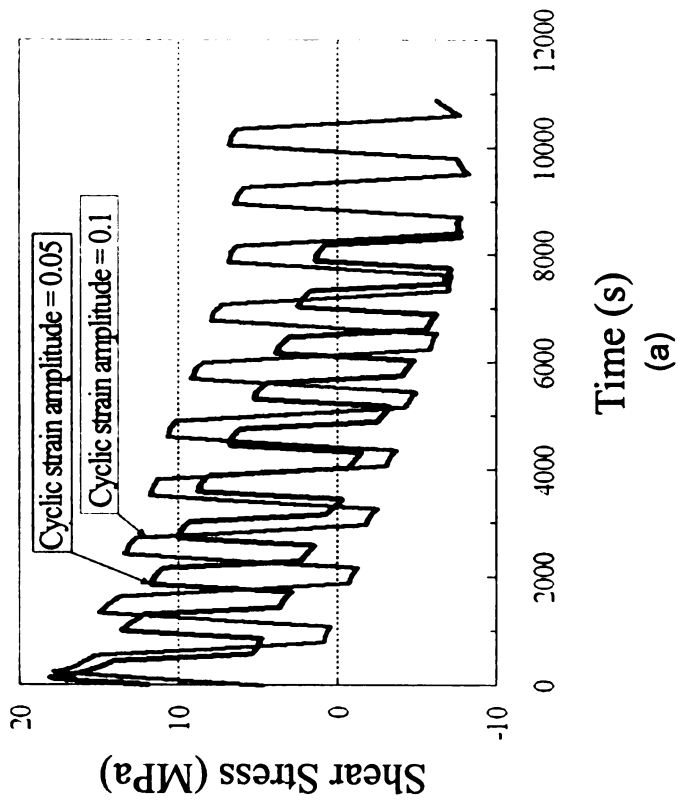


**Figure 6.3** Effects of cyclic strain amplitude on the solder joint behavior under SRC conditions. (a) SRC curves of the eutectic Sn-Ag solder joints, and (b) relationship between the maximum shear stress obtained during each cycle and number of cycles.

**Note:** Other test parameters are fixed at  $\gamma_p$  of 0.3,  $\dot{\gamma}_p$  of 0.001 /s,  $\dot{\gamma}_c$  of 0.0005 /s, and at a testing temperature of 150°C.

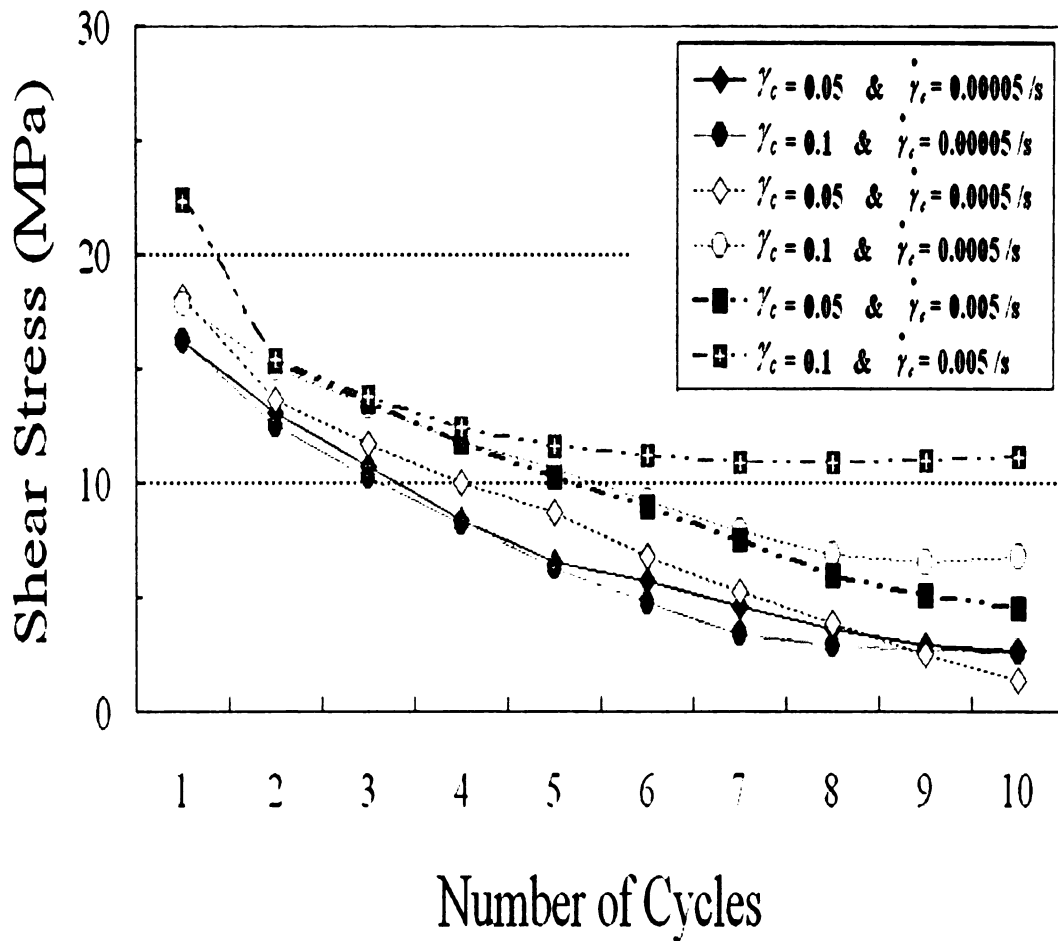


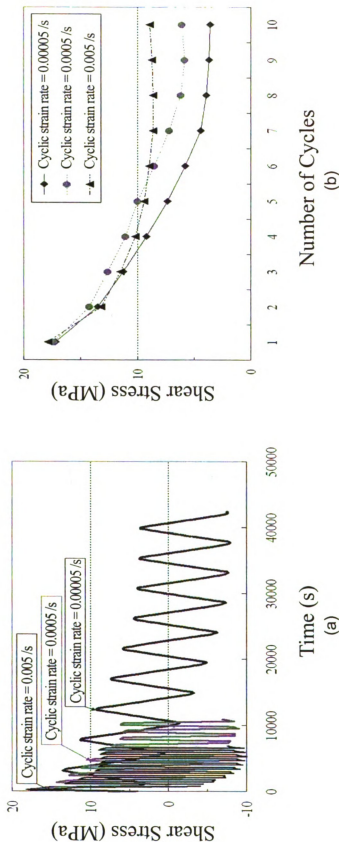
**Figure 6.4** Effects of cyclic strain amplitude on the solder joint behavior under SRC conditions as a function of cyclic strain rate.

**Note:** Other test parameters are fixed at  $\gamma_p$  of 0.3,  $\dot{\gamma}_p$  of 0.001 /s, and testing temperature of 150°C.

6.5 (a), the peak shear stress realized prior to the stress relaxation process in each cycle, and residual shear stress during stress relaxation period after 300 seconds, are strongly affected by imposed  $\dot{\gamma}_c$ . The change in maximum shear stress obtained from each cycle of the stress relaxation as a function of number of cycles for this series of experiments, is shown in Figure 6.5 (b). For a given  $\gamma_p$  and  $\dot{\gamma}_p$  followed by imposing a fixed  $\gamma_c$  under isothermal testing, the maximum shear stresses obtained at first cycle are comparable in all cases since  $\gamma_p$ ,  $\dot{\gamma}_p$ ,  $\gamma_c$  and testing temperature are the same. The stress drop at early stage of SRC condition is very sensitive to  $\dot{\gamma}_c$  imposed. Imposition of faster  $\dot{\gamma}_c$  resulted in higher maximum shear stress after few cycles although the initial shear stress drop during stress relaxation is much larger. As mentioned in earlier (section 6.3.1), stress states realized at the subsequent cycle are comparable to, or even gradually increase, compared to those experienced in previous cycle after few cycles since the experiments were carried out at higher testing temperature.

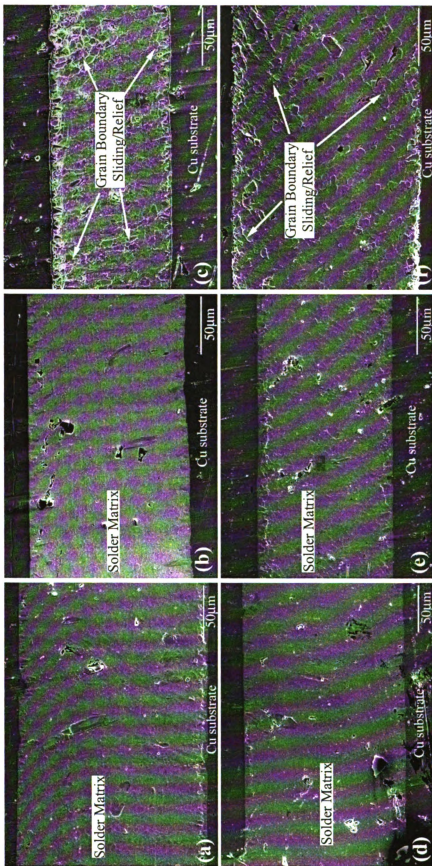
### 6.3.3 Microstructural Characterization

Figure 6.6 shows the microstructures of the side surfaces of the solder joints after the SRC tests. These specimens were subjected to a  $\gamma_p$  of 0.2 and a  $\dot{\gamma}_p$  of 0.001 /s, followed by a fixed  $\gamma_c$  of 0.1 with different  $\dot{\gamma}_c$ 's at various testing temperatures. No significant deformation can be noted at the fine-



**Figure 6.5** Effects of cyclic strain rate on the solder joint behavior under SRC conditions. (a) SRC curves of the eutectic Sn-Ag solder joints, and (b) relationship between the maximum shear stress obtained during each cycle and number of cycles.

**Note:** Other test parameters are fixed at  $\dot{\gamma}_p$  of 0.3,  $\dot{\gamma}_p$  of 0.001 /s,  $\gamma_c$  of 0.1, and at a testing temperature of 150°C.



**Figure 6.6** Microstructures of the solder joint side surfaces after the SRC tests. All specimens were pre-strained to a

$\dot{\gamma}_p$  of 0.2 and  $\dot{\gamma}_p$  of 0.001 /s prior to the first cycle, followed by imposing a fixed  $\dot{\gamma}_c$  of 0.1 and  $\dot{\gamma}_c$  's of

(a) 0.00005 /s at 25°C, (b) 0.00005 /s at 85°C, (c) 0.00005 /s at 150°C, (d) 0.0005 /s at 25°C, (e) 0.0005 /s at 85°C, and (f) 0.005 /s at 150°C.

polished side surface of the specimen pre-strained to a  $\gamma_p$  of 0.2, at the level of magnification employed, in the specimens tested at 25°C and 85°C, since the magnitude of pre-strain is relatively small. However, grain boundary deformation features can be observed in the specimens tested at 150°C (Figure 6.6 (c) and (f)) under similar straining conditions. The microstructures of the side surfaces of the solder joints after the SRC tests in the specimen pre-strained to a  $\gamma_p$  of 0.3 and a  $\dot{\gamma}_p$  of 0.001 /s, followed by a fixed  $\gamma_c$  of 0.1 with different  $\dot{\gamma}_c$ 's at various testing temperatures are provided in Figure 6.7. Unlike that in the specimens pre-strained to a  $\gamma_p$  of 0.2, the deformation feature by a shear-banding mode can be observed in the specimens tested at 25°C. The specimen imposed to a faster  $\dot{\gamma}_c$  at 25°C (Figure 6.7 (d)) has more concentrated shear bands as compared to the specimen imposed to a slower  $\dot{\gamma}_c$  at the same temperature (Figure 6.7 (a)). Deformation features in the specimen deformed at a higher temperature (150°C) are mostly grain boundary deformations, whereas a combination of shear banding and grain boundary deformation is present in the specimens tested at an intermediate temperature (85°C). The grain boundary deformations and shear bands are aligned with respect to the shear direction at this temperature. Similar trends in the deformation features have also been observed in the previously reported monotonic shear test results [97], SR test results [99], and SRC test results [107].

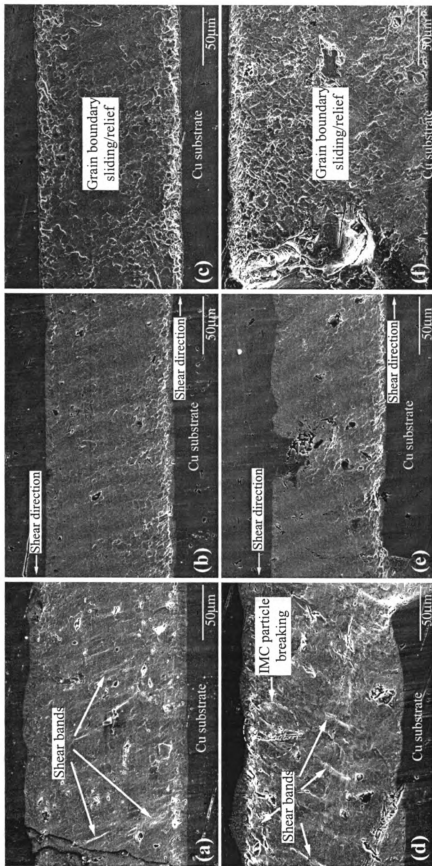


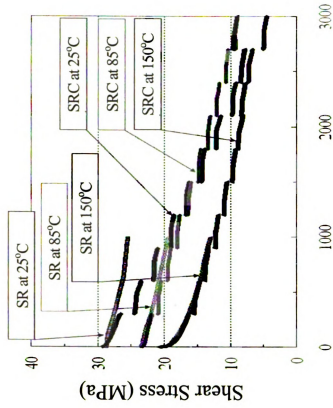
**Figure 6.7** Microstructures of the solder joint side surfaces after the SRC tests. All specimens were pre-strained to a

$\dot{\gamma}_p$  of 0.3 and  $\dot{\gamma}_c$  of 0.001 /s prior to the first cycle, followed by imposing a fixed  $\dot{\gamma}_c$  of 0.1 and  $\dot{\gamma}_c$  's of (a) 0.00005 /s at 25°C, (b) 0.00005 /s at 85°C, (c) 0.00005 /s at 150°C, (d) 0.0005 /s at 25°C, (e) 0.0005 /s at 85°C, and (f) 0.005 /s at 150°C.

### 6.3.4 Comparisons of the Solder Joint Behavior between SR and SRC Conditions

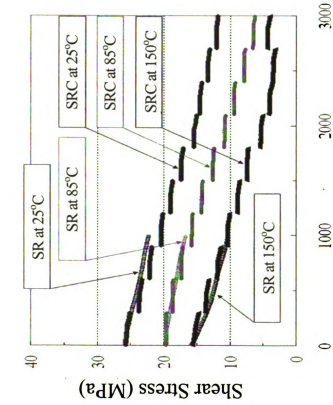
The comparison of shear stress versus time plots obtained from stress relaxation part of the test between SR and SRC conditions is shown in Figure 6.8. Stress decreases more rapidly under SRC condition as compared to SR tests especially at lower temperature with a faster  $\dot{\gamma}_c$ , since repeated reverse stresses may facilitate easy accommodation of microstructural damage [107].

The difference in the extent of the stress drop during stress relaxation under SRC conditions depends on the imposed  $\dot{\gamma}_c$ . At slower  $\dot{\gamma}_c$ , shear stress states realized at the subsequent cycle are lower than those experienced at the end of the previous cycle for all testing temperature ranges except at higher testing temperature (150°C) after few cycles. At higher testing temperatures with a faster  $\dot{\gamma}_c$ , however, stress states after SRC condition are comparable to that after SR tests since the maximum shear stress realized at the subsequent cycle reaches or is superior to shear stress experienced at the end of the previous cycle, probably due to crack healing (recovery) process. This implies that both  $\dot{\gamma}_c$  imposed and testing temperature can play significant roles for solder joint behavior under repeated reverse stressing. Cyclic shear strains and dwell periods at strain extremes strongly affect the formation and growth of microcracks or voids within the solder joints. Presence of tensile stresses around these microcracks during cyclic straining appears to be more damaging than compressive stresses. At a higher temperature, these microcracks may be



Time (stress relaxation portion only, s)

(a)

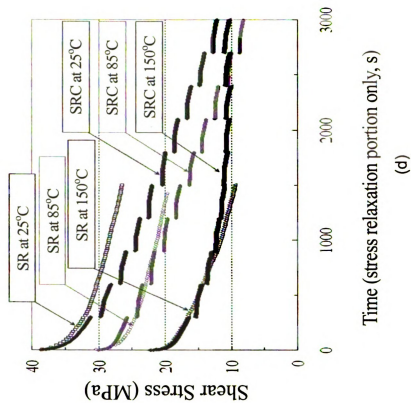


Time (stress relaxation portion only, s)

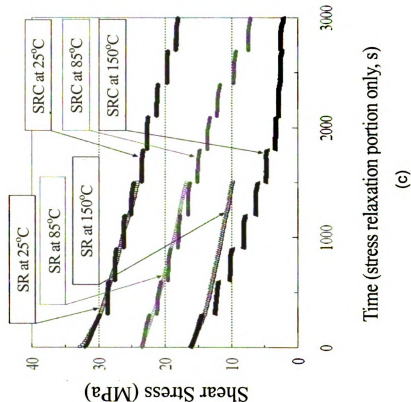
(b)

**Figure 6.8** Comparison of shear stress versus time plots obtained from stress relaxation part of the test between SR and SRC tests. The specimens were pre-strained to (a)  $\dot{\gamma}_p$  of 0.2 at  $\dot{\gamma}_c$  of 0.00005 /s, (b)  $\dot{\gamma}_p$  of 0.2 at  $\dot{\gamma}_c$  of 0.005 /s, (c)  $\dot{\gamma}_p$  of 0.3 at  $\dot{\gamma}_c$  of 0.00005 /s, and (d)  $\dot{\gamma}_p$  of 0.3 at  $\dot{\gamma}_c$  of 0.005 /s. (cont'd)

**Note:** Other test parameters are fixed at  $\dot{\gamma}_p$  of 0.001 /s and  $\dot{\gamma}_c$  of 0.1.



Time (stress relaxation portion only, s)  
(c)



Time (stress relaxation portion only, s)  
(d)

Figure 6.8 (cont'd)

healed or shrunk during cyclic straining whereas the damage due to these microcracks can be accumulated easier at a lower temperature.

Room temperature shear test results obtained from the specimens already tested under SRC condition at various temperatures are presented in Figure 6.9. The SRC specimen tested at 150°C possess the highest room temperature shear strength value and that tested at 25°C has the lowest room temperature shear strength value. This implies that the recovery (or crack healing) process at higher testing temperature during SRC may play a significant role for the strength of this solder joints. In addition, relaxation (a crack healing) in SRC specimen tested at lower testing temperature will be insignificant.

The creep parameters for the eutectic Sn-Ag solder joints under SRC conditions can be extracted by fitting the data to a power-law creep equation since homologous temperatures of such solder joints are greater than  $0.5T_m$  even at room temperature;

$$\dot{\gamma} = A \tau^n \exp\left(-\frac{Q}{RT}\right)$$

where, ' $\dot{\gamma}$ ' is the steady-state shear-strain rate in creep, 'A' is the material constant, ' $\tau$ ' is the shear stress, ' $n$ ' is the stress exponent, 'Q' is the creep activation energy, 'R' is the gas constant, and 'T' is the absolute temperature. Figure 6.10 illustrates the relationship between simple shear-strain rate and shear stress obtained from the stress relaxation part of the SRC tests along with that obtained from SR tests (open symbols) [99]. The stress exponents, which depend on the operating creep mechanisms, under such SRC condition range

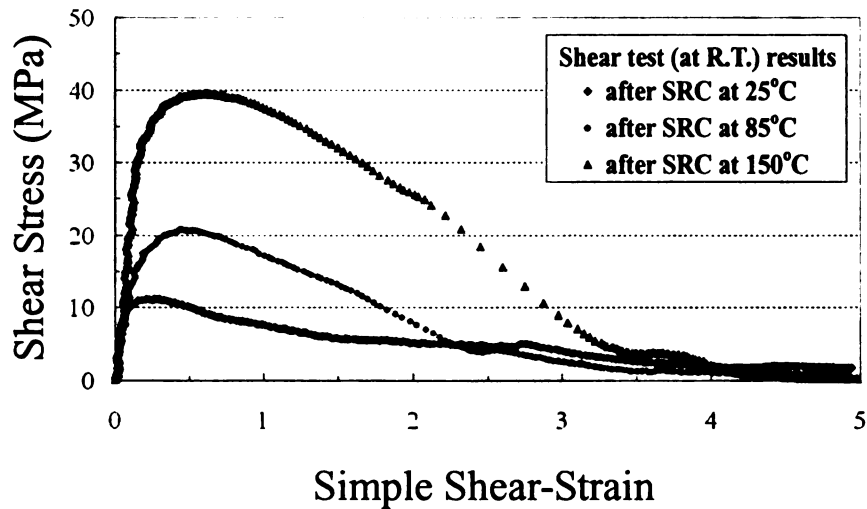


**Figure 6.9** Shear test results obtained from the specimens tested SRC at various temperatures. All specimens were pre-strained to a  $\gamma_p$  of 0.3 and  $\dot{\gamma}_p$  of 0.001 /s prior to the first cycle, followed by imposing a fixed  $\gamma_c$  of 0.05 and  $\dot{\gamma}_c$  of 0.0005 /s for SRC experiments.

**Note:** Shear tests were carried out at room temperature under simple shear-strain rate of 0.01 /s.

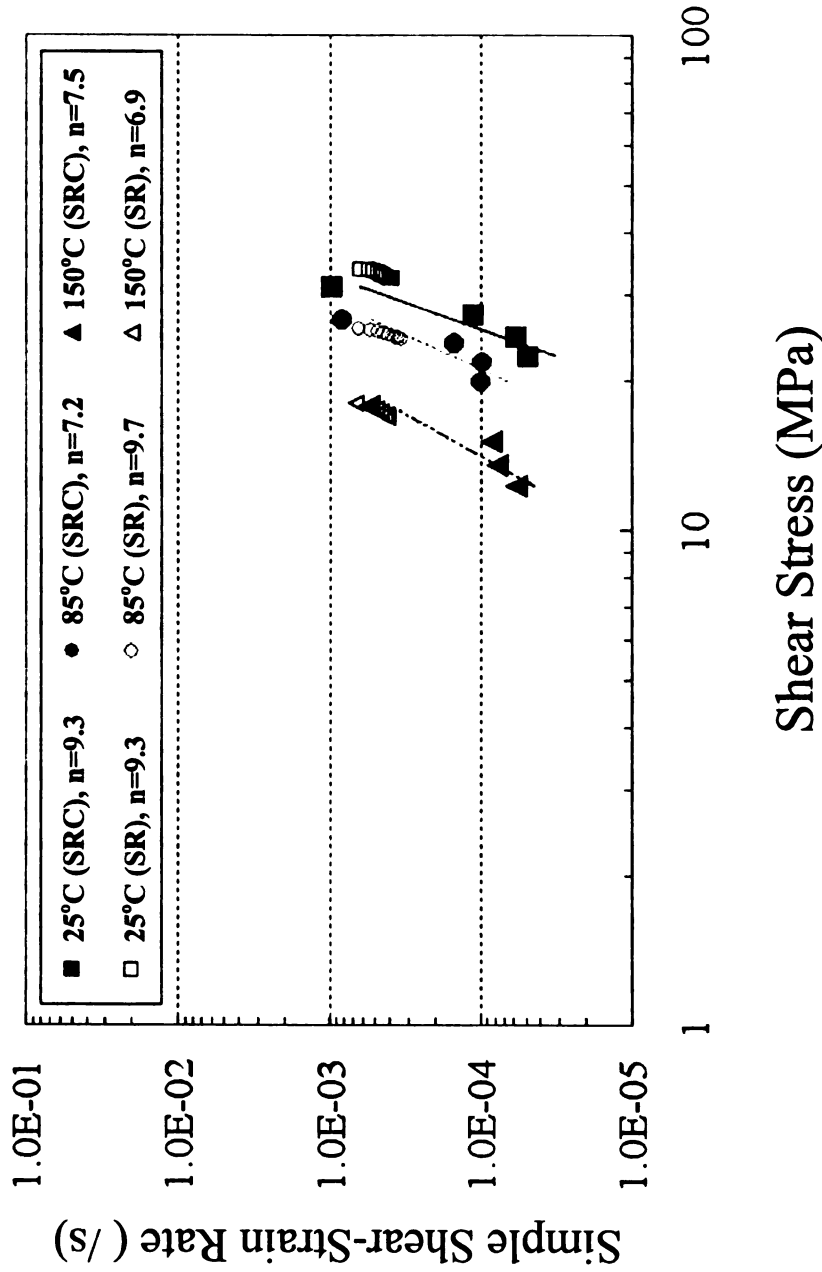


**Figure 6.10** Relationship between simple shear-strain rate and peak shear stress in each cycle obtained from the stress relaxation part of the test. The specimens were pre-strained to a  $\gamma_p$  of 0.3 at a  $\dot{\gamma}_p$  of 0.001 /s, followed by imposing a fixed  $\dot{\gamma}_c$  of 0.1 and  $\dot{\gamma}_c$  of 0.005 /s.

from 7.2 to 9.3, and are comparable to the stress exponents reported in the literature [74]. Although the stress exponents obtained are similar, the simple shear-strain rates vary with respect to the test conditions. For the same stress level, simple shear-strain rates under SRC condition are much larger than those under SR condition at low temperature. However, values for both conditions are much closer at higher temperatures. This can be attributed to the continuing damage accumulation at lower temperature under such test condition as depicted in Figures 6.8 (d) and 6.9.

Figure 6.11 displays the relationship between peak shear stress in each cycle and testing temperature under SRC tests using data from Figure 6.10. The creep activation energy values obtained from stress relaxation during first few cycles are consistent with the values obtained in prior creep studies on joints made with this solder [74], and they keep increasing with subsequent cycles suggesting that stress relaxation becomes more difficult with increasing number of cycles. However, the creep activation energy values during last few cycles decrease with increasing number of cycles because the shear stress values of each cycle at higher temperature increase as depicted in Figure 6.8.

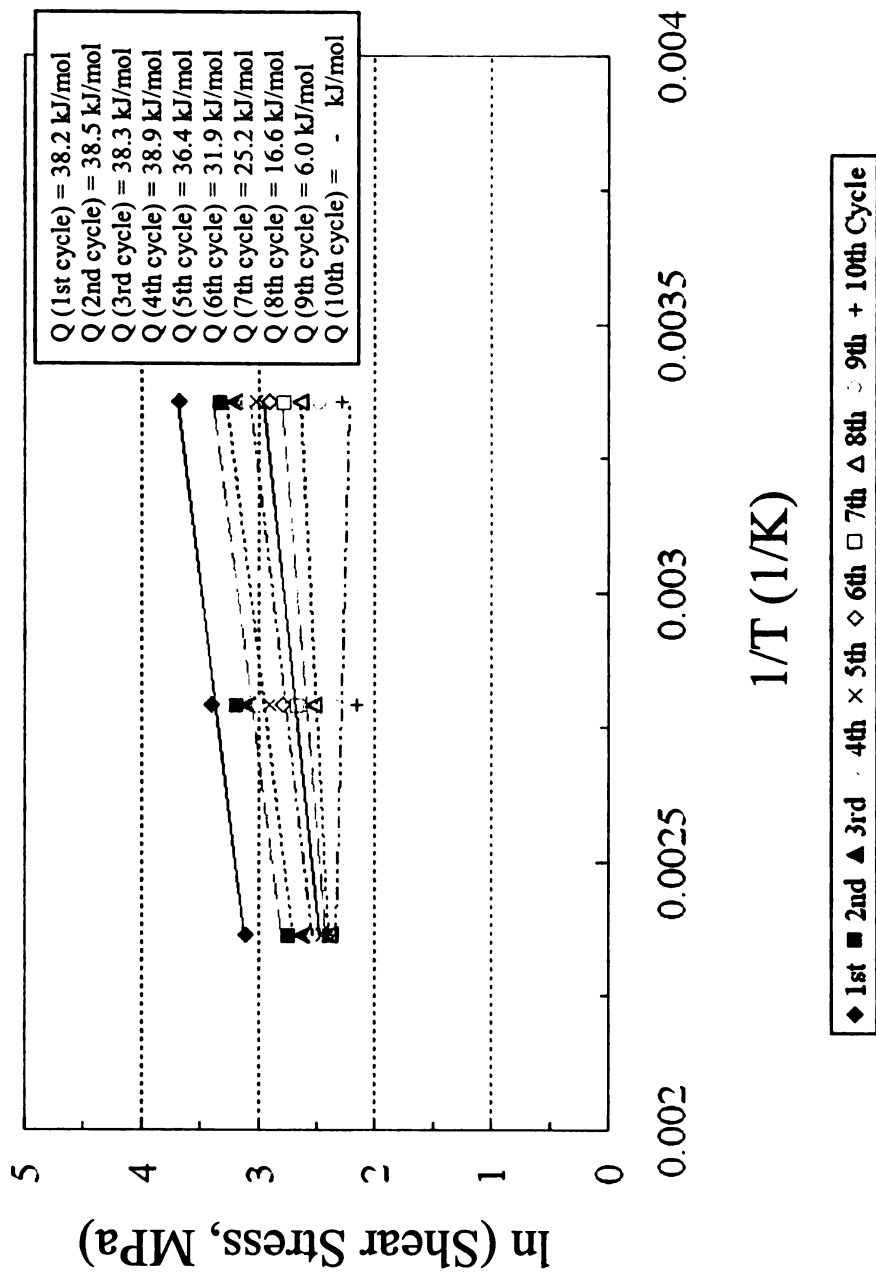


**Figure 6.11** Relationship between peak shear stress in each cycle and testing temperature. The specimens were pre-strained to a  $\gamma_p$  of 0.3 at a  $\dot{\gamma}_p$  of 0.001 /s, followed by imposing a fixed  $\dot{\gamma}_c$  of 0.1 and  $\dot{\gamma}_c$  of 0.005 /s.

## 6.4 SUMMARY AND CONCLUSIONS

Service-related test parameters, such as cyclic strain amplitude and cyclic strain rate imposed during the repeated reverse strain cycling, strongly affect the maximum shear stress and residual stress during each cycle. These parameters may play significant roles during actual TMF cycles of the solder joints.

At higher testing temperatures with a larger cyclic strain amplitude, stress states realized in subsequent cycle are comparable to, or even gradually increase, compared to those experienced in the previous cycle after few cycles.

Grain boundary deformation is dominated in the specimen tested at 150°C while shear-banding or combined deformation features occur in the specimen tested at lower temperatures. Microstructural deformation features of the solder joint are also strongly affected by cyclic straining parameters ( $\gamma_c$ ,  $\dot{\gamma}_c$ ) and testing temperatures.

At high temperature, processes such as crack healing (or recovery) can take place whereas at lower temperature, microstructural damage may accumulate.

## CHAPTER 7

### DISCUSSION

#### **CREEP DEFORMATION MECHANISMS FOR CYCLIC SHEAR STRAINED EUTECTIC Sn-Ag SOLDER JOINTS**

As shown in Chapters 5 (Figure 5.10) and 6 (Figure 6.11), the creep activation energy values for each cycle, obtained from stress relaxation period of the cyclic shear straining with associated stress relaxation experiments, vary with number of cycles. Activation energy exhibits an increasing trend during successive stress relaxation periods. This feature may be explained by considering different creep mechanisms.

There are several mechanisms that can contribute to creep in metals. The rate-controlling mechanisms are dependent on both stress level and temperature, and are related to diffusion processes. There are three basic mechanisms that can be responsible for creep [108-110]:

- i) Dislocation creep (dislocation glide and dislocation climb)
- ii) Diffusion creep (diffusional flow)
- iii) Grain boundary sliding.

Dislocation creep involves the dislocations moving along slip planes (dislocation glide) and overcoming barriers by thermal activation (dislocation climb). This mechanism typically occurs at moderate to high temperatures and stresses. Dislocation glide occurs at relatively high stress level of  $\sigma/G > 10^{-2}$ . This mechanism results in work hardening because intersecting or interfering planar glide cannot pass one another, resulting in dislocation pile-ups. Dislocation climb facilitates movement of dislocation around one another and

thus allows continued strain without work hardening. This mechanism occurs above  $T/T_m = 0.5$  for stress range of  $10^{-4} < \sigma/G < 10^{-2}$ , and is responsible for steady-state creep, where rate of dislocation generation is almost equal to rate of dislocation annihilation by way of recovery. Dislocation climb involves the movement of dislocations which overcome barriers by thermally assisted mechanisms such as the diffusion of vacancies or interstitials. In this mechanism, atoms diffuse into or out of dislocation core leading to dislocation climb. This model predicts a stress exponent ( $n$ ) in the power-law creep equation of 3 to 8 (commonly 5). Dislocation creep mechanism can be applied for a high temperature creep where the activation energy for creep is close to that of lattice self-diffusion ( $Q_c \cong Q_l$ ), and for a low temperature creep where the activation energy for creep is that of pipe diffusion ( $Q_c \cong Q_{p,d}$ ) along dislocation cores.

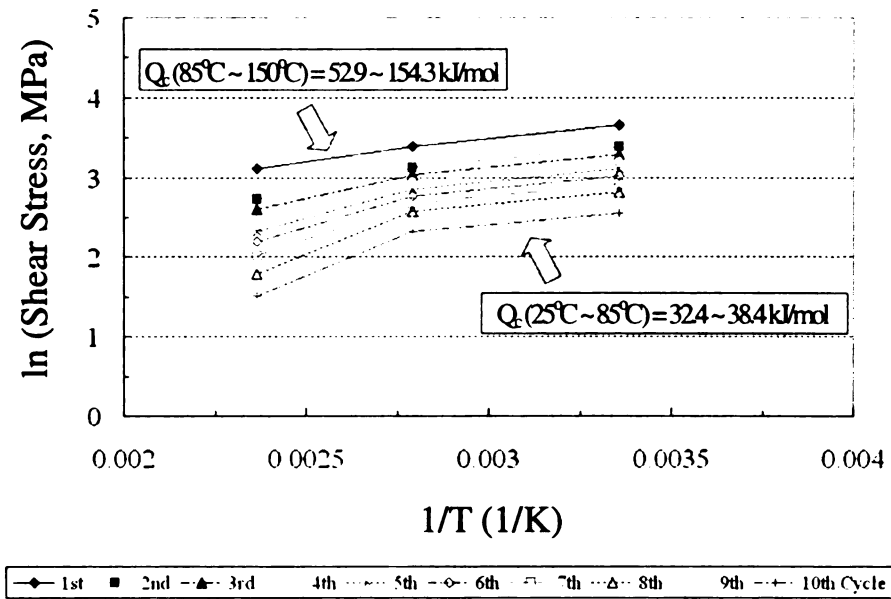
Diffusion creep involves the flow of vacancies and interstitials through a crystal under influence of applied stress and temperature. This becomes the controlling-mechanism at high temperatures and relatively low stress level of  $\sigma/G < 10^{-4}$ . Two distinct mechanisms, Nabarro-Herring creep and Coble creep, are considered in this regime. Nabarro-Herring creep involves the stress-driven atomic diffusion (no dislocation glide) within the grains. The atoms move from regions experiencing compressive stresses to those experiencing tensile stresses under the applied stress. Simultaneously, there is a corresponding flow of vacancies in the opposite direction leading to elongation of the grains. Coble creep is driven by vacancy concentration gradient along the grain boundaries in a

polycrystalline and the surface of a single crystal. Coble creep predominates at relatively lower temperatures than those at which Nabarro-Herring creep is operative. Diffusion creep predicts a stress exponent of  $\sim 1$ , and the activation energy values close to that of lattice self-diffusion ( $Q_c \equiv Q_l$ ) for Nabarro-Herring creep and that of grain boundary diffusion ( $Q_c \equiv Q_{g,b}$ ) for Coble creep.

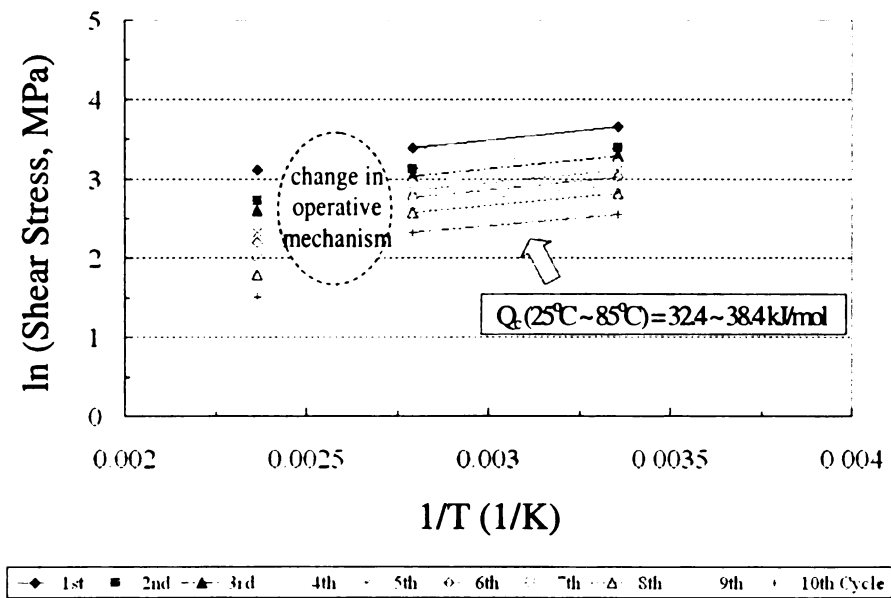
Grain boundary sliding contributes in tertiary creep to the intercrystalline crack initiation and propagation. The onset of tertiary creep is a sign that structural damage has occurred in an alloy. Rounded and wedge shaped voids are usually seen at the grain boundaries, and the mechanism of void formation involves grain boundary sliding which occurs under the imposition of shear stresses acting on the boundaries. In addition to grain boundary sliding, some accommodation process is required to maintain material continuity during the sliding process such as diffusion and boundary migration. It has been known that the grain boundary sliding must also be present during diffusion creep process to maintain materials continuity.

The dominant creep mechanism of the tested condition can be identified by comparing the experimentally obtained values of  $n$  and  $Q_c$  with those predicted since each creep mechanism predicts unique range of values of  $n$  and  $Q_c$ . For instance, one can predict rate-controlling creep mechanism changes for the test condition such that the creep activation energy values are varied as mentioned earlier. The stress exponent values obtained from the specimens pre-strained to a pre simple shear-strain of 0.3 at a pre simple shear-strain rate of 0.01 /s, followed by imposing a fixed cyclic simple shear-strain of 0.05 and cyclic simple

shear-strain rate of 0.005 /s (Figure 5.10) are ranging from 6.9 to 9.7, and the creep activation energy values at low and high temperature regimes are varied as shown in Figure 7.1 (a). The stress exponent range of such test condition seems to be a regime of dislocation creep. The creep activation energy values are different at low and high temperature regimes, suggesting that different mechanisms may be operative. Creep activation energy values for Sn with respect to the different rate-controlling mechanisms can be found in the literature [111], and these are  $Q_l \cong 108$  kJ/mol,  $Q_{g,b} \cong 70$  kJ/mol,  $Q_{p,d} \cong 40 \sim 64$  kJ/mol respectively. In this test condition, therefore, the dislocation creep may be controlled by pipe diffusion and/or grain boundary diffusion at low temperature regime. However, the creep activation energy values are widely varied at high temperature since different mechanism may be operative at this temperature regime. In other words, creep activation energy values obtained from the regression lines between 85°C and 150°C may not be realistic representation of contributing factors. This implies that there may be a possible change in operative mechanism within this temperature regime; such features have been documented from mechanical test results and microstructural characteristics of the same solder joints as described in earlier chapters. Therefore, Figure 7.1 (b) is considered to be a more appropriate expression for this condition.



(a)



(b)

**Figure 7.1** Creep activation energy values obtained from (a) both low and high temperature regimes, and (b) low temperature regime only. The specimens were pre-strained to a  $\dot{\gamma}_p$  of 0.3 at a  $\dot{\gamma}_p$  of 0.01 /s, followed by imposing a fixed  $\dot{\gamma}_c$  of 0.05 and  $\dot{\gamma}_c$  of 0.005 /s.

## **CHAPTER 8**

### **SUMMARY**

The significant findings of present studies can be summarized as follows:

( i ) Isothermal shear stress versus simple shear-strain behavior

Both peak shear stress and flow stress level were strongly dependent on testing temperature and simple shear-strain rate. The peak shear stress and the flow stress level decreased with increasing testing temperature, and with decreasing simple shear-strain rate. The effect of simple shear-strain rate on the peak shear stress was more significant at temperature regimes less than 125°C. The deformation structure of specimens deformed at higher temperature region of 125°C to 150°C was dominated by grain boundary deformation while that at lower temperatures it was dominated by shear banding. Faster simple shear-strain rates were found to cause concentrated deformation in localized region, while slower simple shear-strain rates resulted in diffused deformation characteristics. Changes in the microstructural characteristics in specimens deformed at various temperatures ranging from 25°C to 150°C may indicate a possible change in operative mechanism in low and high temperature regimes that affect the mechanical behavior of eutectic Sn-Ag solder joints. The power-law stress exponent and the activation energy for creep values obtained from the shear tests were consistent with previous findings from steady-state creep tests.

## ( ii ) Monotonic stress relaxation behavior

The peak shear stress during the pre-loading part of the test was strongly affected by the pre-strain, rate of pre-strain, and testing temperature. The peak shear stress increased with increasing simple shear-strain and simple shear-strain rate imposed prior to the stress relaxation at a fixed testing temperature. The peak shear stress decreased with increasing testing temperature for a given pre-strain condition. Residual shear stress resulting from the stress relaxation period decreased with increasing testing temperature at a given pre-strain. This value also increased with increasing simple shear-strain and simple shear-strain rate at a fixed testing temperature. Grain boundary deformation was dominated in the specimen tested at 150°C, while shear-banding was occurred in the specimen tested at lower temperatures. The stress exponent values obtained from the stress relaxation part of the tests were dependent on the pre-strain conditions prior to the stress relaxation, and testing temperature. Faster ramp-rates may cause higher resultant residual stress as compared to slower ramp-rates.

## ( iii ) Cyclic straining with associated stress relaxation behavior

Process and service related test parameters, such as pre-strain and pre-strain rate imposed prior to the repeated reverse strain cycling, cyclic strain amplitude and cyclic strain rate imposed during such cyclic straining, and testing temperature, strongly affected the maximum shear stress and residual stress during each cycle. These parameters may play significant roles during actual

TMF cycles of the solder joints. Grain boundary deformation was dominated in the specimen tested at 150°C, while shear-banding or combined deformation features occurred in the specimen tested at lower temperatures. Microstructural features of the solder joint were also strongly affected by pre-strain parameters, cyclic straining parameters, and testing temperatures. Cyclic straining may be able to provide more stress relaxation in specimens deformed to higher pre-strain at a higher pre-strain rate under lower testing temperatures. At high temperature, the maximum shear stress at the subsequent cycle reached (or superior to) shear stress experienced at the end of the previous cycle under repeated reverse strain cycling condition, whereas microstructural damage may be accumulated easier at a lower temperature. In specimens deformed at higher temperature to a lower pre-strain at lower pre-strain rate, residual stress build-up was less significant and as a consequence cyclic straining has no significant influence on the stress relaxation behavior. At higher testing temperatures with a larger cyclic strain amplitude, stress states realized in subsequent cycle were comparable to, or even gradually increased, compared to those experienced in the previous cycle after few cycles.

## **APPENDICES**

## **APPENDIX A**

## **APPENDIX A**

### **MICROMECHANICAL CHARACTERIZATION OF THERMOMECHANICALLY FATIGUED LEAD-FREE SOLDER JOINTS**

#### **ABSTRACT**

Nanoindentation testing (NIT) was used to investigate micromechanical properties of (i) as-fabricated, (ii) thermomechanically fatigued, and (iii) thermomechanically fatigued and then crept lead-free solder joints. NIT also served to generate information for database on lead-free solder joints. Sn-Ag based solder materials used in this study included a binary eutectic alloy, one ternary alloy, and two quaternary alloys. Thermomechanically fatigued solder joints were thermally cycled for 0, 250, 500, 1000 cycles between  $-15^{\circ}\text{C}$  ~  $150^{\circ}\text{C}$ . Using NIT, mechanical properties such as hardness, elastic modulus, strength trends, creep behavior, and stress exponent for power-law creep were obtained on small (nominally,  $100\mu\text{m}$  thick) solder joints. Because the volume of material probed by the indenter during NIT is small and highly localized, the properties observed strongly depended on the particular joint microstructure of the indent location. Scanning electron microscope (SEM) was used to image the nano indents and monitor deformation and fracture events that resulted from the indenting.

## 1 INTRODUCTION

With advances in surface mount technology and the increasing push for micro-miniaturization in emerging technologies in the transportation sector, there is a need for solders that can perform in more rigorous environments where Pb-Sn solders' thermal and mechanical capabilities are exceeded [17,18]. Solders used in automobile under-the-hood applications are subjected to extremely harsh operational environments, where thermal/mechanical loading in static and cyclic manners promote microstructure evolution, creep, fatigue, creep/fatigue damage [19], stress relaxation, crack propagation and fracture [20], therefore requiring solders that are capable of higher performance and reliability [17,21]. Ideally, a replacement for Pb-Sn solders would have a moderate strength, good ductility, possess an appropriate melting temperature, be cost effective, have similar solderability, and be less toxic to the environment [112,113].

Alternatives to Pb-Sn solders consist of a variety of lead-free alloys along with some with incorporated metallic, non-metallic and intermetallic reinforcements. Eutectic Sn-3.5Ag alloy has received the most emphasis in the search for a replacement for the Pb-Sn solder [91]. This alloy complies mostly with the rationale for the search for an alternative. It lacks, in general, the toxicity problems of lead-bearing solders and possesses properties that meet the requirements. Eutectic Sn-Ag solder has a melting temperature of 221°C, which is higher than Pb-based systems with a melting temperature of 183°C [1]. In the ongoing venture to develop an appropriate replacement for Pb-Sn solders, ternary and quaternary alloys are also being studied.

The conventional approach for assessing the mechanical behavior of solder materials such as tension, compression, hardness, creep, fatigue testing, etc. cannot be readily used to study the micromechanical properties of actual microelectronic solder joints because of size constraints, and furthermore, the microstructure of the joint is significantly different compared to bulk solder materials. Submicron indentation testing represents an alternative approach [21,70]. By measuring the force and the indent depth of indentations made in actual solder joints, it is possible to obtain information about the elastic and plastic deformation properties of the solder joints. Submicron indentation provides information about the micromechanical properties and deformation processes of solder joints that cannot be obtained easily by other means [21,71].

This NIT investigation enabled the determination of mechanical properties of micro-size solder joints in the (i) as-fabricated, (ii) thermomechanically fatigued, and (iii) thermomechanically fatigued and then crept conditions. Moreover, the microphase constituents present in the solder joints were mechanically probed to obtain values of hardness, elastic modulus, and the creep parameters. Load versus displacement data obtained from NIT was used to compare deformation behavior of microphases present in the solder joints. NIT allows for creep behavior to be evaluated in  $\sim 100\mu\text{m}$  thick solder joints giving results comparable to conventional methods [72,74,75,80,89].

## **2 EXPERIMENTAL PROCEDURES**

### **2.1 Materials and Solder Joints Preparation**

Four different compositions of lead-free solder paste materials, a binary eutectic Sn-Ag, one ternary alloy (Sn-4.0Ag-0.5Cu), and two quaternary alloys (Sn-2.5Ag-0.5Cu-0.5Ni and Sn-2.0Ag-1.0Cu-1.0Ni) were used in the present study. These lead-free solder pastes were obtained from a commercial source.

Single shear lap joints were produced by soldering two dog-bone shaped copper strips using the four different solder pastes. The overall dimensions of the solder joints and detailed experimental methods used for producing solder joints used in this study are described in Chapter 3.2, and the TMF testing and creep testing methodologies used can be found elsewhere [72,74,75,80,89]. Nominally the solder joint thickness was  $\sim 100\mu\text{m}$  with  $1\text{mm} \times 1\text{mm}$  solder area. Solder joints made with the four different kinds of solders were subsequently thermomechanically fatigued for 0, 250, 500, 1000 thermal cycles between  $-15^\circ\text{C}$  and  $150^\circ\text{C}$ . Thermomechanically fatigued solder joints were also subjected to creep testing to assess residual creep properties [62]. After completion of each set of experiments, SEM was used to observe and photographically image microstructural evolution and deformation trends [63].

### **2.2 Nanoindentation Testing**

NIT was conducted on actual solder joints mentioned above. These tests were carried out with a Nanoindenter XP<sup>TM</sup> made by MTS Corporation. To evaluate micromechanical properties of various solder joints, two sets of

experiments were performed using nanoindenter. The first set of NIT experiments entailed making nanoindents on each micro-constituent (e.g. an  $\text{Ag}_3\text{Sn}$  or  $\text{Cu}_6\text{Sn}_5$  intermetallic compound (IMC) particle embedded in the solder matrix) of the various solder joints to obtain their micromechanical properties. The second set of NIT experiments involved making an array of indents starting in the Cu substrate, and then progressing through the IMC layer with termination in the solder matrix region within the solder joints. This linear array of indents made a very shallow angle ( $\sim 10^\circ$ ) to the solder/substrate interface such that regions near this interface could be micromechanically probed. Using such an array during NIT allows sampling of all constituent regions of the solder joint in a single test run.

Typically, NIT was conducted using a strain rate of 0.1 /s. The indent depths were usually between 200 ~ 250 nm. All NIT was conducted at room temperature using a Berkovich type indenter. Most of the indents were made using a load-displacement profile that included a 60 second, constant-load hold time. Such loading profiles allow for the creep properties to be assessed. A typical load versus displacement plot of a nanoindentation test is shown in Figure A.1. Analysis of the load versus displacement enables properties such as hardness, elastic modulus, and steady-state creep exponents to be determined. To obtain additional information about deformation and fracture processes associated with indentation, SEM images were taken and characterized for most of the indents made.

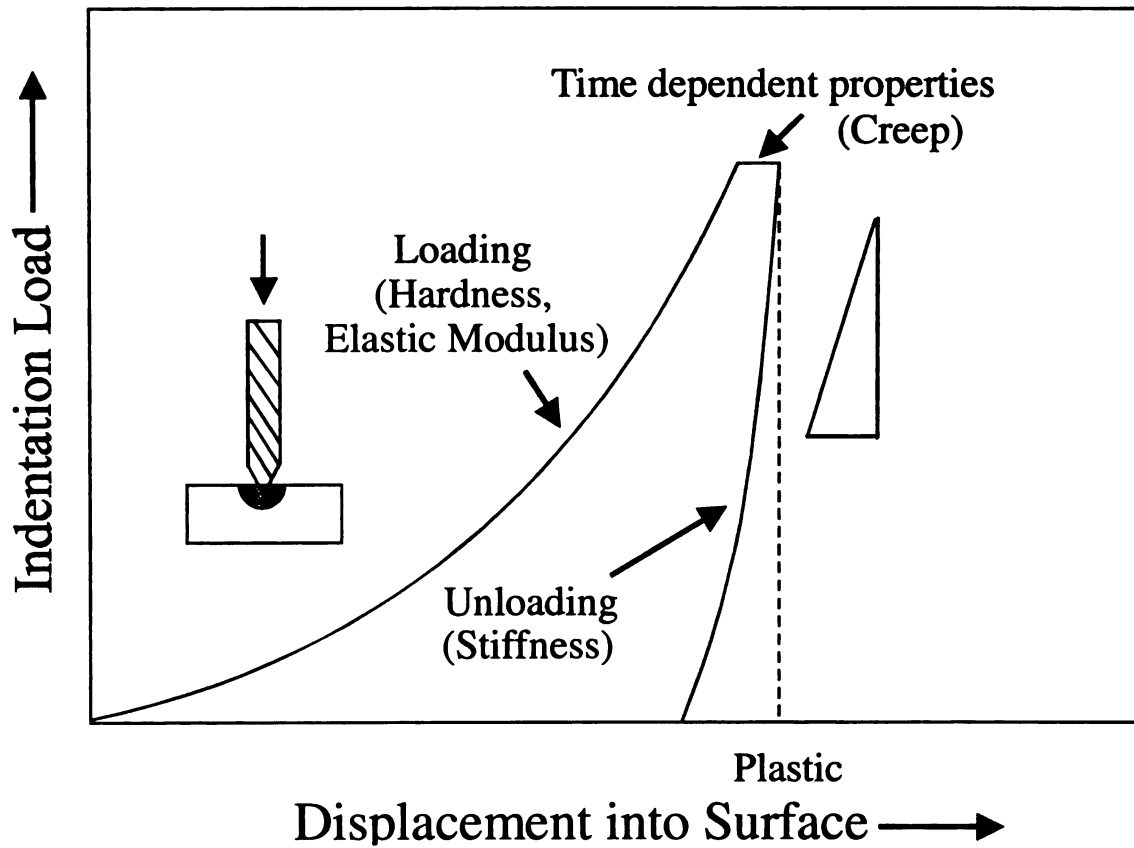


**Figure A.1** A schematic of the indentation load/displacement plot showing loading, hold and unloading segments.

### 3 RESULTS AND DISCUSSION

#### 3.1 Microstructural Characterization of the Solder Joints

The microstructures of as-fabricated and thermomechanically fatigued solder joints are shown in Figures A.2 and A.3, respectively. As-fabricated eutectic Sn-Ag solder joints consisted of the Cu substrate, the  $\text{Cu}_6\text{Sn}_5/\text{Cu}_3\text{Sn}$  interfacial IMC layer, eutectic Sn-Ag phase ( $\text{Ag}_3\text{Sn}$  particle bands), and primary Sn-rich phase. However, the thickness of  $\text{Cu}_3\text{Sn}$  in the IMC layer in the as-fabricated solder joint is minimal. After the TMF cycling, however, significant growth of the interfacial IMC bi-layer of  $\text{Cu}_3\text{Sn}$  and  $\text{Cu}_6\text{Sn}_5$  is evident, and coarsening of the  $\text{Ag}_3\text{Sn}$  particles is readily observed. Coarsening of  $\text{Ag}_3\text{Sn}$  particles at the expense of smaller ones lead to the Sn-rich phase becoming the dominant microstructural feature in the solder joint. The interfacial IMC layer thickness of TMF joints increased by a factor of  $\sim 2.0$  depending on the number of cycles applied. Also, the IMC layer became more uniform in thickness and the surface roughness decreased. Detailed characterization of the interfacial IMC bi-layer formation and the mechanisms for growth can be found elsewhere [81,83,84,90].

Microstructural comparison between as-fabricated and thermomechanically fatigued Sn-4.0Ag-0.5Cu solder joints exhibited similar microstructural features as that for eutectic Sn-Ag solder joints. Again, most prevalent feature is coarsening of the  $\text{Ag}_3\text{Sn}$  phase and thickening of the interfacial IMC layer (Figure A.3 (b)). The IMC layer grew about 2.5 times its initial thickness in this ternary alloy due to TMF cycling.

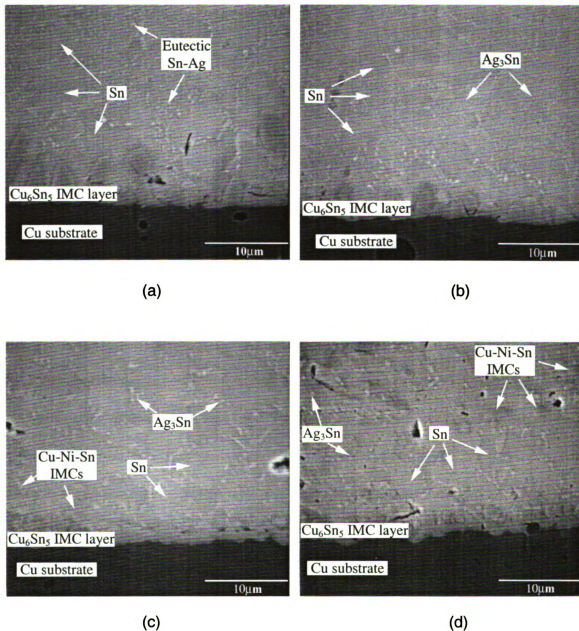


**Figure A.2** Microstructures of the as-fabricated solder joints: (a) Eutectic Sn-3.5Ag, (b) Sn-4.0Ag-0.5Cu, (c) Sn-2.5Ag-0.5Cu-0.5Ni, and (d) Sn-2.0Ag-1.0Cu-1.0Ni.

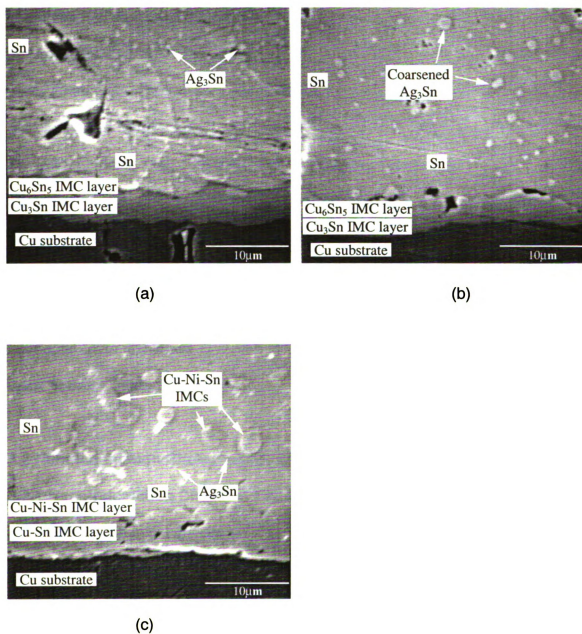


**Figure A.3** Microstructures of the solder joints after 1000 TMF cycles: (a) Eutectic Sn-3.5Ag, (b) Sn-4.0Ag-0.5Cu, and (c) Sn-2.0Ag-1.0Cu-1.0Ni solder joints.

The microstructure of joints made with quaternary alloys exhibited additional constituent phases. Their microstructures consisted of the usual interfacial IMC layer, eutectic  $\text{Ag}_3\text{Sn}$  particles, the Sn-rich phase, and in addition matrix-embedded IMC particles consisting of Cu-Ni-Sn phase. The Cu-Ni-Sn particulates were distributed rather uniformly in the Sn matrix phase. Just as in the binary and ternary alloys, dramatic coarsening of eutectic  $\text{Ag}_3\text{Sn}$  and Cu-Ni-Sn IMC particles was observed as a consequence of TMF cycling, in the quaternary alloys also. The increased thickness of the interfacial IMC layer can be seen in Figure A.3 (c). Solder joints made with the two quaternary alloys showed that the interfacial IMC layer composition contained Cu, Sn, and Ni rather than just Cu and Sn. It is also interesting to note that the Cu-Ni-Sn interfacial layer thickness increased during TMF by ~3 times its as-fabricated value in these quaternary alloys.

## **3.2 Nanoindentation Characterization of the Solder Joints**

### **3.2.1 Nanoindentation Characterization of Micro-Phases**

Micromechanical properties of constituent phases were obtained for all solder materials by mechanically probing the appropriate regions of the solder joints. In general, it is found that the micromechanical properties observed depended strongly on the local microstructure of the indent site.

Table 1 provides the elastic modulus and hardness values according to the indentation site of each constituent phase for as-fabricated and after 1000 TMF cycles in eutectic Sn-Ag solder joints. The hardness values of the IMCs were

**Table A.1** Micromechanical properties of constituent phases in eutectic Sn-3.5Ag solder joints.

	<b>Constituents</b>	<b>Elastic Modulus (GPa)</b>	<b>Hardness (GPa)</b>	<b>Location of the indent</b>
<b>As-fabricated solder joints</b>	Solder matrix	57.2, 50.7, 60.2, 58.3	0.40, 0.59, 0.47, 0.52	Near the interfacial IMC layer
		55.5, 60.2, 51.3	0.51, 0.58, 0.41	Ag <sub>3</sub> Sn Particle bands
	IMC	45.5, 47.0	0.28, 0.29	Tin cell
		68.3, 59.0, 100.3	3.13, 2.44, 5.70	Interfacial IMC layer
		100.9, 83.7	5.06, 5.18	IMC particles
Cu substrate	123.7, 125.6, 126.2	2.67, 2.28, 2.33	Cu substrate	
<b>1000 cycle TMF solder joints</b>	Solder matrix	44.5, 51.7, 56.8, 49.3, 48.5	0.26, 0.32, 0.44, 0.31, 0.31	Tin cell
	IMC	115.1	6.67	Interfacial IMC layer

**Note:** Hardness values of interfacial IMC layer in the as-fabricated condition are not reliable due to the scallop-shape of the thin IMC layer present under such conditions. However, IMC particles were large enough even in the as-fabricated condition to provide reliable hardness values.

significantly higher than those of the solder matrix and the Cu substrate as well. A comparison of the hardness of the interfacial IMC layer of both as-fabricated and thermomechanically fatigued solder joints indicates that their hardness values in as-fabricated joints were somewhat lower (Table A.1). A reason for the observed difference in hardness is due, in part, to the particular location of the indent with respect to the IMC layer thickness and morphology. Since the IMC layer of the as-fabricated joints is narrow and non-uniform in thickness, it is often difficult to position the indent in the center of the IMC layer. Off-center indent locations near IMC/solder interfaces tend to provide lower hardness values, whereas centered indents give higher values. It is also felt that the microstructure and relative volume fractions of  $\text{Cu}_6\text{Sn}_5$  and  $\text{Cu}_3\text{Sn}$  in the IMC layer can affect observed hardness values.  $\text{Cu}_3\text{Sn}$  of the IMC layer tends to be harder than  $\text{Cu}_6\text{Sn}_5$  as reported from earlier nanoindentation studies [114].

For the solder matrix region of as-fabricated eutectic Sn-Ag solder joints, the average hardness values also varied with indenter locations depending on whether the indents were located near the IMC/solder interfacial layer or on a eutectic  $\text{Ag}_3\text{Sn}$  particle band. When indents are located in the latter microstructural regions, higher hardness values were observed as compared to indents located in a pure tin cell. The hardness values are about 0.5 GPa and 0.24 GPa respectively, as depicted in Figure A.4. Typically, the average hardness values of the solder matrix region of thermomechanically fatigued eutectic Sn-Ag solder joints were lower with wider scatter in the data (see Figure A.4). The lower hardness of the solder matrix region of thermomechanically

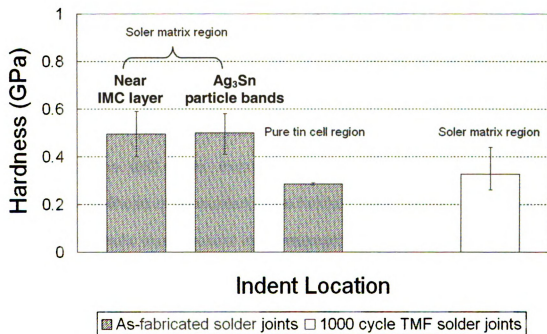


**Figure A.4** Comparison of hardness values of eutectic Sn-Ag solder joints with respect to indenter location in as-fabricated and after 1000 TMF cycle conditions.



fatigued joints is mostly likely due to coarsening of the eutectic  $\text{Ag}_3\text{Sn}$  particles which result in lowering of the strength and hardness of the solder matrix.

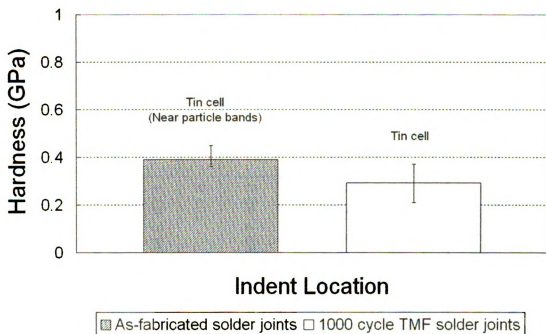
The elastic modulus and hardness values appropriate to the indent location for as-fabricated and 1000-cycle thermomechanically fatigued Sn-4.0Ag-0.5Cu solder joints are listed in Table A.2. This ternary alloy solder joint also exhibited similar trends in hardness values, as did eutectic solder joints. The interfacial IMC layer of the 1000-cycle thermomechanically fatigued solder joints possessed higher hardness values than that present in the as-fabricated solder joints. Thermomechanically fatigued solder joints have a thickly-grown  $\text{Cu}_3\text{Sn}/\text{Cu}_6\text{Sn}_5$  IMC bi-layer. If the IMC layer is fairly thick, indents can easily be positioned in the center of the IMC layer, thus mitigating any lateral constraint issues. However, the likelihood of encountering the harder  $\text{Cu}_3\text{Sn}$  phase is greater in the interface intermetallic layer present in thermomechanically fatigued solder joints. The solder matrix region of the 1000-cycle thermomechanically fatigued solder joints was generally softer as compared to the solder matrix region of as-fabricated solder joints as noted in Figure A.5. Such softening in the solder matrix region is very likely due particle coarsening and other microstructural annealing processes induced by TMF cycling.

Table A.3 shows the elastic modulus and hardness values associated with the location of each indent for as-fabricated and 1000-cycle thermomechanically fatigued quaternary alloy (Sn-2.0Ag-1.0Cu-1.0Ni) solder joints. The solder matrix region of this solder alloy, both in as-fabricated and in TMF conditions exhibit similar hardness values as indicated in Figure A.6. The similarity in the

**Table A.2** Micromechanical properties of constituent phases in Sn-4.0Ag-0.5Cu solder joints.

	Constituents	Elastic Modulus (GPa)	Hardness (GPa)	Location of the indent
<b>As-fabricated solder joints</b>	Solder matrix	48.3, 50.6, 50.0, 42.9, 46.0	0.45, 0.36, 0.44, 0.36, 0.42	Near the Ag <sub>3</sub> Sn particle bands
	IMC	65.0, 50.2	1.38, 0.40	Interfacial IMC layer near the solder matrix
<b>1000 cycle TMF solder joints</b>	Solder matrix	39.0, 40.7, 49.6, 53.6	0.21, 0.28, 0.31, 0.37	Tin cell
	IMC	95.0, 100.2	5.38, 5.57	Interfacial IMC layer

**Note:** Hardness values of interfacial IMC layer in the as-fabricated condition are not reliable due to the scallop-shape of the thin IMC layer present under such conditions.



**Figure A.5** Comparison of hardness values of Sn-4.0Ag-0.5Cu solder joints within solder matrix region in as-fabricated and after 1000 TMF cycle conditions.

**Table A.3** Micromechanical properties of constituent phases in Sn-Ag-1.0Cu-1.0Ni solder joints.

	Constituents	Elastic Modulus (GPa)	Hardness (GPa)	Location of the Indent
<b>As-fabricated solder joints</b>	Solder matrix	57.2, 47.7, 54.3, 56.9, 49.2	0.41, 0.40, 0.32, 0.31, 0.29	Solder matrix
		54.6, 67.1	0.52, 0.49	Near the interfacial IMC layer
	IMC	101.8	4.73	Interfacial IMC layer
		65.0, 59.7, 49.0	1.48, 1.59, 1.06	Interfacial IMC layer near the solder matrix
<b>1000 cycle TMF solder joints</b>	Cu substrate	111.5, 76.2	7.01, 3.71	IMC particles
	Solder matrix	115.2, 125.8	2.02, 2.36	Cu substrate
		60.9, 56.5, 41.8, 52.1, 53.1, 51.3, 56.1	0.40, 0.34, 0.33, 0.32, 0.33, 0.31, 0.35	Solder matrix
	IMC	97.7, 103.9, 113.5, 89.1	5.01, 5.39, 6.50, 4.20	Interfacial IMC layer

**Note:** Hardness values of interfacial IMC layer in the as-fabricated condition are not reliable due to the scallop-shape of the thin IMC layer present under such conditions. However, IMC particles were large enough even in the as-fabricated condition to provide reliable hardness values.

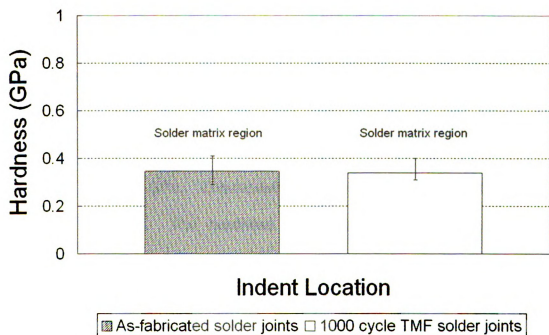


**Figure A.6** Comparison of hardness values of Sn-Ag-1.0Cu-1.0Ni solder joints within solder matrix region in as-fabricated and after 1000 TMF cycle conditions.

solder matrix hardness values under both conditions is reflective of the uniform IMC particles distribution throughout the solder matrix in the quaternary solders.

### **3.2.2 Nanoindentation Characterization on Macro-Phase Regions of Solder Joints**

A composite illustration is shown in Figure A.7 of the overall elastic modulus and hardness data of as-fabricated solder joints made with the various solder alloys. It is evident from the result presented in Figure A.7 the mechanical properties acquired using nanoindentation testing are comparable to those obtained using more conventional static testing methods [115,116]. The average modulus of the Cu substrate is 120 GPa. For the IMC layer moduli range from ~73 to 115 GPa. The moduli of solder regions of the joints are given from 50 to 56 GPa. The hardness of the interfacial IMC layer reveals significantly more scatter, but in general, has a greater hardness compared to the solder matrix and Cu substrate. An additional point to note is that the hardness values observed in the solder matrix of the quaternary (Sn-2.0Ag-1.0Cu-1.0Ni) alloy joints were consistently higher than the hardness values in the solder matrix region of the joints made with other solder alloys. As suggested previously, the higher hardness values are due likely to the increased volume fraction and distribution of Cu-Sn and Cu-Sn-Ni containing intermetallic particles in the matrix of the quaternary alloy solder material.

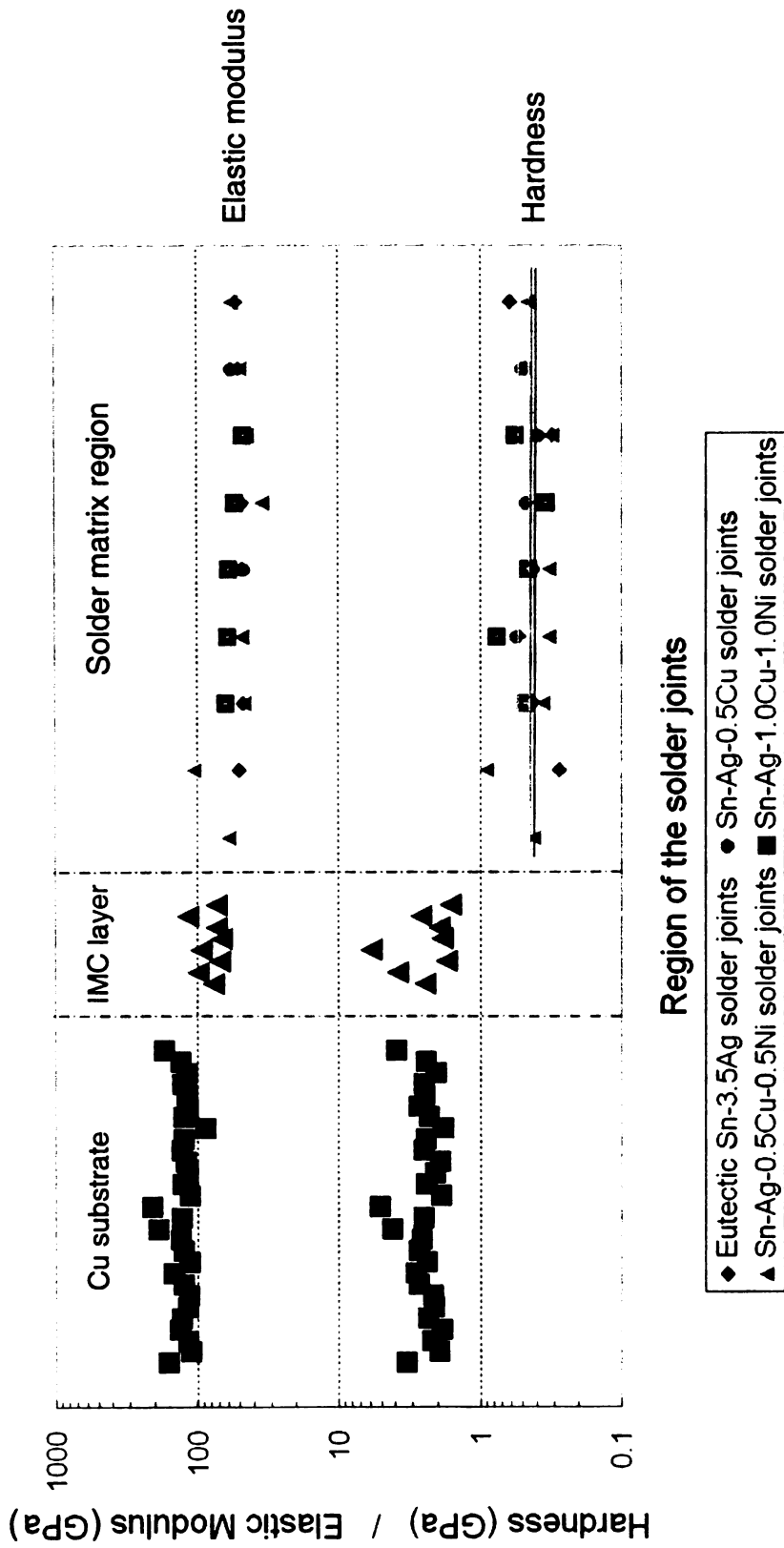


**Figure A.7** The overall comparison of the elastic modulus and hardness values of the Cu substrate, IMC layer and solder matrix region for the four different solder joints in as-fabricated condition.

### **3.2.3 Mechanical Behavior of Thermomechanically fatigued and Thermomechanically fatigued/Crept Solder Joints**

Comparing the properties of as-fabricated solder joints to thermomechanically fatigued, and thermomechanically fatigued and then crept solder joints, a quite noticeable trend can be observed. Figures A.8 (a) and (b) display a change of the hardness and relative yield strength values for 1000-cycle thermomechanically fatigued solder joints compared to as-fabricated solder joints. The hardness and relative yield strength tended to decrease as a result of TMF cycling. Figures A.9 (a) and (b) show the decreasing trend in the hardness and the relative change of yield strength values for 250, 500, 1000-cycles thermomechanically fatigued solder joints that were then crept, as compared to as-fabricated solder joints.

### **3.2.4 Steady-State Power-Law Creep Stress Exponent Using NIT**

Constant-load-hold creep tests were performed using the nanoindenter to obtain steady-state creep stress exponent ( $n$ ) values in various constituent phases of as-fabricated solder joints. Depending on the constituent phase probed by the indenter, ' $n$ ' values ranged from 11 to 38. The stress exponent for steady-state creep of the interfacial IMC layer is considerably greater than that of the solder matrix region, as shown in Figure A.10. As indicated in Figure A.11, the ' $n$ ' values increased for the solder when the indent was located in eutectic  $\text{Ag}_3\text{Sn}$  particle regions in the solder matrix. These findings show that creep behavior and deformation processes are highly variable in different localized microstructural regions of the solder joint. This also suggests that the overall

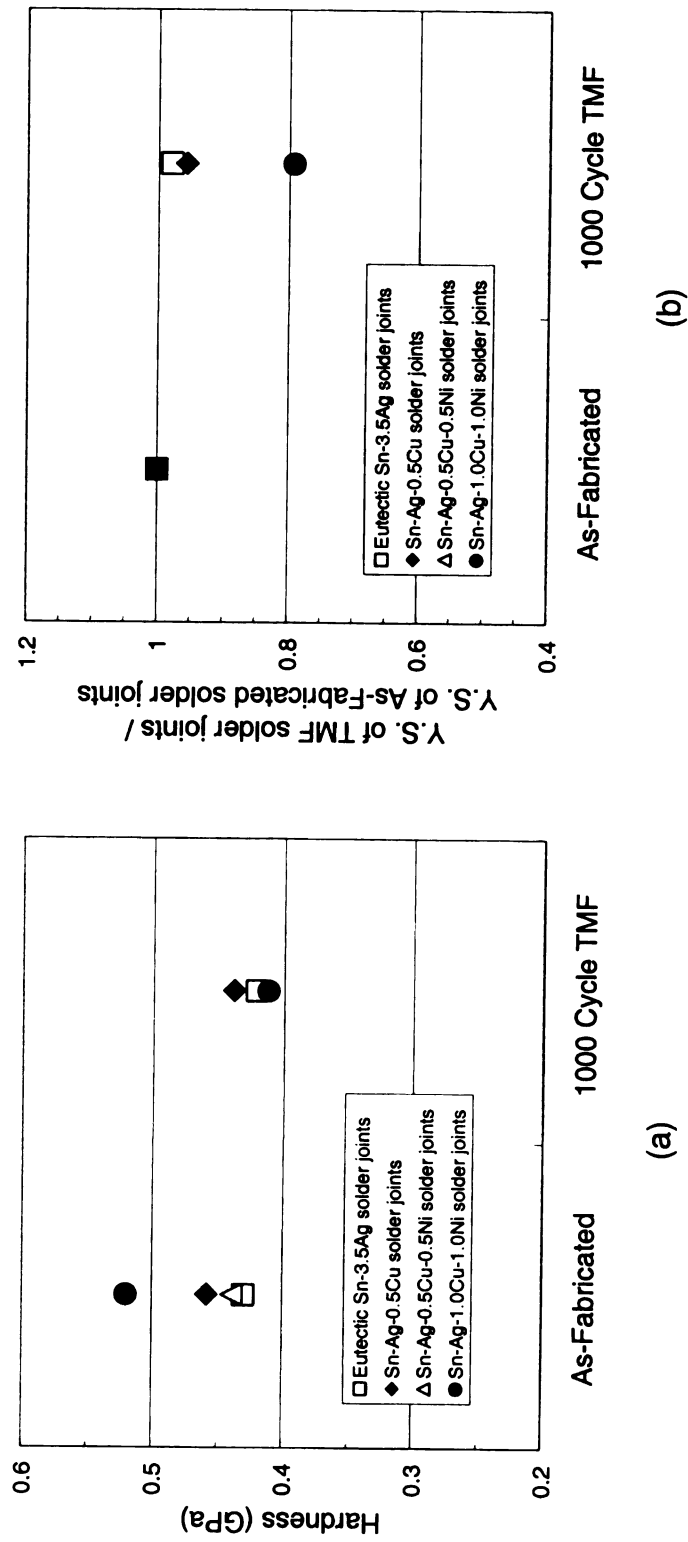


**Figure A.8** The changes in (a) hardness and (b) relative yield strength of solder joints after 1000 TMF cycles.

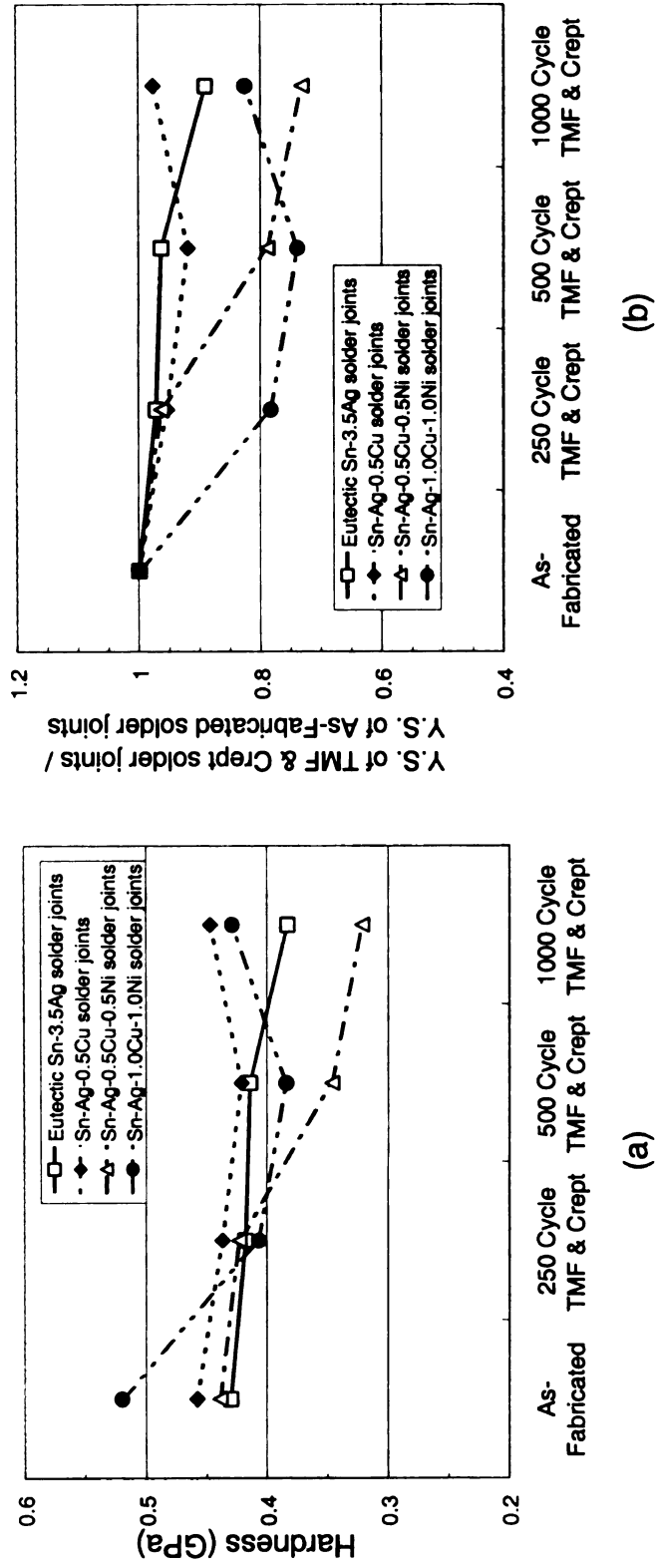


**Figure A.9** The variability of (a) hardness and (b) relative yield strength values for 250, 500, 1000 cycle thermomechanically fatigued and then crept solder joints as compared to as-fabricated solder joints.

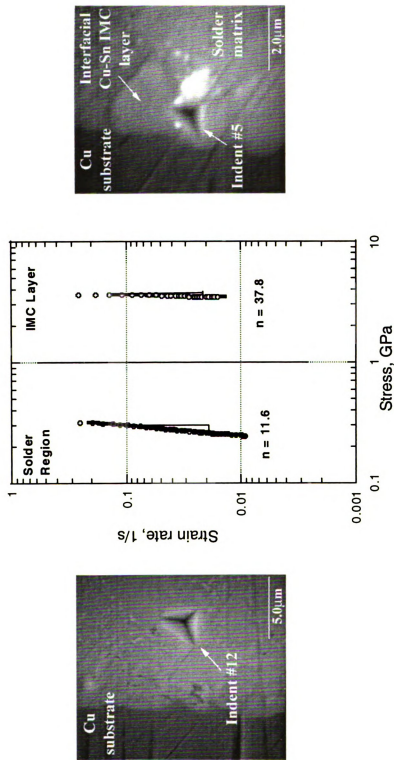


**Figure A.10** The stress exponent for steady-state creep of the solder matrix and the interfacial IMC layer for as-fabricated Sn-4.0Ag-0.5Cu solder joint. The micrographs show the location of the indent in the solder joint.

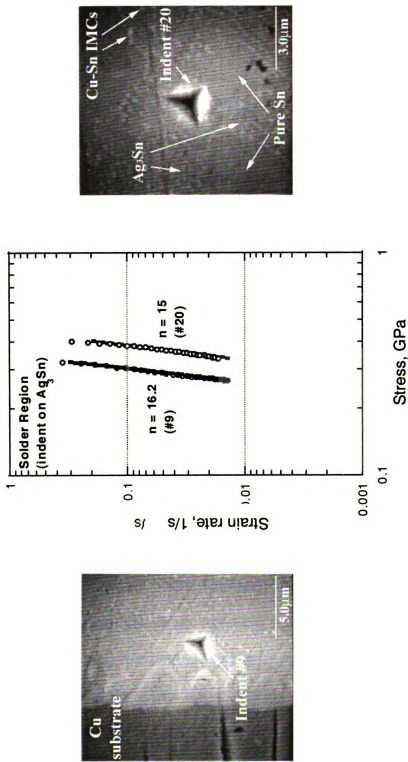


**Figure A.11** The stress exponent for steady-state creep of the indenter lying on the solder matrix region for as-fabricated Sn-4.0Ag-0.5Cu solder joint. The micrographs show the location of the indenter in the solder joint microstructure.

creep rate of the solder joint represents the average sum of creep rates occurring locally throughout the microstructure of the joint.

#### **4 SUMMARY**

Using nanoindentation methods, materials properties were obtained in small-size lead-free solder joints in the as-fabricated condition and joints exposed to thermomechanical cycling and creep conditions. From this investigation, we found that:

Micromechanical properties of the solder joints are specific to the microstructure probed at the indent location. The interfacial IMC layer revealed higher hardness compared to the solder matrix region and the Cu substrate.

The elastic modulus and hardness of the solder matrix were generally similar irrespective of the joint's exposure condition. However, indents located near or directly on the IMC's produced higher property values. Quaternary alloy, Sn-2.0Ag-1.0Cu-1.0Ni, solder joints exhibited the highest hardness values for the solder matrix region among the solder alloys investigated.

The hardness and the yield strength of the solder joints decreased with increasing TMF cycles. The TMF/crept solder joints showed similar strength trends. The power law stress exponent for steady-state creep varied depending on the volume and microstructural feature sampled by the indenter probe in the solder joint material. The IMCs possess the highest stress exponent value among the microconstituents of the solder joints.

## **APPENDIX B**

## **APPENDIX B**

### **EFFECTS OF INTERMETALLIC MORPHOLOGY AT METALLIC PARTICLE/SOLDER INTERFACE ON MECHANICAL PROPERTIES OF Sn-Ag BASED SOLDER JOINTS**

#### **ABSTRACT**

Mechanical incorporation of metallic particles in Sn-Ag based solder resulted in various intermetallic compound (IMC) morphologies around these particles during reflow. Unlike with Ni particle, the IMCs formed around Cu and Ag particles are relatively insensitive to reflow profiles employed. IMC formed around Ni particle ranges from 'sunflower' morphology to 'blocky' morphology with increasing time and temperature above liquidus during the heating part of the reflow profile. Mechanical properties, such as simple shear strength and creep behavior of these composite solders, were affected by the IMC morphologies in the composite solders investigated. Sunflower-shaped IMC formed around Ni particle resulted in higher simple shear strength and better creep properties.

## 1 INTRODUCTION

Among potential candidates to replace lead-bearing solders, Sn-based solders have gained significant attention as a possible substitute due to their comparable performances. Severe operational environments such as automotive under-the-hood applications, and the miniaturization trend in electronic devices, require that solder joints not only be a reliable electrical interconnection but also have structural integrity. Several approaches have been reported to improve Sn-based solder properties such as mechanical strength, creep resistance, thermomechanical fatigue (TMF) resistance, and solder joint reliability, etc. [45,50,73,74,76,83,84,89,91,117] The composite approach is one of the potential methodologies to improve the properties of lead-free solder joints.

The mechanical behavior of composite solder joint depends on reinforcing phases present. Such reinforcements can be introduced by *in-situ* methods or by mechanical means. Compatible IMCs can be produced by converting metallic particles during reflow. Mechanical properties of composite solder joint will also depend on type of IMC and its morphological features.

Studies dealing with formation of IMC around intentionally incorporated Cu, Ag, and Ni particles within the eutectic Sn-Ag matrix have shown that various morphological features can result as a consequence of the reflow condition [118]. For example, the IMCs formed around Ag particles neither change significantly in volume nor change their morphology under different reflow conditions. Copper particles in reinforced composite solders show significant growth of IMC layers

that can completely consume the Cu particles. However, this composite also does not exhibit significant changes in IMC morphology as a consequence of reflow profiles. The IMC formed around Ni particle in Sn-Ag based solder matrix exhibits significantly different morphological features based on reflow profiles and the presence of Cu. Since these features may impact the mechanical behavior of actual solder joints, the current study evaluates the roles of morphological features of the reinforcing phases on the mechanical properties of the Sn-Ag based composite solder joints.

## **2 EXPERIMENTAL PROCEDURES**

### **2.1 Preparation of Composite Solder Joints**

Three different types of composite solder joints based on the eutectic Sn-3.5Ag composition were used in the present study. The composite solder materials were prepared by mechanically mixing (1) ~ 10 $\mu$ m Cu, (2) ~ 1 $\mu$ m Ag, and (3) ~ 5 $\mu$ m Ni particles into eutectic Sn-Ag solder paste for about 20 minutes to promote uniform particle distribution. These composite solder materials contained approximately 20 vol.% reinforcements. The details of the preparation of these composite solders can be found elsewhere [84]. Single-shear lap joints were produced by soldering two dog-bone shaped Cu strips using one of the composite solder pastes. The solder joints were made by placing entire assembly in a fixture, and melting the solder on a pre-heated hot plate until a peak temperature of 280°C was reached. These joints had approximately 1mm  $\times$  1mm joint area and a thickness of about 100 $\mu$ m. Details

of the fabrication of the solder joints are provided in Chapter 3.2.

Solder reflows were carried out with a heating rate of 5°C/sec to reach 280°C and cooling down on an aluminum chill block [118]. Such a reflow profile resulted in sunflower morphology of IMC around Ni particles. Repeating this reflow by four times converted this IMC morphology into a blocky shape.

After making the composite solder joints, both sides of the joint were roughly polished to remove extruded solder from the edges. This was followed by fine polishing of one side of the joint to observe the microstructure prior to and after mechanical testing. The morphology of the IMC phases at particle/solder interface within the solder joint matrix was characterized by using an SEM.

## **2.2 Shear Test**

The shear tests were carried out on a thermomechanical analyzer (RSA-III) made by Rheometric Scientific, Inc. at various simple shear-strain rates of 0.001 /s, 0.01 /s, and 0.1 /s at different testing temperatures (25°C, 85°C, and 150°C). Details regarding the performance and advantages of this apparatus are described in Chapter 3.2.

The simple shear-strain value for each tested solder joint was calculated by dividing actual displacement imposed on the joint by actual joint thickness. This parameter is too large to be termed as 'shear strain', and 'simple shear-strain' would be a more appropriate term [93,97]. Likewise, the term 'simple shear-strain rate' is used instead of the term 'shear strain-rate'. The simple shear-strain rates imposed were obtained by choosing appropriate displacement rates

depending on actual solder joint thickness. The detailed explanation of the nomenclature and calculation for 'simple shear-strain' and 'simple shear-strain rate' is depicted in Chapter 3.2. The actual shear stress values were obtained by dividing the load by the solder joint area after subtracting pore area observed in fracture surfaces. Since the RSA-III used in this study is an extremely soft machine and controls displacement rather than strain, the reported simple shear-strain values are already corrected for the compliance of the machine and the substrates. After obtaining the machine compliance value, actual displacements imposed on the solder joint were obtained by subtracting the deformation of the machine and the copper strips from the imposed displacement.

After the completion of the shear test on a given specimen, deformation structures were observed from the fine-polished side surfaces of the solder joints using SEM.

### **2.3 Creep Test**

Creep testing was carried out on these solder joints, marked with laser pattern or a scratch [80], using dead weight loading on a miniature creep testing frame fixed on an optical microscope. The deformation of the polished side of the solder joint was monitored using a Kodak<sup>®</sup> CCD camera connected to a microscope and a computer. The creep data were obtained by mapping the time-sequence images of the distorted laser-ablation patterns or a scratch mark at set time intervals. Creep tests were conducted at 25°C and 85°C on the solder joints representing homologous temperatures  $T/T_{\text{melt}} (^{\circ}\text{K}) = 0.6$  and 0.72,

respectively. For elevated temperature tests, the solder joint was heated by conduction with a heating pad affixed to the copper strip. The testing temperature was monitored by a thermocouple in close contact with the solder joint. The details of this creep testing process and data process technique is documented in the previously published papers [72,75,80,89].

### **3 RESULTS AND DISCUSSION**

#### **3.1 Microstructures of Composite Solder Joints**

Typical microstructures of as-fabricated Cu, Ag, and Ni composite solder joints based on eutectic Sn-Ag solder are shown in Figure B.1 along with a Ni composite solder joint that had been reflowed four times. The Cu composite solder joint has scallop-shaped IMC layer, whereas Ag composite solder joint has very thin layer of IMC around the metallic particles. The effect of multiple reflow on the growth of IMC formed around Ni particle reinforcements can also be seen. The blocky morphology develops after the fourth reflow (Figure B.1 (d)), whereas the initial morphology of IMC around Ni particle is the sunflower shape (Figure B.1 (c)). The detailed explanation of those features can be found elsewhere [85,118].

#### **3.2 Shear Test**

The shear stress versus simple shear-strain curves for the various composite solder joints tested at a simple shear-strain rate of 0.001 /s at each of the three temperatures are shown in Figure B.2. Shear stress versus simple

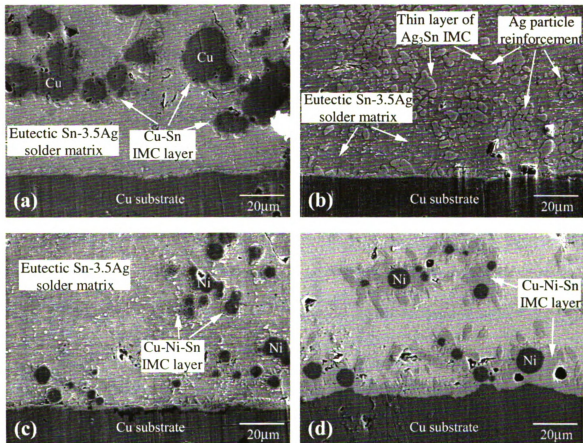


**Figure B.1** Microstructures of composite solder joints based on eutectic Sn-3.5Ag solder: as-fabricated conditions of (a) Cu-composite, (b) Ag-composite, (c) Ni-composite solder joints, and (d) four times reflowed Ni-composite solder joint.

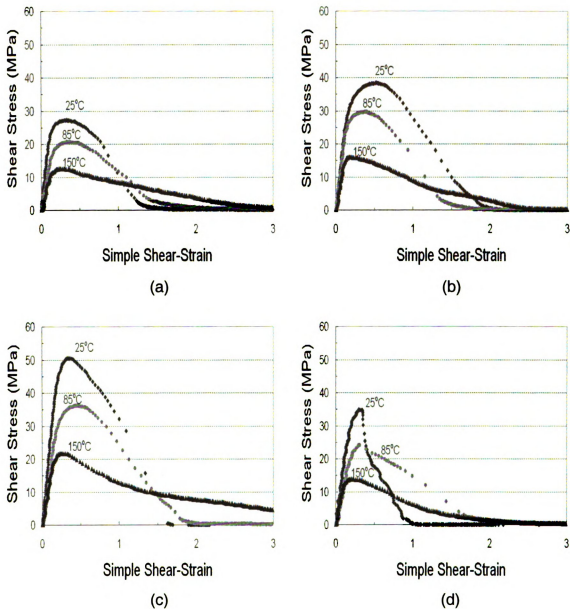


**Figure B.2** Shear stress versus simple shear-strain plots for various composite solder joints at a simple shear-strain rate of 0.001 /s at different testing temperatures: as-fabricated conditions of (a) Cu-composite, (b) Ag-composite, (c) Ni-composite solder joints, and (d) four times reflowed Ni-composite solder joints.

shear-strain curves as a function of simple shear-strain rate at testing temperature of 150°C are depicted in Figure B.3. These figures are typical of those for the various tested conditions of simple shear-strain rates of 0.001 /s, 0.01 /s, and 0.1 /s at different testing temperatures of 25°C, 85°C, and 150°C. The maximum shear stress and the flow stress level of those composite solder joints depend strongly on both testing temperature and simple shear-strain rate. Plots given in Figure B.4 show the maximum shear stress as a function of simple shear-strain rate at different testing temperatures. The maximum shear stress increases significantly with increasing simple shear-strain rate at all testing temperature ranges for all composite solder joints. Also, one can clearly observe that the maximum shear stress is strongly affected by testing temperatures. The maximum shear stress decreases with increasing testing temperature at all simple shear-strain rate levels for all composite solder joints.

Figure B.5 provides an overall comparison of the maximum shear stress of the composite solder joints as a function of temperature at fixed simple shear-strain rate along with that of eutectic Sn-Ag solder joint. One can clearly observe that as-fabricated Ni composite solder joint containing sunflower morphology exhibited the highest maximum shear stress levels for all test conditions followed by Cu composite solder joint containing scallop-shaped IMC layer around Cu reinforcement. Both composite solder joints exhibited better shear strength compared to eutectic Sn-Ag solder joint. However, the Ag composite solder joint, which contains a very thin IMC layer, exhibited the worst shear strength at all the conditions employed. The maximum shear stress level

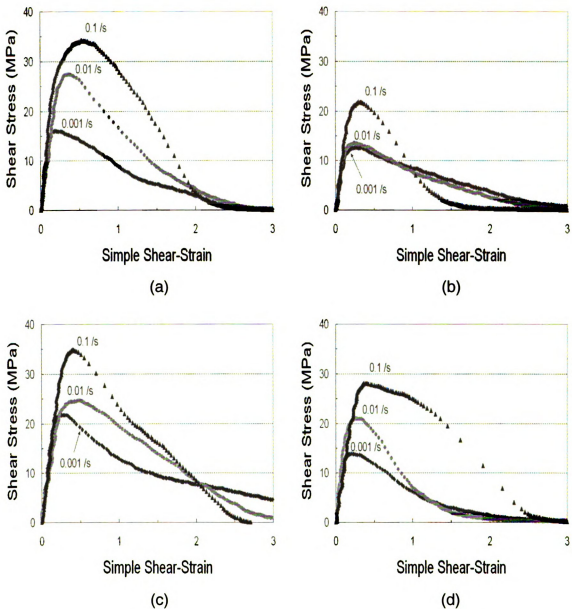
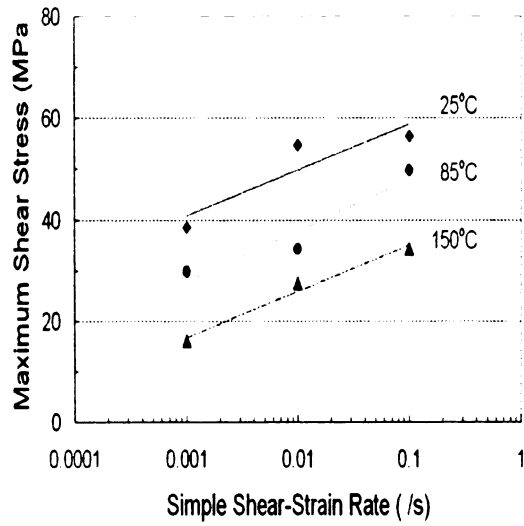
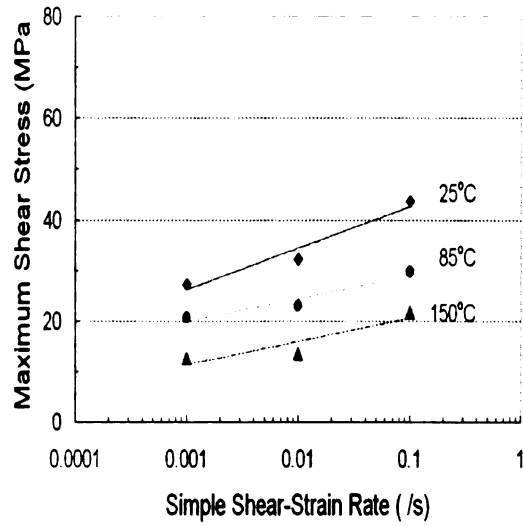


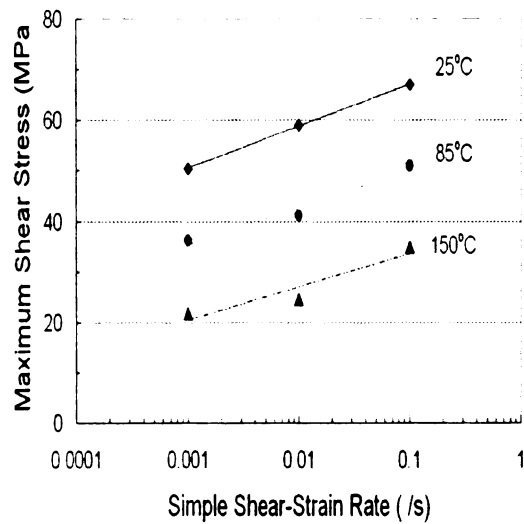
**Figure B.3** Shear stress versus simple shear-strain plots for various composite solder joints at 150°C at different simple shear-strain rates: as-fabricated conditions of (a) Cu-composite, (b) Ag-composite, (c) Ni-composite solder joints, and (d) four times reflowed Ni-composite solder joints.



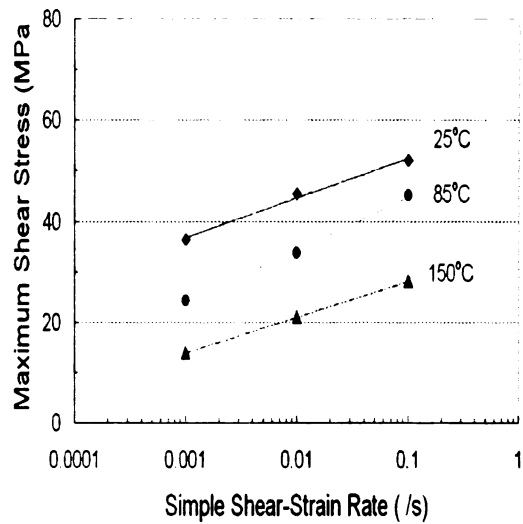
(a)



(b)



(c)



(d)

**Figure B.4** Maximum shear stress as a function of simple shear-strain rate at different temperatures: as-fabricated conditions of (a) Cu-composite, (b) Ag-composite, (c) Ni-composite solder joints, and (d) four times reflowed Ni-composite solder joints.

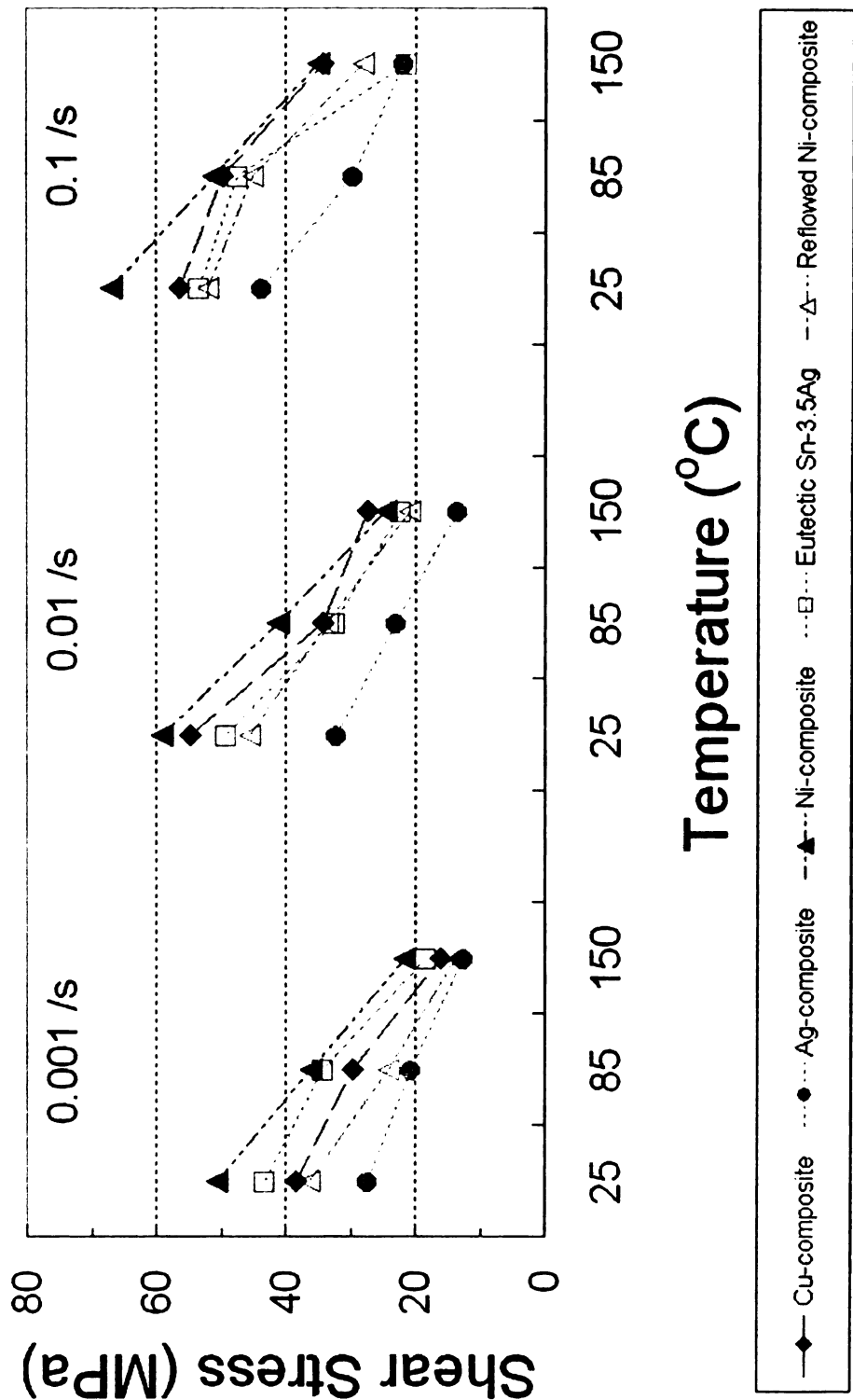


**Figure B.5** Comparison of shear strength of the Cu, Ag, and Ni composite solder joints at various temperatures along with eutectic Sn-Ag solder joint.

of Ag composite solder joint is even lower than that of eutectic Sn-Ag solder joint. The Ni composite solder joint containing blocky IMC morphology that resulted after four reflows exhibited much lower shear strength than that containing sunflower shape IMC.

The microstructures of the solder joint side surfaces after shear testing at a simple shear-strain rate of 0.01 /s at 25°C and 150°C are shown in Figure B.6. The deformation at 25°C is dominated by shear banding mode, whereas that at 150°C it is by a grain boundary deformation. The effect of reinforcing particles and IMC morphology formed around those metallic particles on the deformation features can also be seen. The shear bands do not propagate through the reinforcing particles but flow around these obstacles, suggesting that deformation is retarded by these particles, causing composite solders to have much higher shear strength than the base solder material. However, IMC formed around Ag is very thin so that this effect is not sufficient to retard the propagation of shear deformation. Figure B.7 shows deformation structures of Ni and Ag composite solder joints. These images indicate roles of the IMC around reinforcing particles. This shows that the IMC formed around all reinforcing particles can tortuous and retard the fracture path except those formed around Ag particle.

Figure B.8 is a schematic showing the fracture path in these composite solders. Fracture path in Cu composite solder follows the interface between the  $\text{Cu}_6\text{Sn}_5$  IMC and solder. In Ag composite solder the fracture path not only follows the interface of the thin IMC layer and solder but also cut through the particles. In Ni composite with sunflower IMC morphology, the fracture

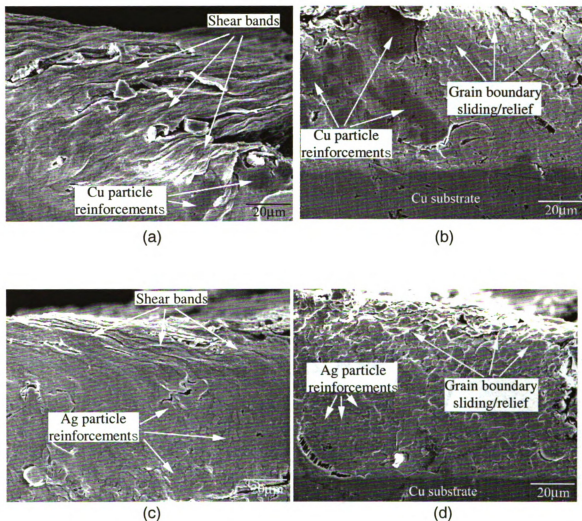
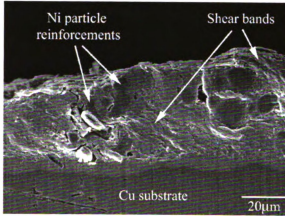
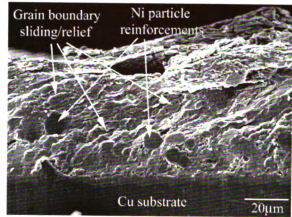


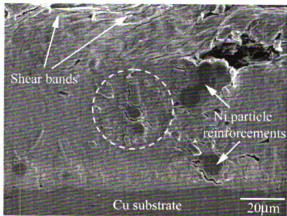
**Figure B.6** Microstructures of the composite solder joint side surfaces after shear test with a simple shear-strain rate of 0.01 /s at various temperatures: (a) Cu composite at 25°C, (b) Cu composite at 150°C, (c) Ag composite at 25°C, (d) Ag composite at 150°C, (e) Ni composite at 25°C, (f) Ni composite at 150°C, (g) four times reflowed Ni composite at 25°C, and (h) four times reflowed Ni composite at 150°C. **(cont'd)**



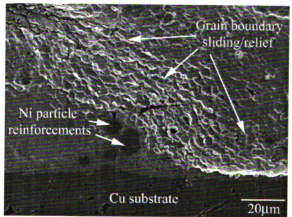
(e)



(f)



(g)



(h)

**Figure B.6 (cont'd)**

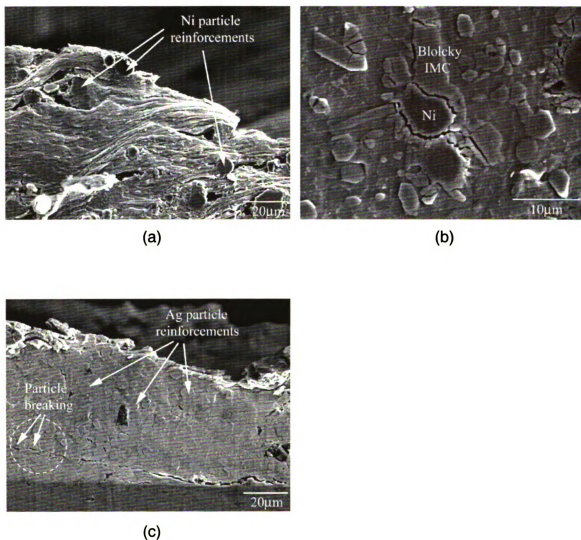


**Figure B.7** Features of the IMCs formed around reinforcing particles within the composite solder joints: (a) Ni composite solder joint with sunflower IMC morphology (specimen deformed to a simple shear-strain rate of 0.1 /s at 85°C), (b) Ni composite solder joint with blocky IMC morphology (enlarged view of Figure B.6 (g); specimen deformed to a simple shear-strain rate of 0.01 /s at 25°C), and (c) Ag composite solder joint (specimen deformed to a simple shear-strain rate of 0.001 /s at 25°C).

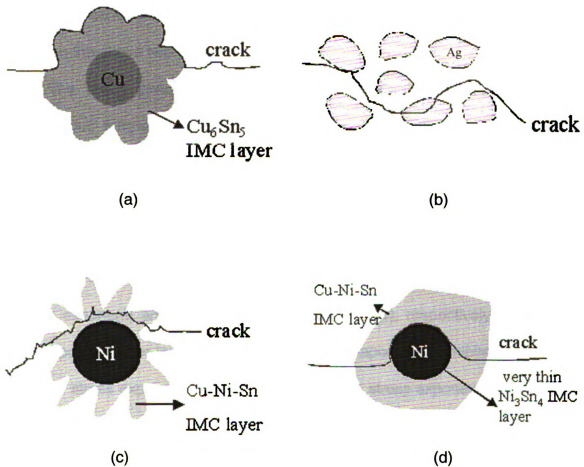


**Figure B. 8** Schematics of fracture paths in various composite solder joints: (a) Cu composite solder, (b) Ag composite solder, (c) Ni composite solder with sunflower IMC morphology, and (d) Ni composite solder with blocky IMC morphology.

encounters a tortuous path. In Ni composite with blocky IMC morphology, the fracture cuts through the Cu-Ni-Sn IMC layer and follows the interface between Ni and IMC. This path will be less torturous compared to the one encountered with sunflower IMC morphology. Scallop-shaped IMC/solder interface in Cu reinforced composite solder provides a situation that will be intermediate between the above two extremes.

The creep parameters can be extracted from the shear tests since homologous temperatures of these composite solder joints are greater than  $0.5T_m$  even at room temperature. The power-law creep equation [98] gives good fits for the simple shear-strain rate versus maximum shear stress relationship from these composite solder joints' shear data at 25°C, 85°C, and 150°C. The creep parameters from the shear tests were depicted in Figures B.9 (stress exponent) and B.10 (creep activation energy), respectively. Again, the Ni composite solder joint containing sunflower-shaped IMC exhibited the highest average stress exponent value of  $\sim 12.9$ , and the stress exponent value at each testing temperature is much higher than that of eutectic Sn-Ag solder joint obtained under similar test conditions [97]. These results are the probable causes of getting higher creep activation energy for Ni composite solder joints as provided in Figure B.10.

### **3.3 Creep Test**

Steady-state creep rates of composite solder joints with Ni composite solder having a blocky IMC morphology were measured under a nominal stress at 17

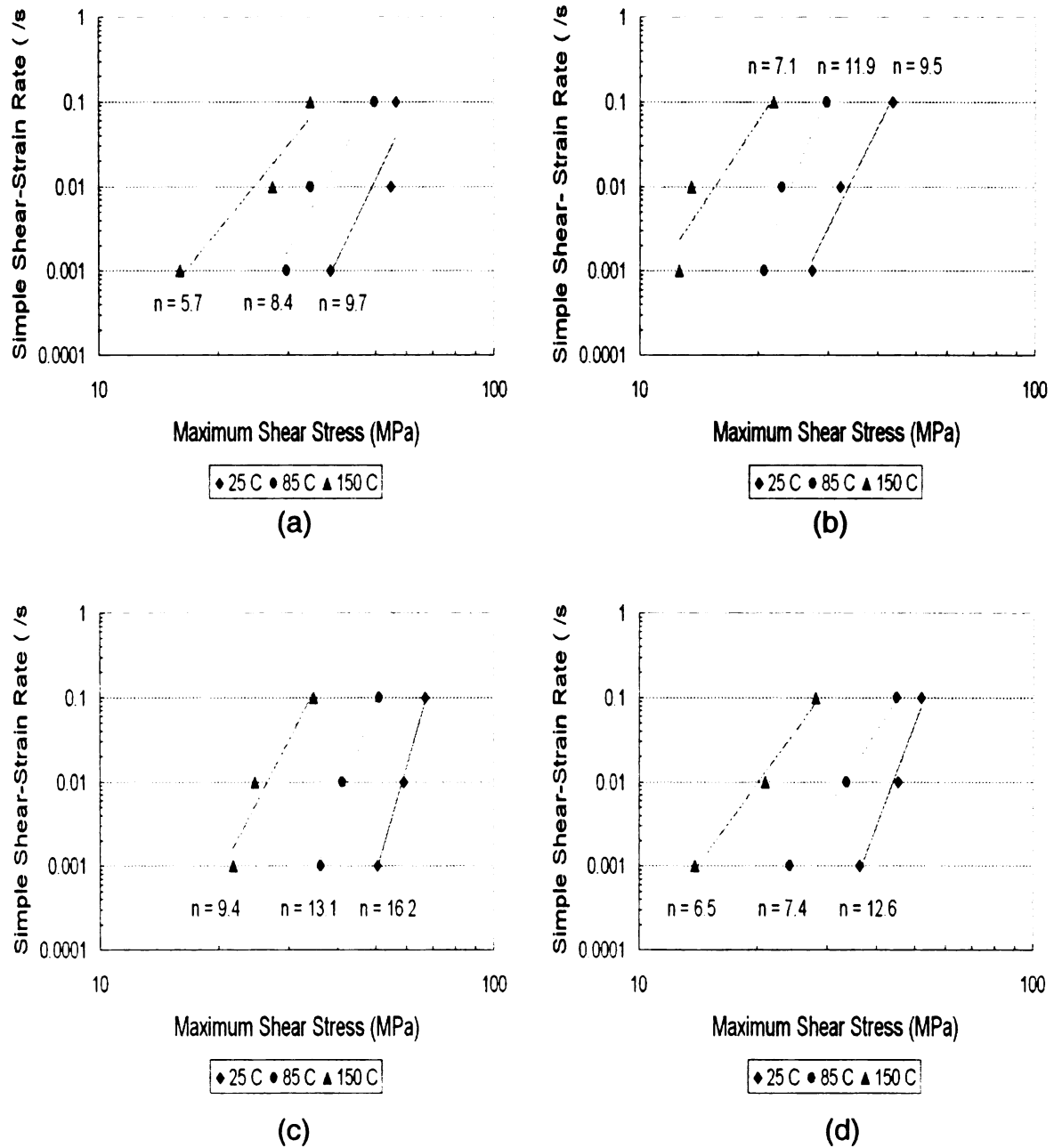
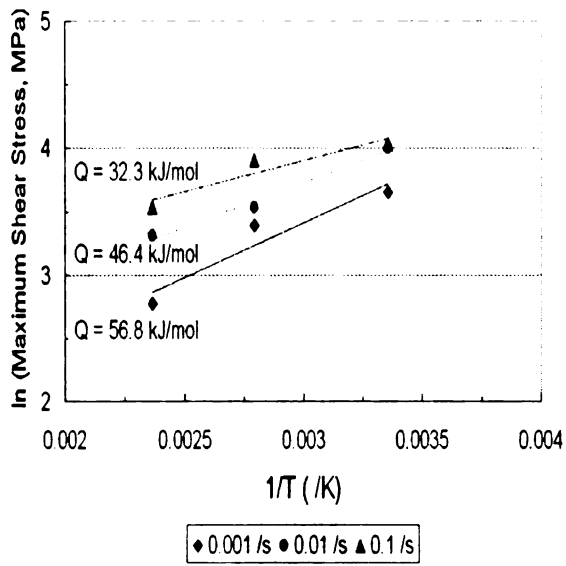
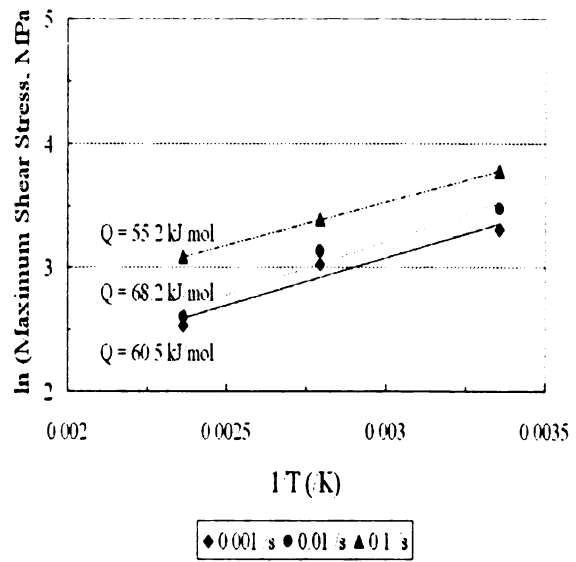


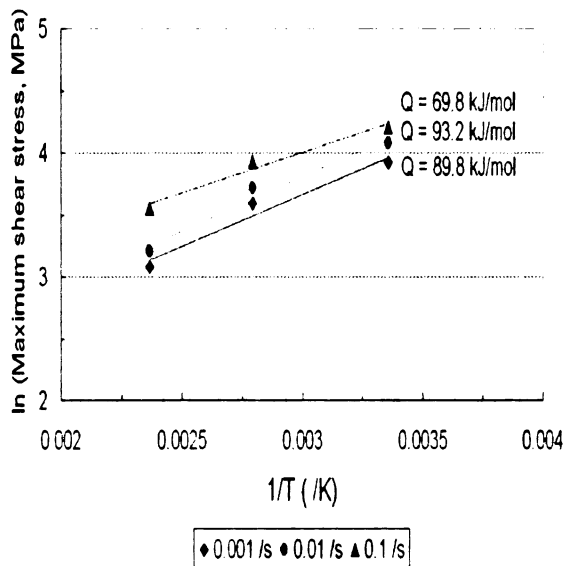
**Figure B.9** Relationship between simple shear-strain rate and maximum shear stress: as-fabricated conditions of (a) Cu-composite, (b) Ag-composite, (c) Ni-composite solder joints, and (d) four times reflowed Ni-composite solder joints.



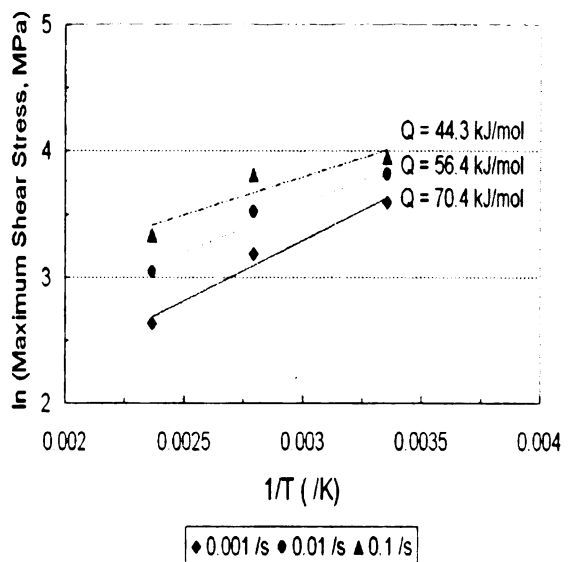
(a)



(b)



(c)



(d)

**Figure B.10** Relationship between shear stress and testing temperature at different simple shear-strain rates: as-fabricated conditions of (a) Cu-composite, (b) Ag-composite, (c) Ni-composite solder joints, and (d) four times reflowed Ni-composite solder joints.

MPa using a miniature creep testing frame. These tests were conducted at 25°C and 85°C on the Ni composite solder joint with blocky-shaped IMC. Those data are plotted as a function of testing temperature in Figure B.11 and compared in the same figure with previously reported steady-state rates for the Ni composite solder joints with sunflower IMC morphology, Cu reinforced composite, Ag reinforced composite, eutectic Sn-Ag, and Sn-4Ag-0.5Cu solder joints tested under similar experimental conditions [72,89]. The previous creep tests have been carried out at 25°C, 65°C, and 105°C. It is clearly shown in this superimposed figure that Ni composite solder joints with sunflower IMC morphology exhibited the lowest steady-state creep rate. At both room temperature and 85°C, the Ni composite solder joints containing blocky reinforcements had a steady-state creep rate higher than the Ni composite solder joint with sunflower IMC morphology as well as the composite solder joints made with Cu reinforcements. However, these composite solder joints showed better creep resistance than Ag composite, eutectic Sn-Ag, and the ternary Sn-4Ag-0.5Cu solder joints. It is reasonable to relate the IMC morphology of the reinforcement particles to the ranking of creep resistance of these composite solder joints. Sunflower-shaped IMC reinforcements improve the creep resistance of the solder joints more than the blocky-shaped IMC reinforcements due to the strengthening effect from their sunflower petals which primarily provide a tortuous path for deformation of the solder joints during creep. The Cu composite solder joints have scallop-shaped IMC morphology with a shape similar to a sunflower with thicker and shorter petals. Therefore, Cu composite

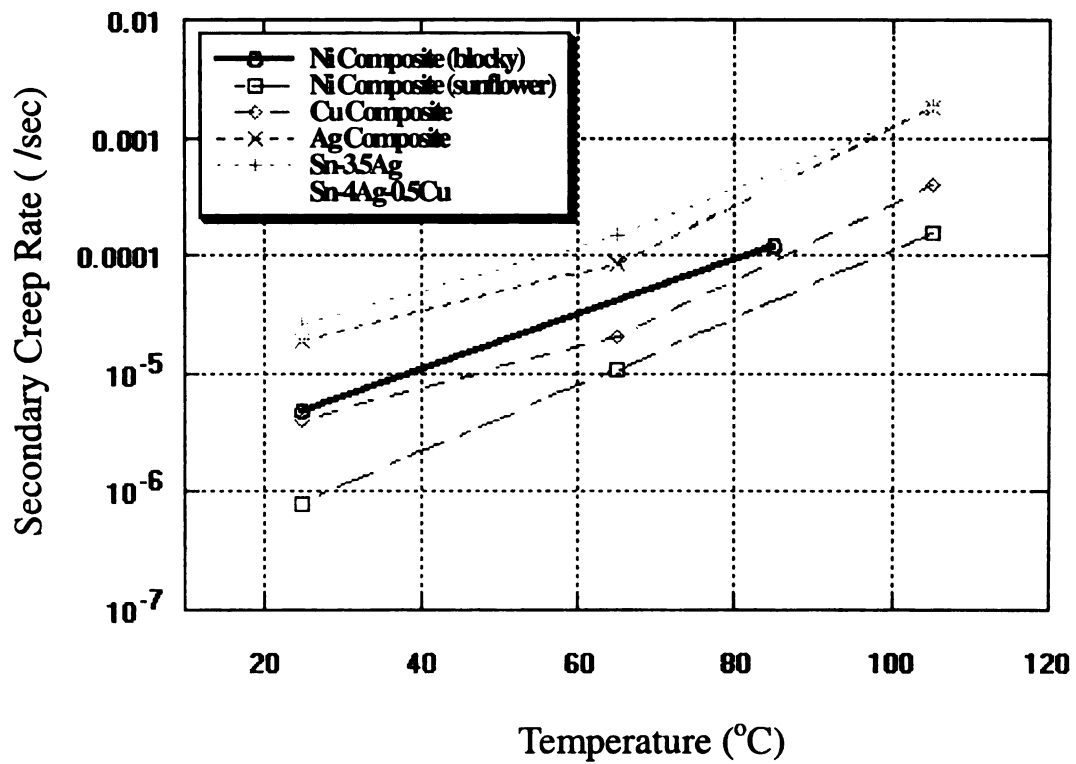


**Figure B.11** Steady-state creep rates of composite solder joints.

**Note:** Data for Ni composite (blocky) obtained in current study.  
Rest from previously published data [89].

solder joints also showed lower steady-state creep rate than the Ni composite solder joints with blocky IMC morphology. Ni composite solder joints with blocky IMC morphology did improve the steady-state creep behavior due to the thick IMC formed compared to Ag composite solder joints in which only a barely-noticeable IMC layer was formed around each Ag particle. In general, to improve the creep resistance of eutectic Sn-Ag solder joint, the formation of a spatially extended IMC is the prerequisite. The morphology of the IMC determines the extent of improvement. The sunflower-shaped IMC morphology tends to render better mechanical properties to the solder joint as compared to the blocky-shaped morphology.

#### **4 SUMMARY AND CONCLUSIONS**

IMCs with different morphologies can be formed around reinforcing phases depending on reinforcing particles and reflow conditions. Since IMC formed around Ni particle is sensitive to reflow profiles, it changes in shape from sunflower to blocky morphology with increasing time and temperature above liquidus.

Maximum shear stress and flow stress level of composite solder joints are strongly affected by testing temperature and simple shear-strain rate. Ni composite solder joint containing sunflower IMC morphology exhibits the highest shear strength among composite solder joints tested. Ni composite solder joint containing blocky IMC morphology exhibits much lower maximum shear stress than Ni composite solder joint containing sunflower IMC morphology at all test

conditions.

Grain boundary deformation can be seen in the specimen deformed at 150°C while deformation at 25°C is dominated by shear bands. Reinforcing phase in composite solder joint may act as an obstacle to retard the propagation of deformation. Ni composite solder joint containing sunflower IMC morphology exhibits the best creep performance just as it behaves in the shear test.

## REFERENCES

## REFERENCES

1. S. Jin, *JOM*, 45 (7), 13 (1993).
2. P.T. Vianco and D.R. Frear, *JOM*, 45 (7), 14 (1993).
3. C. Melton, *JOM*, 45 (7), 33 (1993).
4. M. McCormack and S. Jin, *JOM*, 45 (7), 36 (1993).
5. W.L. Winterbottom, *JOM*, 45 (7), 20 (1993).
6. L.E. Felton, C.H. Raeder, and D.B. Knorr, *JOM*, 45 (7), 28 (1993).
7. J.H. Lau and C. Chang, *1998 IEEE 48th Electronic Components and Technology Conference (ECTC)*, IEEE, Piscataway, NJ, 1339 (1998).
8. F. Hua and J. Glazer, *Design and Reliability of Solders and Solder Interconnections*, TMS, Warrendale, PA, 65 (1997).
9. W.B. Hampshire, *Soldering and Surface Mount Technology*, 14, 49 (1993).
10. J.D. Sigelko and K.N. Subramanian, *Advanced Materials and Processes*, 157 (3), 47 (2000)
11. R.J. McCabe and M.E. Fine, *Scripta Materialia*, 39 (2), 189 (1998).
12. H. Mavoori, J. Chin, S. Vaynman, B. Moran, L. Keer, and M. Fine, *Journal of Electronic Materials*, 26 (7), 783 (1997).
13. J.W. Morris, Jr., *2nd Pacific Rim International Conference on Advanced Materials and Processing*, KIMM, Seoul, 715 (1995).
14. J. Glazer, *Journal of Electronic Materials*, 23 (8), 693 (1994).
15. W. Yang, R.W. Messler, Jr., and L.E. Felton, *Journal of Electronic Materials*, 23 (8), 765 (1994).
16. P.T. Vianco, *Welding, Brazing, and Soldering*, Vol. 6, ASM International, Materials Park, OH, 985 (1993).
17. K.N. Subramanian, T.R. Bieler, and J.P. Lucas, *Journal of Electronic Materials*, 28, 1176 (1999).

18. D.R. Flanders, E.G. Jacobs, and R.F. Pinizzotto, *Journal of Electronic Materials*, 26, 883 (1997).
19. R. Darveaux, K.L. Murty, and I. Turlik, *JOM*, 44, 36 (1992).
20. K.L. Murty and I. Turlik, *Advanced Electronic Packaging*, Vol. 1, ASME, New York, NY, 309 (1992).
21. J.P. Lucas, A.W. Gibson, K.N. Subramanian, and T.R. Bieler, *Fundamentals of Nanoindentation and Nanotribology*, Proceedings of MRS Conference, Vol. 522, MRS, Pittsburgh, PA, 339 (1998).
22. H. Yang, P. Deane, P. Magill, and K.L. Murty, *1996 46th Electronic Components and Technology Conference (ECTC)*, IEEE, Piscataway, NJ, 1136 (1996).
23. S. Choi, K.N. Subramanian, J.P. Lucas, and T.R. Bieler, *Journal of Electronic Materials*, 29 (10), 1249 (2000).
24. E.W. Hare and R.G. Stang, *Journal of Electronic Materials*, 24, 1473 (1995).
25. C.M. Miller, I.E. Anderson, and J.F. Smith, *Journal of Electronic Materials*, 23 (7), 595 (1994).
26. M. McCormack and S. Jin, *Journal of Electronic Materials*, 23 (8), 715 (1994).
27. M. McCormack, H.S. Chen, G.W. Kammlott, and S. Jin, *Journal of Electronic Materials*, 26 (8), 954 (1997).
28. D.M. Jacobson and G. Humpston, *GEC Journal of Research*, 12 (2), 112 (1995).
29. M. McCormack and S. Jin, *Proceedings of the 16th IEEE/CPMT International Electronics Manufacturing Symposium*, IEEE, Piscataway, NJ, 7 (1994).
30. Y. Kariya and M. Otsuka, *Journal of Electronic Materials*, 27 (7), 866 (1998).
31. W.J. Tomlinson and N.J. Bryan, *Journal of Materials Science*, 21, 103 (1986).
32. M. McCormack, S. Jin, and G.W. Kammlott, *IEEE Transactions on Components, Packaging, and Manufacturing Technology — Part A*, 17 (3), 452 (1994).

33. H.S. Betrabet, S.M. McGee, and J.K. McKinlay, *Scripta Metallurgica et Materialia*, 25, 2323 (1991).
34. H.S. Betrabet and S. McGee, *Proceedings of Technical Program — Nepcon West Conference*, Cahners Exhibition Group, Des Plains, IL, Vol. 3, 1276 (1992).
35. S.M.L. Sastry, T.C. Peng, R.J. Lederich, K.L. Jerina, and C.G. Kuo, *Proceedings of Technical Program — Nepcon West Conference*, Cahners Exhibition Group, Des Plains, IL, Vol. 3, 1266 (1992).
36. R.B. Clough, R. Petel, J.S. Hwang, and G. Lucey, *Proceedings of Technical Program — Nepcon West Conference*, Cahners Exhibition Group, Des Plains, IL, Vol. 3, 1256 (1992).
37. H. Mavoori and S. Jin, *Journal of Electronic Materials*, 27 (11), 1216 (1998).
38. J.L. Marshall and J. Calderon, *Soldering and Surface Mount Technology*, 9 (2), 22 (1997).
39. J.L. Marshall, J. Sees, and J. Calderon, *Proceedings of Technical Program — Nepcon West Conference*, Cahners Exhibition Group, Des Plains, IL, Vol. 3, 1278 (1992).
40. J.L. Marshall, J. Calderon, J. Sees, G. Lucey, and J.S. Hwang, *IEEE Transactions on Components, Hybrids, and Manufacturing Technology*, 14 (4), 698 (1991).
41. J.L. Marshall and J. Calderon, *Soldering and Surface Mount Technology*, 9 (3), 6 (1997).
42. J.L. Marshall and J. Calderon, *Soldering and Surface Mount Technology*, 9 (3), 11 (1997).
43. *Metals Handbook 9th ed.*, ASM, Metals Park, OH, 9. 455 (1985).
44. S. Chada, A. Herrmann, W. Laub, R. Fournelle, D. Shangguan, and A. Achari, *Soldering and Surface Mount Technology*, 9 (2), 9 (1997).
45. A.W. Gibson, S.L. Choi, K.N. Subramanian, and T.R. Bieler, *Design and Reliability of Solders and Solder Interconnections*, TMS, Warrendale, PA, 97 (1997).
46. A.D. Roming, Y.A. Chang, J.J. Stephens, D.R. Frear, V. Marcotte, and C. Lea, *The Solder Mechanics: A State of the Art Assessment*, TMS,

- Warrendale, PA, 29 (1991).
47. J.L. Marshall, L.A. Foster, and J.A. Sees, *The Mechanics of Solder Alloy Interconnects*, Van Nostrand Reinhold, New York, NY, 42 (1994).
  48. W. Yang, L.E. Felton, and R.W. Messler, Jr., *Journal of Electronic Materials*, 24 (10) 1465 (1995).
  49. H.D. Solomon, *Journal of Electronic Packaging*, 113, 102 (1991).
  50. A.W. Gibson, S. Choi, T.R. Bieler, and K.N. Subramanian, *IEEE 5th International Symposium on Electronics and the Environment*, IEEE, Piscataway, NJ, 246 (1997).
  51. R.N. Wild, *Welding Research Supplement*, Nov., 521 (1972).
  52. Z. Guo, A.F. Sprecher, Jr., H. Conrad, and M. Kim, *Materials Developments in Microelectronic Packaging Conference Proceedings*, Montreal, Quebec, Canada, 155 (1991).
  53. H. Mavoori, S. Vaynman, J. Chin, B. Moran, L.M. Keer, and M.E. Fine, *Proceedings of Materials Research Society*, 390, 161 (1995).
  54. H. Mavoori, S. Vaynman, J. Chin, B. Moran, L.M. Keer, and M.E. Fine, *Mechanics and Materials for Electronic Packaging: vol. 1 – Design and Process Issues in Electronic Packaging*, Proceedings of 1994 International Mechanical Engineering Congress and Exposition, 165 (1994).
  55. H. Mavoori and J. Chin, *1992 45th Electronic Components and Technology Conference*, IEEE, Piscataway, NJ, 990 (1992).
  56. D.R. Frear, *IEEE Transactions on Components, Hybrids, and Manufacturing Technology*, 12 (4), 492 (1989).
  57. E.C. Kubik and T.P.L. Li, *Martin Marietta Aerospace Internal Report*, Microelectronics Center, Orlando, FL32855.
  58. W. Englemaier, *Circuit World*, 11, 61 (1985).
  59. W.J. Plumbridge, *Journal of Materials Science*, 31, 2501 (1996).
  60. R. Berriche, S. Vaynman, M.E. Fine, D.A. Jeannotte, and M.E. Nicholson, *ASM Third Conference of Electronic Packaging: Materials and Processes and Corrosion in Microelectronics*, Metals Park, OH, 169 (1987).

61. P.J. Greenwood, T.C. Reiley, V. Raman, and J.K. Tien, *Scripta Metallurgica*, 22, 117 (1988).
62. J.G. Lee, F. Guo, S. Choi, K.N. Subramanian, T.R. Bieler, and J.P. Lucas, *Journal of Electronic Materials*, 31, 946 (2002).
63. S. Choi, J.G. Lee, K.N. Subramanian, J.P. Lucas, and T.R. Bieler, *Journal of Electronic Materials*, 31, 292 (2002).
64. E. Baker, *Materials Science and Engineering*, 38, 241 (1979).
65. R. Arrowood and A.K. Mukherjee, *Materials Science and Engineering*, 92, 33 (1987).
66. S.G. Jadhav, T.R. Bieler, K.N. Subramanian, and J.P. Lucas, *Journal of Electronic Materials*, 30 (9), 1197 (2001).
67. M.W. Woodmansee and R.W. Neu, *Materials Science and Engineering A* 322, 79 (2002).
68. K.C. Chen, A. Telang, J.G. Lee, and K.N. Subramanian, *Journal of Electronic Materials*, 31 (11), 1181 (2002).
69. K.J. Ferguson, A. Telang, J.G. Lee, and K.N. Subramanian, *Journal of Materials Science: Materials in Electronics*, 14, 157 (2003).
70. W.D. Nix, *Metallurgical Transactions 20A*, 2217 (1989).
71. W.C. Oliver and G.M. Pharr, *Journal of Materials Research*, 7 (6), 1564 (1992).
72. F. Guo, J.P. Lucas, and K.N. Subramanian, *Journal of Materials Science: Materials in Electronics*, 12, 27 (2001).
73. F. Guo, J. Lee, S. Choi, J.P. Lucas, T.R. Bieler, and K.N. Subramanian, *Journal of Electronic Materials*, 30 (9), 1073 (2001).
74. S. Choi, J.G. Lee, F. Guo, T.R. Bieler, K.N. Subramanian, and J.P. Lucas, *JOM*, 53 (6), 22 (2001).
75. J. McDougall, S. Choi, T.R. Bieler, K.N. Subramanian, and J.P. Lucas, *Materials Science and Engineering A*, 285, 25 (2000).
76. J.W. Morris, Jr., J.L.F. Goldstein, and Z. Mei, *JOM*, 45 (7), 25 (1993).

77. K.I. Chen and K.L. Lin, *Journal of Electronic Materials*, 31 (8), 861 (2002).
78. M.S. Yeh, *Journal of Electronic Materials*, 31 (9), 953 (2002).
79. S.L. Choi, A.W. Gibson, J.L. McDougall, T.R. Bieler, and K.N. Subramanian, *Design and Reliability of Solders and Solder Interconnections*, TMS, Warrendale, PA, 241 (1997).
80. J.P. Lucas, F. Guo, J. McDougall, T.R. Bieler, K.N. Subramanian, and J.K. Park, *Journal of Electronic Materials*, 28 (11), 1270 (1999).
81. S. Choi, T.R. Bieler, J.P. Lucas, and K.N. Subramanian, *Journal of Electronic Materials*, 28 (11), 1208 (1999).
82. J. Sigelko, S. Choi, K.N. Subramanian, J.P. Lucas, and T.R. Bieler, *Journal of Electronic Materials*, 28 (11), 1184 (1999).
83. F. Guo, S. Choi, J.P. Lucas, and K.N. Subramanian, *Journal of Electronic Materials*, 29 (10), 1241 (2000).
84. F. Guo, S. Choi, J.P. Lucas, and K.N. Subramanian, *Soldering and Surface Mount Technology*, 13 (1), 7 (2001).
85. J.G. Lee, F. Guo, K.N. Subramanian, and J.P. Lucas, *Soldering and Surface Mount Technology*, 14 (2), 11 (2002).
86. F. Guo and K.N. Subramanian, *Advanced Materials and Processes*, 160 (12), 41 (2002).
87. F. Guo, S. Choi, K.N. Subramanian, T.R. Bieler, J.P. Lucas, A. Achari, and M. Paruchuri, *Materials Science and Engineering A*, 351, 190 (2003).
88. J.G. Lee and K.N. Subramanian, *Journal of Electronic Materials*, 32 (6), 523 (2003).
89. F. Guo, J. Lee, J.P. Lucas, K.N. Subramanian, and T.R. Bieler, *Journal of Electronic Materials*, 30 (9), 1222 (2001).
90. S. Choi, J.P. Lucas, K.N. Subramanian, and T.R. Bieler, *Journal of Materials Science: Materials in Electronics*, 11, 497 (2000).
91. J.D. Sigelko, S. Choi, K.N. Subramanian, and J.P. Lucas, *Journal of Electronic Materials*, 29 (11), 1307 (2000).
92. A.U. Telang, *MS thesis*, Michigan State University (2002).

93. P. Guerrazzi, *BS thesis*, Michigan State University (1997).
94. S. Choi, *PhD thesis*, Michigan State University (2001).
95. D. Tribula, D. Grivas, and J.W. Morris, *Journal of Electronic Materials*, 17 (5), 387 (1988).
96. R.W. Rohde and J.C. Swearingen, *Journal of Engineering Materials and Technology*, 102 (2), 207 (1980).
97. H. Rhee, K.N. Subramanian, A. Lee, and J.G. Lee, *Soldering and Surface Mount Technology*, 15 (3), 21 (2003).
98. J.H. Lau, *Thermal Stress and Strain in Microelectronics Packaging*, Van Nostrand Reinhold, New York, NY, 472 (1993).
99. H. Rhee and K.N. Subramanian, *Journal of Electronic Materials*, 32 (11), 1310 (2003).
100. Y.H. Pao, S. Badgley, E. Jih, R. govila, and J. Browning, *Journal of Electronic Packaging*, 115 (2), 147 (1993).
101. H.J. Frost and R.T. Howard, *IEEE Transactions on Components, Hybrids, and Manufacturing Technology*, 13 (4), 727 (1990).
102. J. Howell, A. Telang, J.G. Lee, S. Choi, and K.N. Subramanian, *Journal of Materials Science: Materials in Electronics*, 13 (6), 335 (2002).
103. K.N. Subramanian, *Journal of Electronic Materials* (2004) (*in print*).
104. M. Abtey and G. Selvaduray, *Materials Science and Engineering*, 27, 95 (2000).
105. M. Gunawan, E.H. Wong, S.G. Mhaisalkar, L.T. Davila, Y. Hong, J.F.J.M. Caers, and T.K. Tsai, *Journal of Electronic Materials*, 33 (9), 1041 (2004).
106. C. Kanchanomai and Y. Mutoh, *Journal of Electronic Materials*, 33 (4), 329 (2004).
107. H. Rhee, K.N. Subramanian, and A. Lee, *Journal of Materials Science: Materials in Electronics* (2004) (*in review*).
108. T.H. Courtney, *Mechanical Behavior of Materials*, McGraw-Hill, Inc., 263 (1990).
109. G.E. Dieter, *Mechanical Metallurgy 3rd ed.*, McGraw-Hill, Inc., 432 (1986).

110. M.A. Meyers and K.K. Chawla, *Mechanical Metallurgy Principles and Applications*, Prentice-Hall, Inc., 659 (1984).
111. *Smithell's Metals Reference Book 7th ed.*, Butterworth-Heinemann, Ltd., Ch. 13 (1992).
112. D. Shangguan and A. Achari, *1994 IEEE/CPMT International Electronics and Manufacturing Technology Symposium*, IEEE, Piscataway, NJ, 25 (1994).
113. J. Glazer, *International Materials Reviews*, 40 (2), 65 (1995).
114. J.P. Lucas and F. Guo, *Unpublished Research*, Solder Research Group, Michigan State University (1999).
115. R.J. Field, S.R. Row, and G.K. Lucey, Jr., *The Metal Science of Joining*, TMS, Warrendale, PA, 165 (1991).
116. H.P.R. Frederikse, R.J. Field, and A. Feldman, *Journal of Applied Physic*, 72 (7), 2879 (1992).
117. C.G. Kuo, S.M.L. Sastry, and K.L. Jerina, *Microstructures and Mechanical Properties of Aging Materials*, TMS, Warrendale, PA, 409 (1993).
118. J.G. Lee, K.C. Chen, and K.N. Subramanian, *Journal of Electronic Materials*, 32 (11), 1240 (2003).

MICHIGAN STATE UNIVERSITY LIBRARIES



3 1293 02736 1181